COMPLIANT CONTROL OF A TELEOPERATED ENDOSCOPE ROBOT

A Thesis Submitted to
the Graduate School of Engineering and Sciences of
İzmir Institute of Technology
in Partial Fulfillment of the Requirements for the Degree of

MASTER OF SCIENCE

in Mechanical Engineering

by
Oğulcan IŞITMAN

July 2018
İZMİR

We approve the thesis of **Oğulcan IŞITMAN**

Examining Committee Members:

Prof. Dr. Enver TATLICIOĞLU
Department of Electrical & Electronics Engineering
İzmir Institute of Technology

Assoc. Prof. Dr. Mehmet İsmet Can DEDE
Department of Mechanical Engineering
İzmir Institute of Technology

Assoc. Prof. Dr. Levent ÇETİN
Department of Mechatronics Engineering
İzmir Katip Çelebi University

10 July 2018

Assoc. Prof. Dr. Mehmet İsmet Can DEDE
Supervisor
Department of Mechanical Engineering
İzmir Institute of Technology

Prof. Dr. Metin TANOĞLU
Head of the Department of
Mechanical Engineering

Prof. Dr. Aysun SOFUOĞLU
Dean of the Graduate School of
Engineering and Sciences

ACKNOWLEDGMENTS

I am very grateful for the encouragement, support and good wishes of my parents who always support and help me throughout my lifetime.

I am sincerely grateful to my supervisor Assoc. Prof. Dr. Mehmet İsmet Can Dede for his most valuable efforts in guiding, teaching, understanding and throughout the study. I would like to thank all the members of IRL & RAML for their friendship and support. I would like to extend special thanks to my dear friends who always being understanding and always being ready for help, Gizem Ersavaş, Faruk Tuna, Vedat Şenol, Oğuz Gürses, Mert Şener and Orhan Ayit.

This work is supported by The Scientific and Technological Research Council of Turkey via grant number 115E726.

ABSTRACT

COMPLIANT CONTROL OF A TELEOPERATED ENDOSCOPE ROBOT

With the development of the technology, robots are started to be used in many medical application including minimally invasive surgery to overcome disadvantages of conventional open surgery procedures. This thesis is a part of the research project called "Robot-assisted endoscope control that can be controlled by the surgical tools (NeuRoboScope)" for the minimally invasive endoscopic pituitary gland tumor surgery side. During the procedure, endoscope is handled by a robot which moves the endoscope in the human nasal cavity and the movement of the endoscope is constrained by soft tissues. Another operation scenario is the positioning of the endoscope by the surgeon backdriving the endoscope holder robot.

In the scope of this thesis, two research problems are addressed which are controlling the interaction between (1) surgeon - robot and (2) robot - soft tissue. First, the interaction of the surgeon and the robot is studied. Effects of the compliant controller parameters are experimentally tested by using a single degree of freedom non-backdrivable experimental set-up. A task is defined to quantitatively compare the effect of the controller parameters on the performance in terms of the energy efficiency and the accuracy.

The second research problem involves human nasal tissue modeling in order to design an accurate controller. To acquire data from the human cadaver, a new hand-held measurement device is designed. The external forces and moments and the soft tissue models are obtained in an ex-vivo experiment. After the soft tissue models are identified, a modified interaction control is proposed for the teleoperated endoscope holder robot. The defined surgery procedure is tested with the proposed interaction controller via single degree-of-freedom experimental set-up. Experiments of the proposed controllers were successful for the defined operation scenario and the results show that it is possible to realize the motion control of the surgical robots in a constrained environment.

ÖZET

UZAKTAN YÖNLENDİRİLEN BİR ENDOSKOP ROBOTUNUN UYUMLU DENETİMİ

Teknolojinin gelişmesi ile birlikte robotlar, minimal invazif ameliyatlar da dahil olmak üzere birçok tıbbi alanda kullanılmaya başlanmıştır. Bu tez, 'Cerrahi aletlerle yönlendirilebilen robot yardımlı endoskop kontrol sistemi (NeuRoboScope)' isimli bilimsel araştırma projesinin bir parçasıdır. Proje kapsamında endoskopik hipofiz bezi ameliyatı vakası ele alınmıştır. Bu ameliyat sırasında, endoskobunu hareketi insanın burun boşluğundaki hassas dokular sebebiyle sınırlıdır.

Bu tezin kapsamında araştırma preoblemleri, (1) cerrah - robot ve (2) robot-hasta olmak üzere iki ana başlık altında toplanmıştır. Öncelikle doktorun endoskop tutucu robot ile olan etkileşimi ele alınmıştır. Uyumlu kontrolcünün parametrelerinin etkileri, tek serbestlik dereceli geri sürülemeyen bir cihazda deneysel olarak test edilmiştir. Bu etkileri nicel olarak karşılaştırabilmek için bir yöntem önerilmiştir.

Ele alınan ikinci araştırma konusu ise robot ve hastanın etkileşimidir. Etkili bir uyumlu kontrolcü tasarımı yapabilmek için insana ait burun dokusunun viskoelastik modeli çıkartılmıştır. Bu amaçla kadavra üzerinden ölçüm alabilecek taşınabilir bir düzenek önerilmiştir. Ayrıca ameliyat sırasında karşılaşılabilecek kuvvet ve moment limitleri tespit edilmiştir. Elde edilen bu bilgiler doğrultusunda, uzaktan kontrol edilebilen robot ile burun dokusu arasıda gerçekleşen uyumlu denetim, deneysel ve benzetim yöntemleri kullanılarak test edilmiştir. Belirli bir senaryo dikkate alınarak yapılan deney sonuçları göstermiştir ki, hassas dokular etrafında çalışacak bir robot güvenli bir şekilde kontrol edilebilir.

TABLE OF CONTENTS

LIST OF FIGURES

Figure **Page**

LIST OF TABLES

CHAPTER 1

INTRODUCTION

Minimally invasive surgery (MIS) is an alternative to traditional surgery. It has different approaches such as hypodermic injection (using the syringe), endoscopic surgery, percutaneous surgery which involves needle puncture of the skin, laparoscopic surgery which is commonly called keyhole surgery, a coronary catheter, angioplasty and stereotactic surgery. In endoscopic surgery, an endoscope and surgical instruments are inserted into the patient's body through small incisions. MIS technique has several advantages which make them very popular among surgeons and patients (Lanfranco et al., 2004). Many studies have shown that endoscopic surgeries result in decreased hospital stays, reduced trauma to the body and risk of infection, also minimal scars (Kim et al., 2002; Fuchs, 2002). Besides its various advantages, it also has few disadvantages such as limited range of motion at the surgical site which decrease dexterity, poor depth perception and hand-eye coordination, and reduced tactile sensation. In addition to these, the endpoint of the endoscope move in the opposite direction to the surgeon's hands due to the pivot point, this is referred in some studies as the Fulcrum effect (Camarillo et al., 2004; Gallagher et al., 1998; Nisky et al., 2012).

In the past two decades, robots are started to be used for many medical application including minimally invasive surgery to overcome these disadvantages. Using robots in medical interventions can offer benefits such as high accuracy, fine manipulation capability, good repeatability, high reliability and lack of fatigue of the surgeon.

The minimally invasive endoscopic pituitary gland tumor surgery is one of the challenging cases for the surgical robotics. The pituitary gland is an important hormone gland that controls several other hormone glands and in this way, it directly or indirectly affects the working mechanism of all organs in the body of a human. Any pathologies constructed around the pituitary causes serious health problems. The cure for this type of tumors is performed either by opening the skull for an open-brain surgery or by the application of an MIS method such as endoscopic surgery through the nasal cavity.

Since endoscopic surgery provides the visuals of the operational field from the closest distance from a wider visual angle, it is more convenient for the surgeons. Figure 1.1 shows the representation of the transsphenoidal surgery.

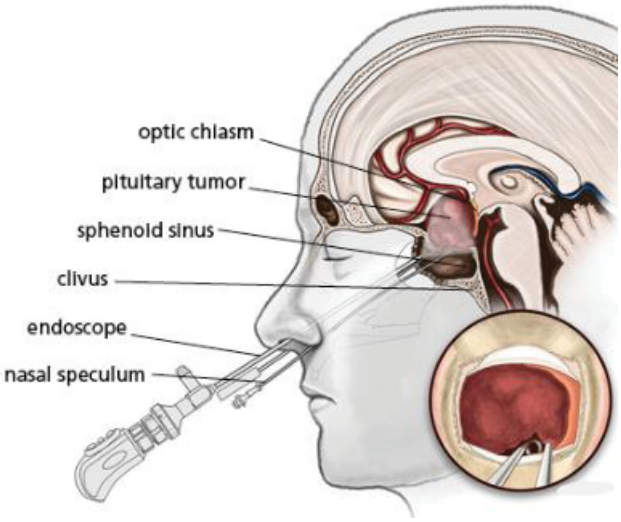

Figure 1.1. Transsphenoidal Surgery
(Source: PNI, 2018)

One of the major problems encountered during this operation is that the surgeon has to use his/her one hand to hold an endoscope to provide visual feedback. Since the surgery takes approximately 2-4 hours, the surgeon gets tired which decreases the success of the operation. In some cases, the assistant helps the surgeon by directing the endoscope while surgeon handles the other tools. This also causes synchronization problems between the surgeons.

With the motivation of the increasing efficiency of the procedure by giving third hand to the surgeon, a research project is initiated which is called "Robot-assisted endoscope control that can be controlled by the surgical tools (NeuRoboScope)". In this project, a robotic co-worker is designed to manipulate the endoscope during the surgery alongside the surgeon. This co-worker is directed by the surgeon via teleoperation and also through direct physical interaction.

The safety of the procedure is one of the key points of the project and this thesis is focused on the motion control of the system while meeting the safety requirements. The robot moves inside a human nasal cavity, hence, the motion is constrained and the system has to be comply with the environment in order not to apply excessive force to the soft tissue surrounding the endoscope. In addition to that, the surgeon has to be able to hold the robot and back-drive it during the surgery in the case of an emergency or a raised need.

The research problems that are addressed in this thesis are presented in two scenarios: (1) controlling the robot during the surgeon-robot interaction, and (2) controlling the robot during the robot - soft tissue interaction.

The first one includes investigating the effects of the controller parameters on the back-drivability performance of human operators. A task is defined to quantitatively compare the performance in terms of the energy efficiency and the accuracy.

The second research problem includes the human nasal tissue modeling in order to design an accurate controller. To acquire data from the human cadaver, a new hand-held measurement device is designed and the soft tissue models are obtained. After the soft tissue models are identified, the compliant controller is developed and tested in simulation environment and then, the controller is tested on a one degree-of-freedom (DoF) experimental set-up.

In the following Chapter 2, a review of the literature on compliant control algorithms, soft tissue modeling, and force sensors are presented. The controller design for the back-drivability is explained in Chapter 3. Modeling of the soft tissue with the newly designed measurement device is presented in Chapter 4. The compliant controller designed for the robot-soft tissue interaction is proposed and the test results are given for a case study in Chapter 5. In Chapter 6, conclusions and findings are listed and discussed, and future works for possible improvements on compliant controller design for teleoperated surgical robots are addressed.

CHAPTER 2

LITERATURE SURVEY

Medical robotics is becoming one of the hot topics among the researchers in varying application areas from rehabilitation robots to magnetically driven micro-robotic surgeries due to their promising technologies. In this wide range of application, this survey is focused on minimally invasive surgeries (MIS). Firstly, a general overview of MIS systems that are developed in the previous years are given. Later in this chapter, the control strategies that can be applied in MIS systems for compliant control of the robot in constrained environments are reviewed. Forces sensors that are used in compliant control of robotic surgery systems are reviewed by presenting their sensing techniques, limitations and placements. Finally, since the controllers that are reviewed are model-based controllers, the environment (which is the soft tissue in the MIS systems) modeling techniques are investigated.

2.1. Robotics in Minimally Invasive Surgery

Surgical robots can be classified in 3 separate roles as they are reviewed in (Camarillo et al., 2004). First one is the passive role which has limited act on surgery and has minimal risk. Secondly, the restricted role which is responsible for a more invasive task with higher risk. As an example, Automated Endoscopic System for Optimal Positioning (AESOP) can be considered as a restricted system. It has voice controller for providing the demands to the robot to adjust the position of the endoscope (Allaf et al., 1998). Since the robot has constant contact during the surgery, it is not passive; however, it is only used for imaging which does not involve any invasive manipulation. Therefore, it can be considered as a restricted system (Stoianovici, 2000). The last class is an active role which has higher risk and responsibility. There is a trade-off between autonomy and the robot role. Computed tomography (CT) scan as an imaging method can be an example to this with the high autonomy and passive role. On the other hand, one of the best known commercial surgical robot *da Vinci* (IntuitiveSurgical, 2018) has active robot role with low autonomy.

Surgical robots can be also categorized by using a different taxonomy (Taylor and

Stoianovici, 2003; Dario et al., 2000; Tavakoli, 2008). Two main categories are augmenting devices and surgical assistants. Augmenting devices are the ones that are responsible for primary tasks such as the invasive parts of the surgery. Supporting devices are used for secondary tasks such as positioning of the endoscope in MIS.

Hand-held tools are one of the augmenting devices as they involve minimal changes in operating room also without any robotic arm they cannot be locked in position. The tool presented in Payne and Yang (2014) has a steerable tip with sensors for detecting to tip's interaction with the tissue and this device has semi-automatic collision avoidance feature. Another hand-held device that allows force control is developed in (Yuen et al., 2009), to track the motion of a beating heart. Cooperatively controlled tools are also considered as augmenting tools. These devices can be active or passive. The surgeon and the robot both hold the surgical device in these type of augmenting devices. One of the examples of this type of robots is the Steady-Hand robot which allows steady manipulation of a surgical tool and can provide scaled force-feedback that augments the surgeon's sense of touch (Taylor et al., 1999).

Teleoperated tools are one of the subcategories of augmenting devices. In teleoperated surgery, movements of a surgical robot are controlled via a surgeon's console. ,Well-known examples of these robots are da Vinci and Zeus systems. In these dual handed teleoperated systems, two slave robots manipulate the surgical instrument while another slave robot controls the camera. These robots allow precise movements, filter out hand tremors and increase dexterity (Tavakoli, 2008). The last augmenting type devices are autonomous tools which can perform certain tasks autonomously. RoboDoc system can be considered in this category. It is used in orthopedic surgery and it has an image-guided system to generate the cutting path. It requires a preoperative process such that surgeon must locate the landmarks to synchronize with CT images. This preoperative part and manual registration process decrease the level of autonomy (Camarillo et al., 2004).

In some laparoscopic surgeries, an assistant surgeon needs to hold the endoscope or other surgical instrument and that causes fatigue and loss of accuracy on position in the surgery. To resolve this problem, a common use case of passive supporting devices is a positioning stand on which the endoscope can be locked at required position without the need of an assistant surgeon. As the last category of supporting devices, the study in (Dai et al., 2016) can be given as an example for autonomous supporting devices. This is an endoscope holder with automatic tracking feature. It has optical positioning device to track specified surgical instrument. By the proposed control algorithm, motion of the endoscope is claimed to be exact, in real-time and with the usage force sensor it is claimed

to be safe. Another autonomous supporting device is presented in (Bauzano et al., 2013). The proposed control provides a solution to combining hand assisted laparoscopic surgery and single incision laparoscopic surgery. In this system, upper auto-guided velocity planner is connected to a low-level force feedback controller. Auto-guided velocity planner based on behavior approach computes a collision free trajectory of the surgical instrument tip and force feedback controller uses this trajectory for performing the instrument displacement by taking into account the holonomic movement constraints introduced by the fulcrum point. The aim is minimizing the exerted force on abdominal wall.

In above-mentioned ways of categorizations consider either the degree of autonomy or the realized tasks. The NeuRoboScope robot, is an active endoscope holder which can be controlled teleoperatively. Due to its autonomy level and the role, it can be considered as a restricted role in the first type of classification. On the other hand, NeuRoboScope should be classified as an active supporting device in the second type of taxonomy.

2.2. Compliant Controllers for Safe Physical Interaction in MIS

Using robots in MIS offers various benefits such as increased dexterity, high reliability, increased manipulation capability and repeatability. However, they must provide a solution to the safety issue which is one of the main problems in using robots in MIS. To avoid excessive contact force to the environment, the robotic surgical instrument must display compliant behavior. Control of the position is not sufficient to solve this problem alone hence, control of the dynamic behavior is also required (Hogan, 1985). Force and position control strategies have been developed and studied for many years. The robot force control algorithms are classified by Zeng and Hemami (1997) as fundamental and advanced control strategies. Some of the main categories of fundamental methods are stiffness control, impedance control, admittance control, explicit force control, implicit force control and hybrid force/position control (Whitney, 1985).

2.2.1. Fundamental Compliant Control Structures

Compliant control can be realized by passively or actively. Passive control compensates the interaction forces by using spring - damper compositions on the end effector instead of using control algorithm. Passive stiffness control is mainly hardware based thus it can be used in specific tasks and it is mechanically complex also the stability is

guaranteed (Wang et al., 1998).

On the other hand, the active controller adjusts the end effector's stiffness in different directions due to the specific task (Dede, 2003). This can be achieved by adjusting joint stiffness through control of each joint torque. Active controllers are software based, therefore it can be used in general applications. Instabilities may occur in this control strategy due to uncertainties in the model of the environment. Fundamental control structures provide good results with the known environment parameters. Advanced compliant control structures are proposed in the literature for dynamically changed or uncertain environments.

2.2.1.1. Stiffness Controller

Stiffness controller relates the position with the applied force by using zeroth order impedance term. This controller is also known as compliance controller which is reciprocal of the stiffness term as a definition.

Figure 2.1 presents the principle of stiffness control. In this figure, X_D is desired position reference, J is the Jacobian matrix, X_E is the environment displacement, τ is the control input, $H(s)$ is the transfer function of the force sensor, X and $\dot{X}$ are the end-effector's position and velocity vectors. K_P, K_V, K_E are represents the position feedback gain, the velocity feedback gain and the net stiffness between the environment and the end effector, respectively.

K_{F1} is the compliance matrix, which modifies the position command. Although accurate position control requires high stiffness, the force control requires that the system stiffness be as low as possible. Therefore, end effector's stiffness should be controlled in various directions depending on the task (Dede, 2003).

The first implementation of the stiffness control on the continuum robots, which are a relatively novel class of manipulators that are increasingly being adapted to medical applications, is presented in (Mahvash and Dupont, 2011). This study shows that desired stiffness of the end effector could be achieved independently in the lateral or bending directions. Reduction of the stiffness of the end effector can provide safe navigation inside the delicate tissue. However, in a case of tissue manipulation, a higher stiffness may be advantageous.

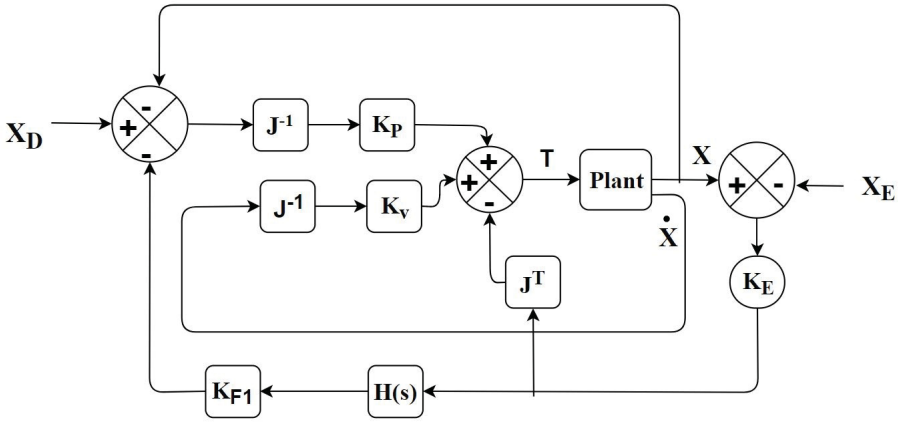

Figure 2.1. Block Diagram of stiffness control
(Source: Whitney, 1985)

2.2.1.2. Impedance Control

Another widely studied control strategy is impedance control. Under the applied external force, a structure has a resistance to the motion which is commonly named as mechanical impedance, Z_m. It provides a relation between forces acting on the structure and its velocity (Khan et al., 2014). In the frequency domain, second order impedance can be defined as in Equation 2.1 and the control scheme is presented in Figure 2.2.

$$\begin{aligned} F(s) &= Z_m(s)\dot{X}(s) \\ sZ_m(s) &= \frac{F(s)}{X(s)} = Ms^2 + Bs + K \end{aligned} \tag{2.1}$$

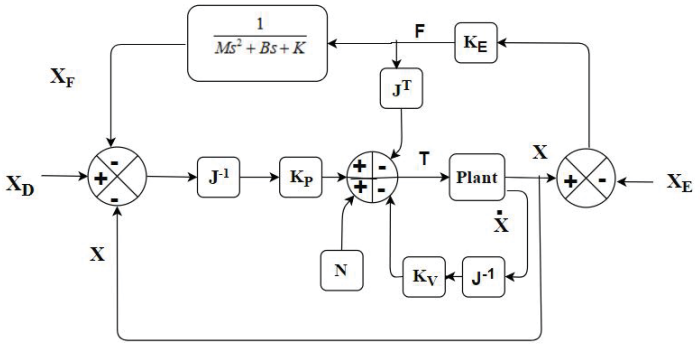

Figure 2.2. Block diagram of position based second order impedance control

In the figure, M, B and K coefficients represent the desired mass, damping and

stiffness terms, respectively. The term N is added to the control input in order to compensate for the nonlinear gravity, centrifugal and Coriolis effects.

Since the dynamics of a second order system are well studied and the higher order systems cause difficulties to obtain measurements, sensor based impedance controller requires second order system at most (Volpe and Khosla, 1993). First order impedance control contains damping and stiffness terms while zeroth order impedance deals only with the stiffness term.

A lightweight surgical manipulator called MIRO is developed to control the interaction with the humans in unstructured environments (Hagn et al., 2008). It has impedance control mode to guide the robot to the desired position by hand. Due to its kinematic redundancy, the inner joints of the robot can be controlled in compliance mode by using virtual springs to impose constrained forces which gives additional safety to the system working with the humans cooperatively.

2.2.1.3. Admittance Control

Admittance control is a force tracking control method. In contrast with the mechanical impedance, admittance control takes force input and makes the modification on velocity. In this control strategy, a force compensator guarantees the tracking of force set point. Mechanical admittance A, can be defined as reciprocal of mechanical impedance as presented in Equation 2.2 where Figure 2.3 shows the structure of admittance controller.

$$A = \frac{1}{Z_m} \tag{2.2}$$

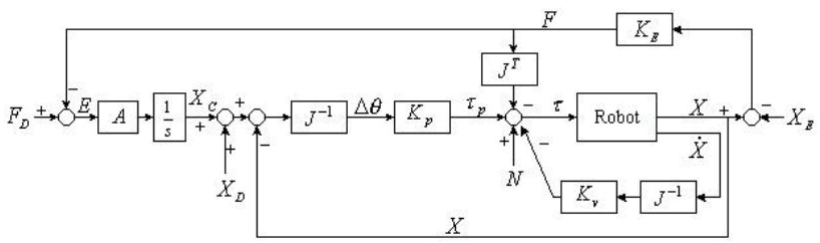

Figure 2.3. Block diagram of admittance control
(Source: Dede, 2003)

Recently, in Kim et al. (2016) adjustable admittance force feedback control is proposed for bone fracture reduction robotic surgery. The study shows that using double force / torque sensors and adjustable admittance increase the protection bones against the damage and the stiffness of the environment affects the performance of the force feedback algorithm. Also, they provide force feedback to the surgeon to feel the environment. The system, which includes environment, robot, and a human arm, is modeled as in Figure 2.4.

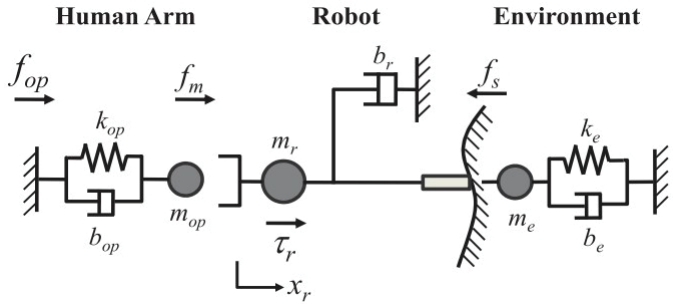

Figure 2.4. Dynamic model of the interaction
(Source: Kim et al., 2016)

Another study presents a hybrid system approach, which incorporates impedance and admittance control (Ott et al., 2010). In contrast to the impedance controller, admittance control provides relatively good performance for soft environments but results in contact instability for stiff environments. An ideal controller should achieve consistently reliable performance, without being affected by the environment stiffness. This approach allows to continuously switch and interpolate between these controllers to overcome this limitations. Control structure of the proposed approach is presented in Figure 2.5.

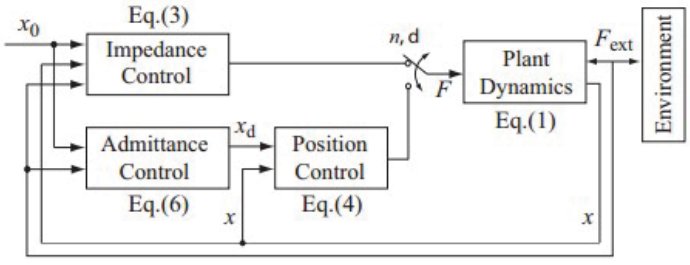

Figure 2.5. Impedance and admittance controller switching
(Source: Ott et al., 2010)

Researchers in (Osa et al., 2014) present a hybrid master-slave velocity control and admittance control for safe remote robotic surgery. Contact force must be required for

some tasks such as peeling off membranes and holding organs to insert surgical needles. However, to avoid excessive contact force, the robotic surgical instrument must behave compliantly. To meet these requirements, the proposed controller switches between these two controls adaptively and stable. Figure 2.6 shows the control structure.

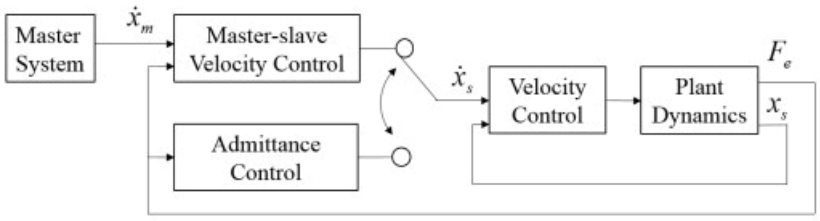

Figure 2.6. Hybrid admittance control scheme
(Source: Osa et al., 2014)

2.2.1.4. Implicit and Explicit Force Control

Another approach for force control method is explicit force controller which includes two categories as force based and position based (Zeng and Hemami, 1997). Force based control structure is presented in Figure 2.7. In this controller, unlike the previous techniques, directly measured force feedback is used to obtain force error. The main idea of the controller is to eliminate the error by defining force control law and it has a structure similar to an admittance controller.In this figure, F_D is desired force value, J^T is the transpose of the Jacobian matrix, N is the velocity related nonlinear terms and τ_p is the command torque.

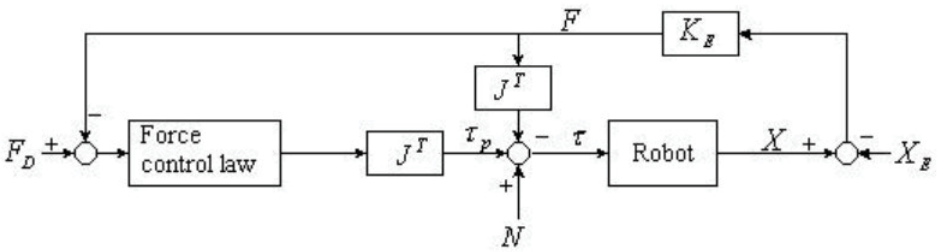

Figure 2.7. Block diagram of force based explicit controller
(Source: Dede, 2003)

The second category is position based implicit force control method which involves no force sensor, instead, desired stiffness is obtained by adjusting the joint servo gains K_p (Whitney, 1985). Figure 2.8 shows implicit force control structure. In this controller, the position is controlled by using pre-defined position to achieve desired force.

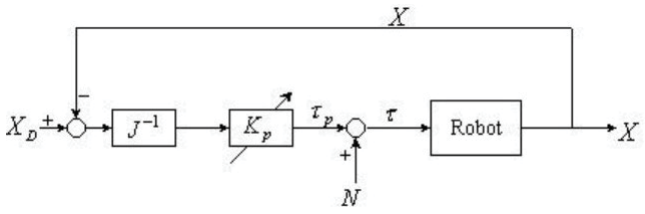

Figure 2.8. Block diagram of the position based implicit controller
(Source: Dede, 2003)

2.2.1.5. Hybrid Position / Force Control Structures

Hybrid position / force control and hybrid impedance control methods combine the applied force / torque with position data based on two complementary workspaces which can be defined as position and force sub-spaces (Dede, 2003).

Different control algorithms can be applied to these sub-spaces due to the defined task (Raibert and Craig, 1981). The combination of the impedance controller and the hybrid position / force controller is proposed in (Anderson and Spong, 1988) as hybrid impedance control strategy. Figure 2.9 shows common structure of hybrid position/force control.

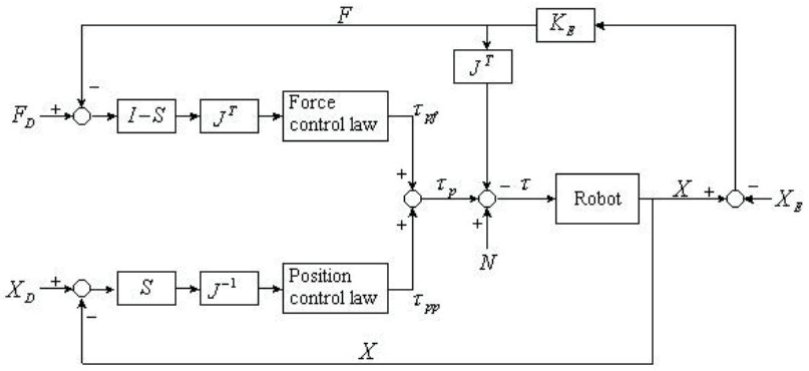

Figure 2.9. Block diagram of hybrid position/force controller
(Source: Anderson and Spong, 1988)

In the figure, S is the compliance selection matrix which determines the force or position control for each sub-space. The S matrix can be constant or depend on the configuration or can continuously change with time (Fodor and Gabor, 1999). This controller allows the desired force is maintained in some directions while in the remaining directions, a position demand is tracked.

In MIS it is required that there is no sideways motion at the point where the robots enter the patient's body. To satisfy this requirement, researcher studied on two main solutions. In the first one, a remote center of motion (RCM) is obtained by mechanically as in the da Vinci robot. And the second one is obtaining RCM by controlling the robot. A study in (From et al., 2014) presents this type of solution to maintain safety in the MIS. They proposed hybrid compliant control architecture for endoscopic surgery which satisfies the zero-lateral velocity requirement at the entry point for serial manipulators. Adjusting the Jacobian matrix is realized by using selection matrix in certain directions.

2.2.2. Advanced Compliant Control Structures

Due to the existence of complex tasks and uncertainties such as uncertain environment, external disturbances, unmodeled dynamics...etc., more advanced force control algorithms are developed. These methods are based on fundamental strategies. In the aforementioned controllers, many strict assumptions are made to simplify the model, which may reduce the effectiveness of the control algorithm based on such a simplified model. Hence, to overcome the uncertainty in the model parameters, adaptive control is a desirable choice. There are two main types of adaptive control schemes, *i.e.*, model reference adaptive control (MRAC) and self-tuning (ST) adaptive control which can be further classified as either direct or indirect adaptive control (Slotine and Weiping, 1991).

Roy and Whitcomb (2002) proposed an adaptive force control algorithm for velocity/position controlled robots which are in contact with surfaces of unknown linear compliance. This proposed controller guarantees global asymptotic convergence of force trajectory tracking errors to zero.

In a recent study (Ebrahimi et al., 2016), a nonlinear adaptive impedance sliding mode controller is developed in order to make the impedance of the robot converge to the pre-defined impedance which is a mathematical representation of a sino-nasal tissue.

Another group of researchers developed a tank-based approach to impedance control with variable stiffness (Ferraguti et al., 2013). The proposed approach controls the exchanged energy during the task by creating a reservoir of energy, which is called tank,

in case of time varying stiffness to achieve stability. One of the proposed application of the presented algorithm is the reproduction of surgeon's behavior during a puncturing task.

In a similar approach study in (Ferraguti et al., 2015), extend the previous controller and applied admittance controller where inertia, stiffness, and damping can all be passively changed. They both use tank based energy approach to achieve stability. The reason that researchers have developed these advanced control structures is standard impedance and admittance control schemes cannot guarantee a stable interaction when time-varying interactive behaviors need to be implemented.

Learning controller algorithm is another advanced force control approach in the literature. This controller is applied when the robot performs the same task repeatedly (Dede, 2003). The algorithm takes the position, velocity or acceleration error as an input for learning the adjust control command to guarantee the motion and force tracking and robustness.

As an example, Kim, B. et al. (2010), developed impedance learning algorithm for robotic contact tasks. Proposed learning method employs the impedance control, based on the equilibrium point control theory and reinforcement learning to determine the impedance parameters for contact tasks. Making use of this controller, researchers optimized the performance of contact task such as door opening, point to point contact and ball catching by using learning algorithm.

2.3. Force Sensing Techniques

Determining forces and torques is the first technical challenge to control the force between the tool and soft tissue. To prevent applying excessive force and increasing the compliance with the environment, some sensing techniques are developed in the literature. Due to the dexterity of the MIS, force sensors have some constraints such as size, waterproof, electrical passivity, and sterilizability. As Puangmali et al. (2008) reviewed, placement of the force sensor is an important matter. Four placement locations are possible.

1. Near or at the actuation mechanism:

It is possible to measure forces by evaluating the stress of the mechanical linkages or responses of the actuators. However, measurement accuracy is reduced due to the force

transmission through mechanical linkages, friction, backlash, gravity, and inertial effects (Puangmali et al., 2008; Yip et al., 2010).

2. On the instrument shaft outside the patient's body:

This type of placements does not have aforementioned constraints because force does not pass through on different linkages. But the friction forces are becoming much more important. For this kind of placement, friction compensation should be used. (Puangmali et al., 2008).

3. On the instrument shaft inside the patient's body:

For this location, force measurements are not affected by the reaction and friction forces generated on fulcrum point. Recently, researchers focused on this type of sensors (Puangmali et al., 2008; Berkelman et al., 2003; Bicchi et al., 1996). However, the size of these sensors should be minimized.

4. At the instrument tip, such as on a gripper jaw:

This method provides most direct force sensing, however, it requires severe space limitations. Only instruments which have either a large gripper or extremely small sensing elements can be considered for this case. In the literature, this placement is preferred for laparoscopic grippers and optical based force sensing methods (Watanabe et al., 2014; Peirs et al., 2004; Yip et al., 2010).

2.3.1. Constraints of Using Force Sensor in MIS

There are also important constraints for the force sensor in MIS. For the case that the force sensor is located inside the patient body, a waterproof seal is required in order to protect the sensor from the pressurized blood. Also, surgical instrumentation must be electrically passive to avoid disrupting normal electrical activity in the heart (Yip et al., 2010). Optical based force sensing technology is a promising alternative to this issue.

Since MIS requires small incisions, force sensor has size constraints too. Another important issue is material constraints due to the imaging technology. Some metals tend to create artifacts in ultrasound images and not suitable for MR imaging techniques (Yip et al., 2010).

Sterilizability of the designed sensor is an essential constraint for the operating room. Presently, steam sterilization known as an autoclave is a standard method widely

applied to sterilize surgical equipment. This sterilization method commonly employs saturated steam to heat the equipment up to 121 C at 103 kPa above the atmospheric pressure for at least 15 min. (Puangmali et al., 2008). These conditions can also potentially damage sensors or electronic circuits.

2.3.2. Sensing Methods

According to specified requirements, several force sensing techniques are developed in recent years. One of the simplest sensing methods is displacement-based sensing (Richards et al., 1999). This method detects the displacement of an elastic element to evaluate applied force. However, this technique requires a good knowledge about the stiffness of the elastic element and good calibration.

Second sensing method is current-based sensing. This technique considers the force exerted on the motor axis as a disturbance and by obtaining current value, force is being measured. In MIS, Tholey et al. (2004) investigated this sensing method with a specially designed laparoscopic grasper. Although this method is a simple approach to force sensing, it does not provide a very accurate measurement (Puangmali et al., 2008). Also, several compensations and disturbance observers are necessary to increase accuracy (Katsura et al., 2007).

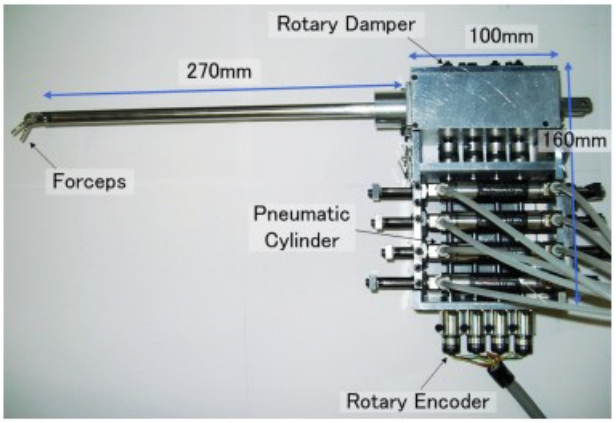

Figure 2.10. Pneumatic driven forceps
(Source: Tadano and Kawashima, 2006)

Pressure-based sensing is an alternative way to sense for by using a pneumatic equipment. Forces can be measured by similar way to current based approach and also it is possible to detect force by measuring the pneumatic pressure. Tadano and Kawashima

(2006) have developed four DoF pneumatic-driven forceps that possess force sensing capability as shown in Figure 2.10.

Another way to measure force is resistive based sensing which is the most common sensing method in the literature. The strain gauge is usually bonded to a flexible structure to obtain accurate force measurement and it changes the electrical resistance as a consequence of resulting strain. This allows the measure force electrically. However, there is always a tradeoff between the stiffness of the structure and the sensitivity of the measurement (Craig, 1989). Berkelman et al. (2003) developed the miniature force sensor in Figure 2.11 to measure contact forces at the tip of a microsurgical instrument in three dimensions. The principal features of proposed sensor are its small size and a novel configuration of strain gauges in order to measure forces isotropically at the instrument tip. Also, Prasad et al. (2003) developed a two DoF force sensing sleeve that can be integrated with a variety of 5 mm laparoscopic instruments. Full bridge strain gauges were used as its sensing elements.

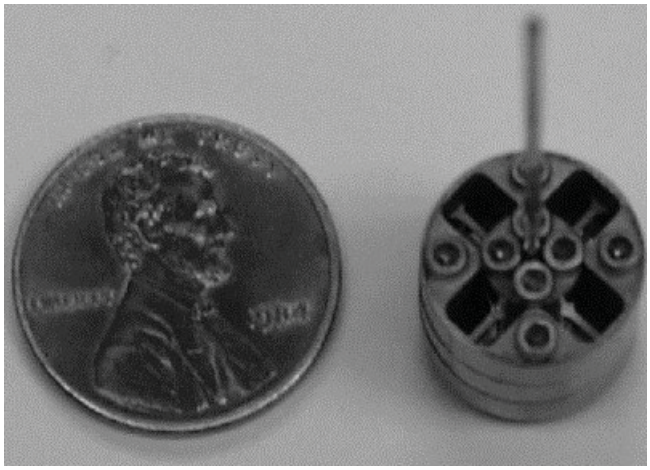

Figure 2.11. A miniature force sensor
(Source: Berkelman et al., 2003)

Another sensing method is capacitive-based sensing. This method is the most powerful one for detecting extremely small deflection of structures (Puangmali et al., 2008). Gray and Fearing (1996) developed capacitive sensor array for sensing forces on endoscopic tools. Deformations due to contact forces that cause changes in capacitance of the sensing elements allow the forces to be detected using oscillatory circuits. Howe et al. (1995) developed a remote palpation system for helping the surgeons to search for hidden arteries and tumors buried inside tissues during MIS procedures by using capacitive-based sensing.

Piezoelectric-based sensing, a sensitively generate voltages when their structures

are deformed due to compression. The capability to produce voltages of piezoelectric sensors is better than most other sensors (Puangmali et al., 2008). In addition to that, no electrical power is needed to be supplied to the sensing elements. However, these sensors are only sensitive to time-varying force quantities. They do not provide accurate measurements for static force. For an application in MIS, Dargahi et al. (2000) applied such material in the development of a micro-machined tactile sensor that can be equipped with a jaw of endoscopic graspers. Figure 2.12 shows the prototype endoscopic grasper integrated with the tactile sensor.

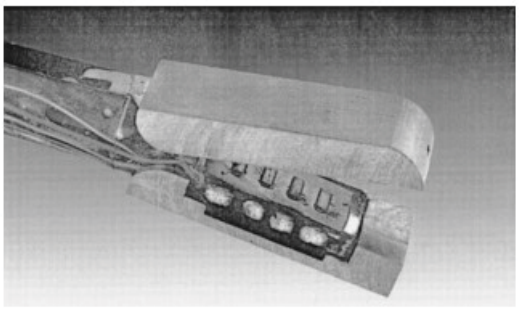

Figure 2.12. Endoscopic grasper with developed tactile sensor
(Source: Dargahi et al., 2000)

One of the several sensing methods is vibration-based sensing. This method can measure dynamic responses. Fetter et. al. developed vibrotactile sensor. It has an alternate current (AC) excitation coil which generates an oscillatory magnetic field to induce vibration on a permanent magnet (Petter et al., 1996). In literature, there are several studies on evaluating mechanical properties of human tissue by using vibration based sensing method. (Omata et al., 2004; I. Baumann, 2001).

The last method of force sensing is optical-based sensing. This method is firstly proposed by Hirose and Yoneda (1990). In this method, fiber optic cables are used for carrying information to the sensor instead of electrical wires. The light transfers through fiber optic cables to the transducer which modulates the light in proportion to the value of the force being measured.

Yip et al. (2010) developed miniature uniaxial force sensor based on an optical sensor that can be used for beating heart surgery. Due to the electrical passivity and 3D imaging constraints for heart surgery they used optical-based sensing method. Figure 2.13 presents sensor components and prototype, respectively.

Another study on this type of sensor is presented by Peirs et al. (2004). They presented tri-axial force sensor and force range measurements for the skin, muscle, and

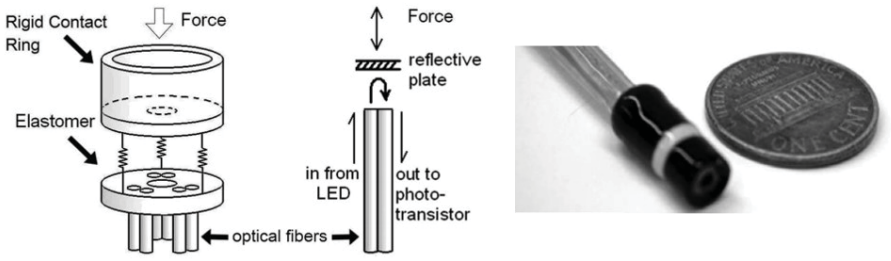

Figure 2.13. A miniature unaxial force sensor
(Source: Yip et al., 2010)

liver. Also, Watanabe et al. (2014) developed a force sensing system that can be used with a thin fiberscope/endoscope which is shown in Figure 2.14. Measurement is realized by detecting highly elastic fiber's deformation, which is attached to the tip of the endoscope, by using a camera. Although the system has a resolution of less than 0.01 N and force range of 0-0.2 N, it can measure force only in one direction.

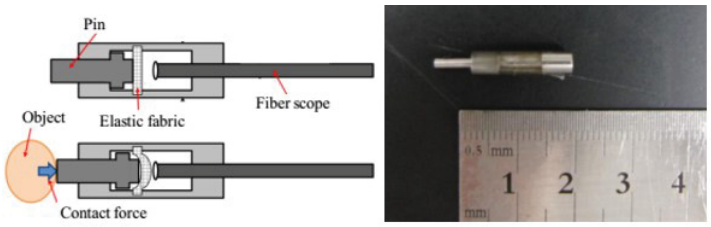

Figure 2.14. A force sensing system for endoscope
(Source: Watanabe et al., 2014)

Besides the aforementioned force sensors which are developed for specific cases, several commercially available force / torque sensors are commonly used for the compliant control purpose. The ranges and the resolutions of these sensors are varying in a wide range and selection should be done by considering the application. In MIS surgery,the end effector of the robot is expect to interact with the soft tissue hence, the force sensor must be able to sense relatively small forces.

2.4. Soft Tissue Modeling

Safety of the procedure is one of the main issues in robotic MIS. Understanding the interaction between medical tools and living tissues can result in more precise and reliable controller design. One of the first attempts to designing force controller based on

tissue model is presented in Yuen et al. (2010) by assuming interaction is purely elastic. However, it is not realistic for the biological tissues (Fung, 2013). Several soft tissue models are proposed to define relatively more accurate tool-tissue interactions. These interaction models can be classified as finite element methods (FEM) and analytical methods such as viscoelastic methods, fractional models, and high order models (Misra et al., 2008).

Deformation accuracy and computation time are the two main constraints for modeling the interaction and Figure 2.15 represents the different types of applications according to these constraints (Delingette, 1998; Moreira et al., 2014).

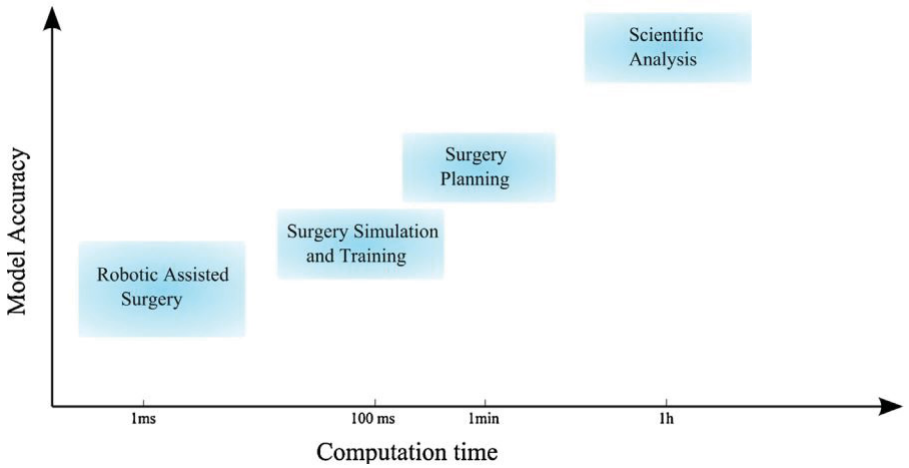

Figure 2.15. Relation between model accuracy and computational time for different type of applications (Source: Moreira et al., 2014)

In the case of scientific analysis of the tissue and surgery planning, more precise FEM's are suitable in spite of their longer computational time. On the other hand, robotic assisted surgeries require faster computational time for real-time applications as a result of that analytical models are more adequate.

2.4.1. Finite Element Method

The FEM is a numerical technique which has been used to simulate soft tissue deformation by solving the equations of continuum mechanics. FEM techniques provide solutions to complex problems such as modeling of anisotropic, inhomogeneous biological tissues. In general, increased mesh number provides better accuracy which also increases the computation effort (Misra et al., 2008). Therefore, these techniques are not

fully compatible with real time applications. However, the study presented in Basdogan et al. (2001) proposed optimization of linear elastic FEM for real time surgical simulation. Several researchers have studied linear elastic FEM for non-invasive operations (Cotin et al., 1999; Gladilin et al., 2001; Kühnapfel et al., 2000; Kerdok et al., 2003).

Since FEM requires relatively more time to obtain accurate solutions and these methods are more suitable for scientific analysis rather than designing compliant controller, analytical methods are considered for the MIS surgery case.

2.4.2. Analytical Methods

A conventional way to represent the viscoelastic properties of tissue is using combinations of an ideal damper and spring components. These models are comprehensively studied and compared in literature (Moreira et al., 2014; Misra et al., 2008; Pappalardo et al., 2016) and schematic representation of some of these models are given in Figure 2.16. In the figure, $F(t)$ and $x(t)$ represent the applied force and the deformation of the tissue, respectively.

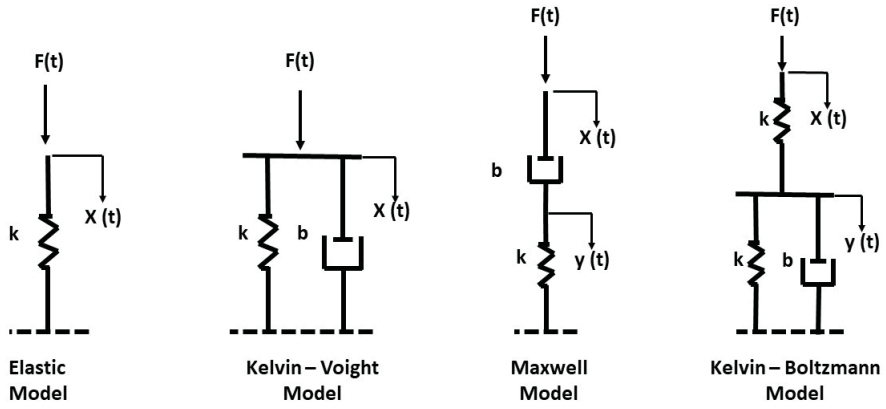

Figure 2.16. Commonly used analytical models

The simplest model is a purely elastic model with single ideal spring model and it's governing equation given in Equation 2.3 where k represents the spring coefficient.

$$F(x) = kx(t) \tag{2.3}$$

The Kelvin-Voight model consists of a parallel connection of an ideal damper and an ideal spring. The interaction force is presented in Equation 2.4 where b is the damping

coefficient.

$$F(t) = b\frac{dx(t)}{dt} + kx(t) \tag{2.4}$$

On the other hand, the Maxwell model is composed of a serial connection of ideal spring and ideal damper and its mathematical model is presented in Equation 2.5 where $\alpha = \frac{b}{k}$.

$$F(t) = k\frac{dx(t)}{dt} - \alpha\frac{dF(t)}{dt} \tag{2.5}$$

Serial combination of elastic and the Kelvin-Voight models describes the Kelvin-Boltzmann model and the corresponding mathematical model is represented in Equation 2.6 where $\alpha = \frac{k_2}{k_1+k_2}$, $\beta = \frac{k_1k_2}{k_1+k_2}$, $\gamma = \frac{b}{k_1+k_2}$ and k_2 is another spring constant.

$$F(t) = \beta x(t) + \alpha\dot{x}(t) - \gamma\dot{F}(t) \tag{2.6}$$

Viscoelasticity has two important features such as relaxation and creep. When a body is strained suddenly and maintained constant, the induced stress is decreased with time. This phenomenon is called stress relaxation. On the contrary, if a sudden stress is applied on the body and it is maintained constant, the body continues to deform. This is called creep phenomenon (Fung, 2013).

These viscoelastic models differ from each other by their ability to mimic tissue behaviors. Pre-studied experiments show that (Misra et al., 2008), The relaxation behavior of the Maxwell model provides acceptable relaxation behavior, but its creep behavior is insufficient. On the contrary, the Kelvin-Voight model has a good first order approximation of creep but its stress relaxation behavior is inadequate. On the other hand, the Kelvin-Boltzmann model provides relatively good behaviors of both creep and stress relaxation.

Hunt and Crossley (1975) presented that linear viscoelastic models show inconsistencies against physics of contact and they proposed a non-linear model which is represented in Equation 2.7 where λ is the damping parameter related to the coefficient of restitution.

$$F(t) = kx^n(t) + \lambda x^n(t)\dot{x}(t) \tag{2.7}$$

Combinations of mass, spring and damper are also studied in the literature to model tissue deformations (Keeve et al., 1996; Castaneda and Cosio, 2003).

In addition to the mechanical model, other modeling approaches have been developed. One of them is called Long Element Model (LEM) which has two-dimensional distributed elements filled with an incompressible fluid (Misra et al., 2008). This approach provides a real time solution for complex deformable bodies, multi modal interactivity and stable haptic interfaces. Sundaraj et al. (2002), proposed LEM to simulate human tight and Balaniuk and Salisbury (2002) applied LEM to deformable bodies.

Since FEM is not suitable for real time applications and it is very sensitive to mesh resolution, De et al. (2005) proposed a meshless technique which is called Point Collocation based Method of Finite Spheres (PCMFS) for modeling interaction in MIS. Furthermore, they extended the concept to Point Associated Finite Field Approach (PAFF) which assumes linear elasticity for modeling soft tissue (De et al., 2006).

Fractional calculus can provide an efficient model for describing the behavior of viscoelastic dampers using a small number of parameters that occur in biological tissues. Several researchers have studied FO models to describe viscoelastic properties of soft tissue. Meral et al. (2010) developed a fractional order Voigt model in order to better simulate the surface wave response of soft tissue-like material phantoms. Lewandowski and Chorazyczewski (2010) presented both the Kelvin–Voigt fractional model and the Maxwell fractional model to identify parameters and they derived the equations of hysteresis curves for fractional models. Craiem et al. (2008) proposed an alternative relaxation function based on fractional calculus theory to describe stress relaxation experiments in strips cut from healthy human aortas.

CHAPTER 3

CONTROLLER DESIGN FOR ACTIVE BACK-DRIVABILITY

In the robotic pituitary gland surgery, there might be a case that the surgeon needs to back-drive the robotic arm by holding and relocating the endoscope. The endoscope can be relocated if the system is passively back-drivable or the back-drivability is satisfied by the use of a controller. This type of controller is named as admittance control which receives the input from the human in terms of force and this information is used for back-driving. The selection of the admittance term is the key point of this controller design.

In this chapter, an experimental study is presented that is carried out to determine the effects of the admittance terms on back-drivability. In the next section, the experimental set-up is described then, dynamic model of the experimental set-up is formulated, parameter estimation study is presented and finally the controller design is explained. In the second section of this chapter, the experimental task is defined for the investigation of the effects of admittance terms. In the third and fourth sections, the results of the user evaluation experiments are given and the outcome of the experiments are presented and discussed, respectively.

3.1. Experimental Set-up

In order to investigate the effects of the admittance terms, a non-back-drivable one degree of freedom device is designed (Işıtman et al., 2017). To obtain linear motion, a DC motor (HITACHI D06D401E) with an optical encoder (AEDA-3300AT) is assembled to a lead screw linear stage which has 220 mm workspace. The quadrature encoder provides $16384\frac{count}{rev}$ and the lead screw stage has 5 mm pitch which results in $0.3\frac{\mu m}{count}$ resolution.

A precision grasp type handle is mounted on top of linear stage as an interface for the human subject's hand. To measure the applied force from the subjects, a Kistler (type 9017B) 3 DoF force sensor is placed below the handle which is shown in Figure 3.1. The calibration of the force sensor is realized by using the ManuWare software. An external force is applied to the sensor then by using this software a scale factor is calculated as $9.44\frac{N}{V}$ which works in range of $\pm$10 V.

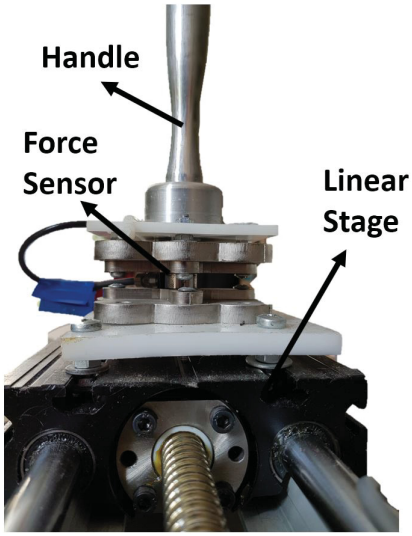

Figure 3.1. The placement of the force sensor

For the data acquisition and control purpose, NI MyRIO 1900 data acquisition (DAQ) system is used. This DAQ system has a 12-bit ± 10 V analog input/output and digital input/output pins to acquire the force data and provide the analog outputs to the Maxon 4-Q-DC servo-amplifier. A 30 V DC power supply is used. Figure 3.2, shows the experimental set-up with all the components.

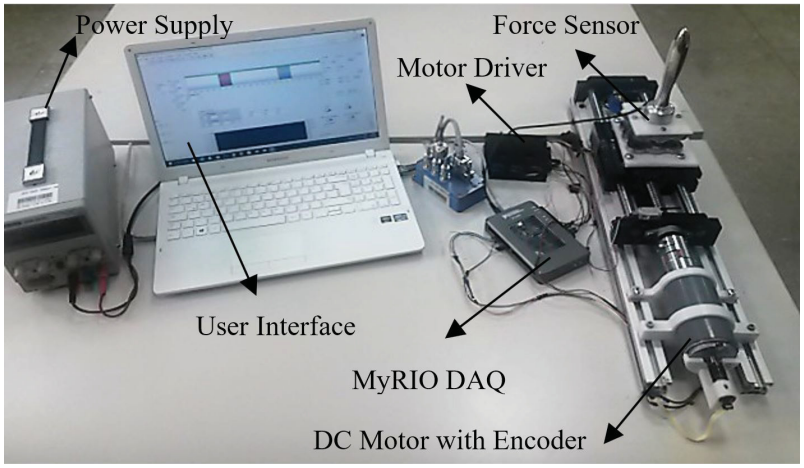

Figure 3.2. The experimental set-up
(Source: Işıtman et al., 2017)

Control algorithm and graphical user interface are developed in NI LabView Software with Control Design and Simulation module and Real-Time module. Force readings are acquired and control algorithm is executed at a sampling rate of 1 kHz.

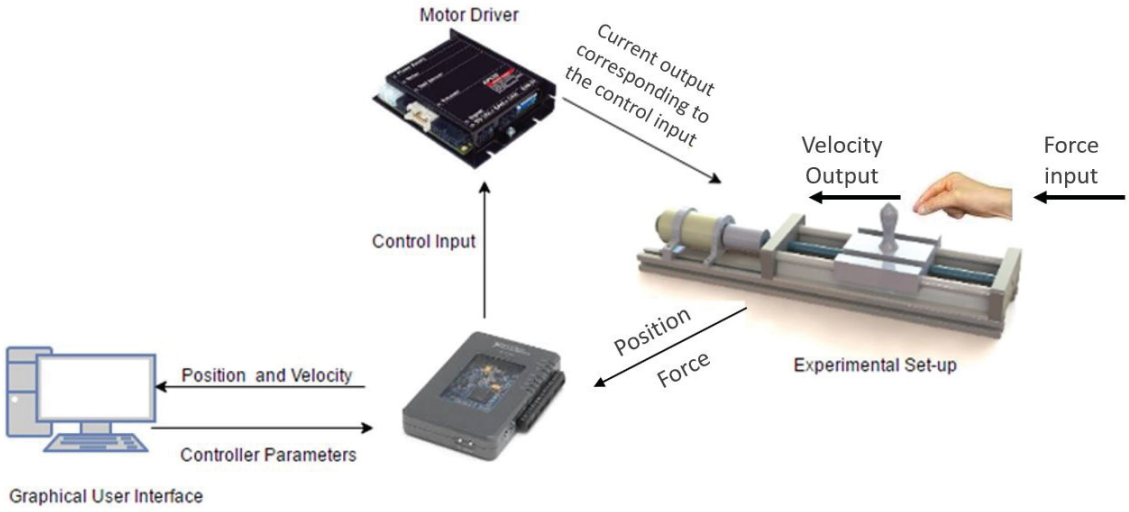

Figure 3.3. The information flow between the components

The information flow between these components is presented in Figure 3.3. The controller parameters such as controller gains and admittance terms can be defined via the graphical user interface (GUI), then the process starts by receiving the measured applied force and the position data in the DAQ. The designed admittance control algorithm generates the control input in the micro-controller which sends this information to the motor driver. The motor driver (servo amplifier) then calculates the respective current output for the received control input and drives the DC motor. The output velocity and the position can be monitored in real-time via using GUI.

3.1.1. Dynamic Model of the System

In order to design a controller, it is required to develop a mathematical model of the system. In Figure 3.4, the free body diagram of the experimental set-up is given. In this figure, F_{ij} represents the applied force by the i^{th} component to the j^{th} component. The F_{ext} is the external force which is the applied force by the human. T, m, a, b and v represent the actuator torque, mass of the moving platform, acceleration of the moving platform, viscous friction coefficient and the velocity of the moving platform, respectively. In Equation 3.1, the relation between the torque supplied by the actuator $T(t)$ and the armature current $i(t)$ is given where the k_t is the torque constant of the actuator.

$$T = k_t i(t) \tag{3.1}$$

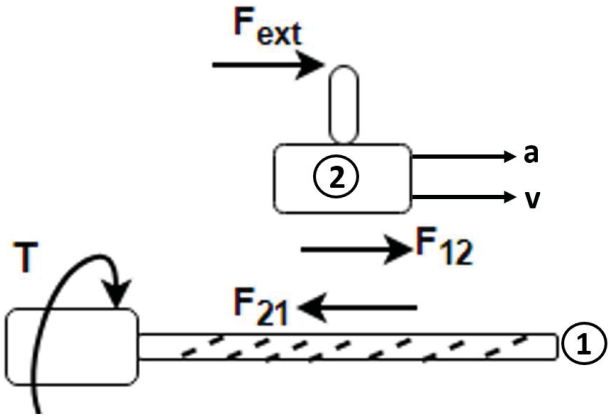

Figure 3.4. Dynamic model of the experimental set-up

Equation 3.2, defines the relationship between the angular position, $\theta(t)$, and the linear position $x(t)$ which also defines the relation between task space and the joint space. By taking the derivative of this equation, the velocity relation can be obtained. In these equations, k_g is the pitch of the lead screw where its value is $k_g = \frac{5}{2\pi}$ in $\frac{mm}{rad}$.

$$x(t) = k_g\theta(t) \longrightarrow \dot{x}(t) = k_g\dot{\theta}(t) \tag{3.2}$$

The force and torque relation can be defined in Equation 3.3.

$$\begin{aligned} &\tau - \tau_{\text{friction}} = k_g F_{21} \\ &\tau = k_g F_{\text{drive}} \\ &\tau_{\text{friction}} = k_g F_{\text{friction}} \\ &F_{\text{friction}} = bv + \text{sgn}(v)\mu N \\ &F_{21} = -F_{12} \end{aligned} \tag{3.3}$$

The dynamic equation can be obtained for the 2nd component as in Equation 3.4 and the Equation 3.3 can substitute into this equation.

$$\begin{aligned} &-F_{\text{ext}} + m\ddot{x}(t) = -F_{12} = F_{\text{drive}} - b\dot{x}(t) - \text{sgn}(v)\mu N \\ &-F_{\text{ext}} + m\ddot{x}(t) + b\dot{x}(t) + \text{sgn}(v)\mu N = F_{\text{drive}} = \frac{\tau}{k_g} \end{aligned} \tag{3.4}$$

Since the admittance controller will be dealing with the external force to cancel its affect, this term can be neglected in order to obtain simplicity reasons and the nonlinear term $\text{sgn}(v)\mu N$ can be taken out to linearize the system.

Hence, the linearized dynamic equation is simplified as in Equation 3.5.

$$\frac{k_t i(t)}{k_g} = m\ddot{x}(t) + b\dot{x}(t) \tag{3.5}$$

By taking the Laplace transformation of the Equation 3.5, the transfer function between the velocity and the current can be defined as following Equation 3.6.

$$\frac{V(s)}{I(s)} = \frac{k_t/k_g}{ms + b} \tag{3.6}$$

3.1.2. Parameter Estimation

Parameters of k_t, m, and b the system needs to be estimated to design controller. In order to estimate the torque constant k_t the experimental setup which is shown in Figure 3.5 is designed.

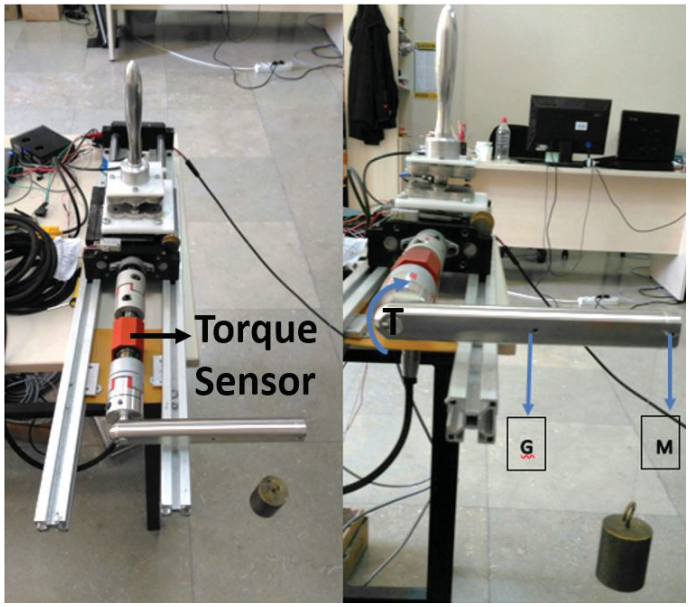

Figure 3.5. Torque sensor calibration verification experimental set-up

In this experiment, a rotary torque sensor (Futek TRS300) is attached to the lead screw and the linear motion is constrained. Next, predefined moments are applied to the system by using moment arm and calibrated weights. The data acquisition from the torque sensor is realized by using MyRIO DAQ and LabView software. In Figure 3.5, G represents the weight of the moment arm which is 6.867 N and is designed$M$ represents

the external force that is applied to the system. The applied torque T_a is calculated by using Equation 3.7 where the length of the moment arm L is 180 mm .

$$T_a = ML + G\frac{L}{2} \tag{3.7}$$

Table 3.1. The results of Futek TRS300 torque sensor measurement

G [N]	M [N]	Ta [Nm]	Tm [Nm]	Error %
6,867	0	0,618	0,6	0,029
6,867	0,981	0,800	0,8	0,001
6,867	1,962	0,982	1	0,017
6,867	2,158	1,019	1,02	0,0005
6,867	4,905	1,53	1,58	0,032

Table 3.1 presents the results of the torque sensor measurements. As it can be observed from the results, torque measurements are in acceptable error ranges. In order to determine the torque constant, the DC motor is mounted to the torque sensor and the linear motion is constrained. By using the DAQ and the motor driver, 10 control inputs are applied to the motor. The resultant actuator torque is measured and presented in Figure 3.6 which shows almost a linear relationship. By using linear regression, the equation of the output torque in terms of applied current is calculated as $T(i) = 0.078i + 0.005$ therefore, torque constant could be calculated as $k_t = 0.078\frac{Nm}{A}$.

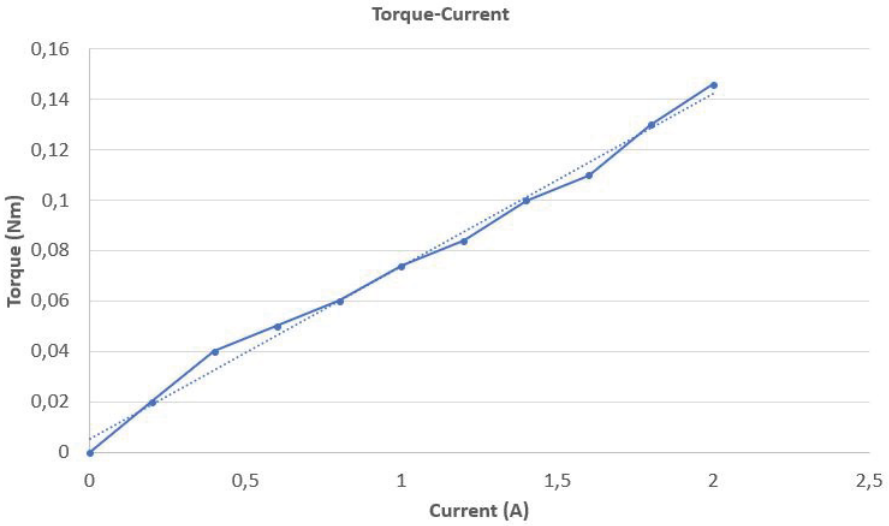

Figure 3.6. The measured torque values respect to the applied current

Parameters of the transfer function, which is given in Equation 3.6, can be estimated by using frequency response analysis. In order to realize this, several sinusoidal inputs with constant current amplitudes are given to the system with a frequency range from $0.5\frac{rad}{s}$ to $100\frac{rad}{s}$.

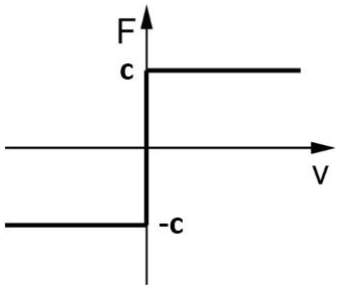

Figure 3.7. Coulomb friction model

In this experimental set-up, dry friction has a considerable effect. In order to eliminate this nonlinear effect, the dry friction can simply be modeled as Coulomb friction which is shown in Figure 3.7, and the governing equation is given in Equation 3.8 where c represents dry friction force and $V(t)$ represents the linear velocity. For the estimation of the dry friction coefficient, the applied current is increased until the motion is started and the friction coefficient is estimated as $0.274N$.

$$F_c = c\text{sgn}(V(t)) \tag{3.8}$$

In order to realize frequency response analysis, friction model is added to the input as a feedforward component then the output velocity is measured for different frequencies. Figure 3.8 shows the obtained Bode plot of the system.

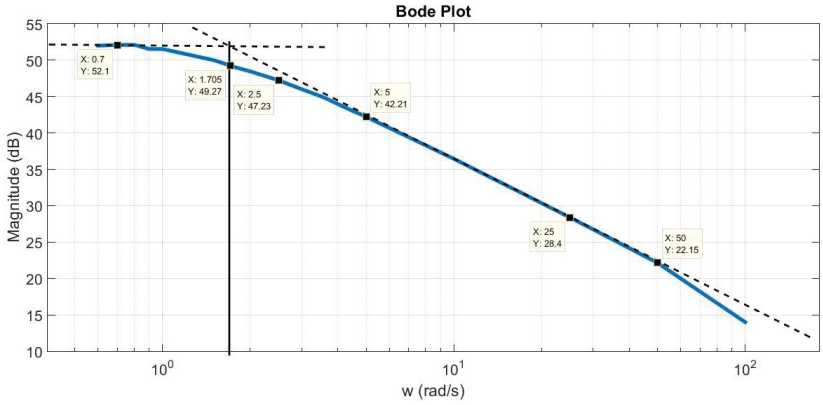

Figure 3.8. Frequency response analysis of the experimental set-up

Since the transfer function of the system is modeled as a first order system, the Bode plot is also expected to be first order. By investigating of the Bode plot, m and b parameters are calculated. Transfer function in Equation 3.6 is reorganized for parameter estimation as shown in Equation 3.9 where the parameters are obtained as $\frac{1}{\tau} = 1.7\frac{rad}{s}$ and open-loop gain K $20log(K) = 52dB$ from the Bode plot.

$$\frac{V(s)}{I(s)} = \frac{\frac{k_t}{k_g b}}{\frac{m}{b}s + 1} = \frac{K}{\tau s + 1} \tag{3.9}$$

Using these numerical results, transfer function of the system is estimated as

$$\frac{V(s)}{I(s)} = \frac{9.9317}{0.0146s + 0.0249} \ . \tag{3.10}$$

The model validation is realized by applying sinusoidal input withs magnitude of $0.6A$ and a frequency of $3rad/sec$. Figure 3.9 shows the comparison of the system output and the model output to the same sinusoidal input.

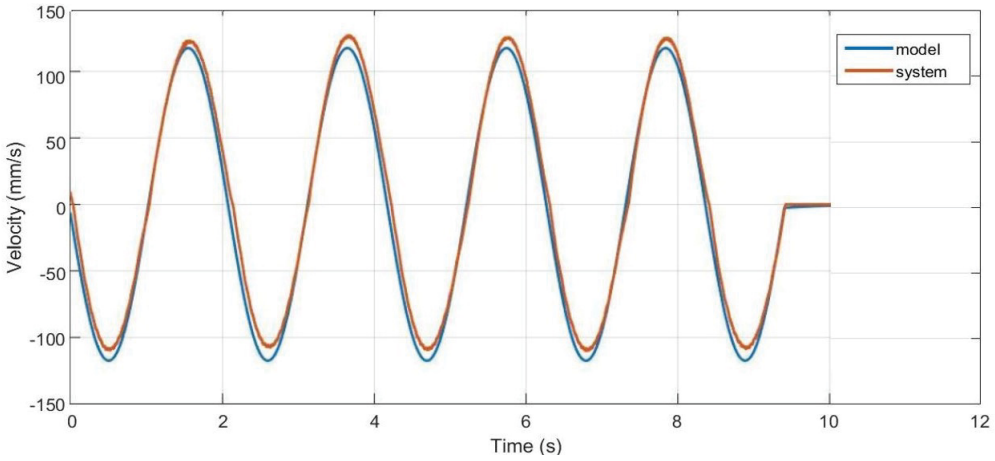

Figure 3.9. Model verification for the experimental set-up

3.1.3. Admittance Controller Design

In order to investigate the effects of the admittance term on back-drivability, an admittance controller is designed. The block diagram representation of the controller is given in Figure 3.10 where the G_c represents the low-level velocity controller. F_{ref} is the reference force which is selected to be zero for free motion (full back-drivability), A is the

admittance term, X_m is the measured position, X_e is the position vector of the contacted environment, K_E is the stiffness between the handle and the human hand, V_s and F_s are velocity and force sensor transfer functions, respectively.

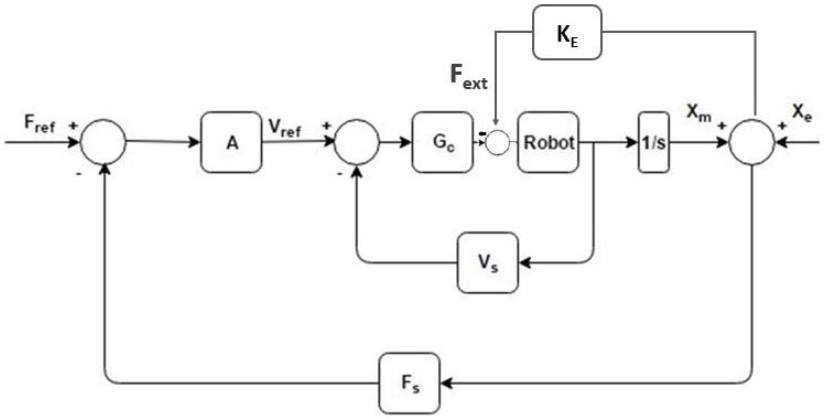

Figure 3.10. Control scheme of one dof admittance type device
(Source: Işıtman et al., 2017)

In this scheme, a velocity controller is implemented as a low-level controller. Since the model of the system is obtained in the previous section, the feedback linearization method is applied to eliminate the non-linear effects.

Velocity error e is defined as in following equation.

$$e = \dot{x}_{ref} - \dot{x} \tag{3.11}$$

If the error satisfies the following differential equation;

$$\begin{aligned} \dot{e} + ke &= 0 \\ \ddot{x} &= \ddot{x}_{ref} + ke \end{aligned} \tag{3.12}$$

which is obtained when the the error converges to zero exponentially.

Substituting Equation 3.12 to the equation of motion results in following equation and the corresponding block diagram of the feedback linearization based admittance controller is presented in Figure 3.11.

$$F = m(\ddot{x}_{\text{ref}} + ke) + b\dot{x} + c\text{sgn}(\dot{x}) - F_{\text{ext}} \tag{3.13}$$

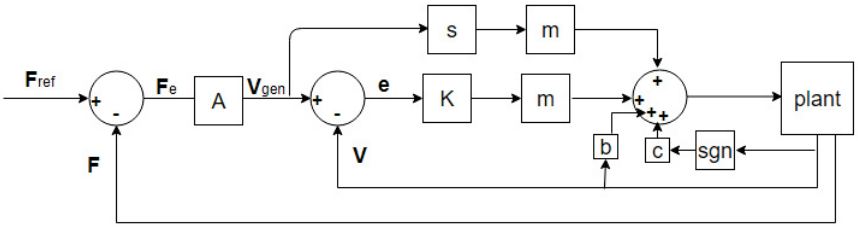

Figure 3.11. Admittance controller with feedback linearization

In an admittance controller, a force set point is specified and it is tracked by a force compensator. This compensator can be modeled as a mass, spring and damper system, given in Equation 3.14; where F, V, m_a, b_a, k_a and A parameters refer to force, velocity, mass, damper, spring and admittance term, respectively.

$$\begin{aligned} F(s) &= m_a s V(s) + b_a V(s) + \frac{1}{s} k_a V(s) \\ \frac{V(s)}{F(s)} &= \frac{s}{m_a s^2 + b_a s + k_a} = A \end{aligned} \tag{3.14}$$

An admittance control requires accurate trajectory following capabilities and accurate measurements of the interaction forces between the robot and its environment. These requirements put specific demands on the system design such as high power actuators and a stiff construction. On the other hand, characteristics of the admittance term depend on the chosen parameters which are selected by considering tracking capability of the experimental set-up and the human force limits.

High admittance term causes a sudden reaction, while compliance with a smaller admittance term gives a slow reaction to the applied force. Mass and damper coefficients are chosen as small as possible to initiate the robot motion softly. However, selecting very small values cause the system to be very sensitive to the interaction forces.

3.2. Description of the Task

Effects of the admittance term parameters on the performance of human operators are investigated by designing an experiment. Accuracy and energy usage of the subjects with different parameters are evaluated by having the users perform a specific designed task.

In this task, the subject is asked to hold the precision type handle, with his/her dominant hand. As guided by the graphical user interface, which is given in Figure 3.12, the subject is instructed to move the handle to the blue target and keep it there for four seconds as indicated by the user interface. After four seconds, the subject moves the handle by 116 mm to reach the red target and holds the handle at that location for four seconds. The subject repeats this process 2 times without releasing the handle. When the user reaches the target for the last time, she/he releases the handle without any further action.

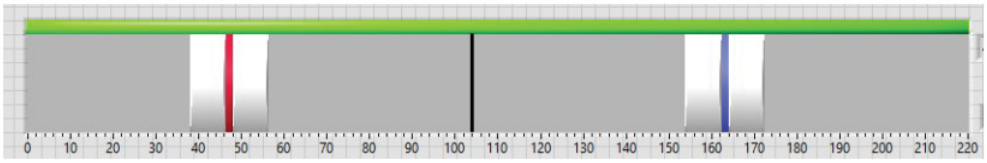

Figure 3.12. Graphical user interface for the generated task
(Source: Işıtman et al., 2017)

The black bar demonstrates handle's position and targets are represented as a red (on the left) and blue (on the right) bars. The white region near the targets presents the scoreboard which is created to define a metric for comparison between the parameters. The scoreboard is given in Figure 3.13. In this figure, the x-axis represents the position range of the targets. The 46-48 mm and 162-164 mm ranges are the main targets which are defined as 100 points. As the position of the handle moves away from this are the score starts to decrease with respect to the defined scale. The overall score is calculated by taking the average score at the waiting phase of the experiment. During all the experiments, locations of the targets are kept the same.

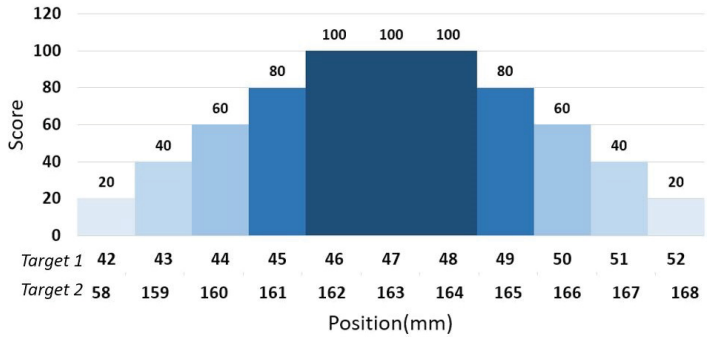

Figure 3.13. Score range of the first target based on position
(Source: Işıtman et al., 2017)

Efforts of the subjects while moving the handle is investigated and named as energy consumption. The evaluation of these efforts is realized by using Equation 3.15 where F_n, x_n, $E_{kin,n}$, $E_{damp,n}$, $E_{spr,n}$, $E_{lost,n}$ represent applied force, position of the handle, kinetic energy, dissipated energy due to virtual damper, potential energy stored in the virtual spring and energy lost due to viscous friction, respectively. The subscript n represents the step number of the data acquisition.

$$\begin{aligned}
F_1(x_1 - x_0) &= E_{kin1} + E_{damp,1} + E_{spr,1} + E_{lost,1} \\
E_{spr,1} + F_2(x_2 - x_1) &= E_{kin,2} + E_{damp,2} + E_{spr,2} + E_{lost,2} \\
&\vdots \\
F_n(x_n - x_{n-1}) &= E_{kin,n+1} + E_{damp,n+1} + E_{spr,n+1} + E_{lost,n+1} \\
E_{spr,n} &= E_{kin,n+1} + E_{damp,n+1} + E_{lost,n+1} \\
\hline
\sum_{i=1}^{n}(F_n \Delta x_n) &= \sum E_{kin} + \sum E_{damp} + \sum E_{lost}
\end{aligned} \tag{3.15}$$

The work is calculated by multiplying the applied force at a step with the measured position difference with the previous step. In a similar way, the dissipated energy due to virtual damper and the kinetic energy are calculated as

$$\begin{aligned}
E_{damp,n} &= bV_{n-1}(x_n - x_{n-1}) \\
E_{kin,n} &= \frac{1}{2}m(V_n - V_{n-1})^2
\end{aligned} \tag{3.16}$$

The energy loss of the system can be neglected since the results will be evaluated relatively. Since the experimental process is completed when the handle comes back to its static condition again, the sum of the kinetic energy terms is equal to zero.

As it can be observed from the Equation 3.15, the potential energy of the spring term cancels out between each state. Due to these conditions, damping term dissipates all the energy in the experiments.

3.3. Experimental Results

The experiments are carried out with 4 women and 9 men subjects whose ages are between 24 and 32. Before the experiments, each subject is informed about the task. They are allowed to practice with different admittance parameters than the inspected ones in order not to affect the reliability of the comparison-based results.

The experiments can be grouped into two main categories which consist of three different experiments. The first category of the experiments consist of the mass-spring-damper model and the second group is modeled with mass and damper terms but without a spring term. In these 6 experiments, the effect of the corner frequency is investigated. Table 3.2 presents chosen admittance parameters and the designated corner frequency respect to the experiment number.

Table 3.2. Mass-spring-damper parameters
(Source: Işıtman et al., 2017)

Admittance Term Parameters				
Experiment Number	(m) Mass (kg)	(k) Spring (N/m)	(b) Damping (Ns/m)	(ω_n) Corner Frequency (rad/s)
1	2	2	3,78	1
2	2	18	11,38	3
3	2	72	22,77	6
4	2	0	2	1
5	2	0	6	3
6	2	0	12	6

Damping ratio ζ of the admittance term $\frac{K\omega_n^2 s}{s^2+2\zeta\omega_n s+\omega_n^2}$ is kept constant to determine parameters with respective to desired natural frequency. In this thesis, the bandwidth frequency is named as corner frequency for both first order $\omega_c = \frac{b}{m}$ and second order $\omega_c = \sqrt{\frac{k}{m}}$ admittance gains.

For the first three experiments, desired corner frequencies are obtained by modifying the spring parameters while the damping parameter is adjusted for the last three experiments.

The effect of the spring term is investigated by comparing the test results with the same corner frequency which are the experiments 1-4, 2-5 and 3-6. The main reason to do so is to have similar bandwidths for two types of admittance terms; with and without the spring component.

The result of the accuracy experiments is given in Table 3.3 with the average and the normalized average values of each set of experiments. As it can be observed from the results, when the corner frequency is increased, obtained accuracy scores also increase. Also, better accuracy is obtained with spring term for the same corner frequency results.

Table 3.3. Accuracy Scores of Subjects
(Source: Işıtman et al., 2017)

Accuracy Results						
Subject	*Exp # 1*	*Exp # 2*	*Exp # 3*	*Exp # 4*	*Exp # 5*	*Exp # 6*
1	77,28	76,8	91,23	66,67	86,85	85,47
2	88,72	93,21	90,46	71,42	78,63	90,27
3	89,75	89,02	90,32	55,91	72,67	68,25
4	92,22	93,03	94,92	68,04	79,71	80,15
5	84,51	81,59	92,85	82,36	79,41	84,41
6	80,21	87,49	90,86	67,34	84,57	87,78
7	71,59	84,43	85,9	69,6	84,68	85,47
8	61,14	88,94	90,08	51,56	82,1	74,7
9	47,03	77,82	78,19	67,5	74,71	83,84
10	62,79	89,85	85,48	58,78	69,31	75,84
11	68,25	75,32	73,98	57,78	81,69	76,58
12	72,6	90,4	90,08	67,04	76,31	84,22
13	88,3	91,25	82,74	70,31	84,03	90,81
Average	75,72	86,09	87,47	65,71	79,59	82,14

The energy consumption, which indicates the effort by the user, in each experiment is presented in Table 3.4 and the units for these results are given in Joules. Similar to the accuracy experiment results, the supplied energy by the user increases as the chosen corner frequency values are increased. The first three experiment group which includes spring term, consumes more energy with respect to the latter one.

Table 3.4. Energy Consumption of Subjects
(Source: Işıtman et al., 2017)

Energy Consumption (*J*)						
Subject	*Exp # 1*	*Exp # 2*	*Exp # 3*	*Exp # 4*	*Exp # 5*	*Exp # 6*
1	0,12	0,34	0,5	0,05	0,1	0,21
2	0,06	0,16	0,34	0,04	0,11	0,23
3	0,05	0,17	0,37	0,05	0,2	0,17
4	0,07	0,2	0,43	0,04	0,09	0,14
5	0,13	0,28	0,5	0,05	0,12	0,2
6	0,07	0,28	0,55	0,05	0,09	0,16
7	0,07	0,18	0,4	0,06	0,1	0,28
8	0,06	0,16	0,32	0,04	0,08	0,15
9	0,09	0,21	0,47	0,03	0,06	0,11
10	0,12	0,2	0,54	0,05	0,12	0,19
11	0,06	0,18	0,36	0,03	0,07	0,15
12	0,08	0,23	0,55	0,02	0,12	0,19
13	0,11	0,28	0,5	0,04	0,11	0,23
Average	*0,08*	*0,22*	*0,45*	*0,04*	*0,1*	*0,18*

3.4. Conclusions

In the robotic pituitary gland surgery, safety and control of the physical interaction between the endoscpoe and the human body is a vital part. In the event of an emergency, the surgeon might be required to back drive the robotic arm. If the type of transmission system does not allow passive back-drivability, then the back-drivability is satisfied by the use of an admittance controller.

In the surgical case, the aim is controlling the interaction of the surgeon with the robot by using the admittance controller. The interaction dynamics is defined by the admittance term and the determination of this term is not trivial. The optimal parameters depend not only on the key performance criteria but also on the human operator. An experimental study is carried out to evaluate the effects of the admittance term parameters on the performance of human operators in terms of the energy efficiency and the accuracy.

To realize this experiment, a non back-drivable one degree of freedom experimental set-up is designed. Then, feedback linearization based admittance controller is applied by estimating the model parameters of the system.

The user experiment results are evaluated in terms of accuracy and energy consumption according to the described task which is presented in previous sections. The results are investigated in two main perspectives. In the first one, the effects of the spring term are investigated by comparing accuracy and energy consumption results for the same corner frequencies. In the second perspective, the effect of the corner frequency is investigated by comparing the results in similar type of admittance term.

It is observed that the corner frequency is one of the essential parameters for better accuracy for both types of admittance terms with and without the spring component. On the other hand, spring term has a positive influence on the accuracy which can be observed by the comparing the experiment groups 1-4, 2-5, 3-6, which have same corner frequencies.

As presented in Equation 3.15, the energy calculations depend on damping term and system velocity. In addition to that, the mass term is kept constant in all the experimental groups. Hence, the energy consumption increases as a result of higher corner frequency which is consistent with the obtained results.

As a conclusion, the mass, spring, damper parameters can be chosen optimally for specific tasks. For the tasks that require accuracy, the higher spring coefficient in the admittance term must be preferred such as in surgical robots. However, increasing the coefficients of admittance term requires higher force values and it is limited with the

operating limitations of the user. On the other hand, due to high-energy consumption, the spring term might be unnecessary for rehabilitation tasks which is another medical robotic application.

CHAPTER 4

VISCOELASTIC MODELING OF HUMAN NASAL TISSUES

The work presented in this Chapter is conducted to model the interaction of the endoscope with the nasal tissues to be used in the control and simulation tests of an endoscopic pituitary tumor robotic surgery system. In the NeuRoboScope project, an endoscope is handled by the robot which rotates about a remote center of motion (RCM). This point is commonly called the pivot point. During the surgery, it is expected that the endoscope interacts with the nose tip and the nasal concha.

In the next Section, experimental set-up is presented with validation of this measurement system. Then test procedures are defined to acquire measurements from a fresh frozen human cadaver. In the third Section of this Chapter, parameter estimation technique is explained and in the final section, results are presented.

4.1. Experimental Set-up

Preparing in-vitro specimen for endoscopic pituitary tumor surgery area is not straightforward, hence, a new mobile hand-held measurement device is designed (Işıtman et al., 2018). This new design gives an opportunity to acquire the necessary data in an ex-vivo set-up without disrupting the characteristic motion of the surgery. The soft tissue is designated to be modeled by using applied moment and angular displacement about a pivot point since the endoscope will be controlled to perform rotations about a pivot during the surgery.

In order to acquire force and torque measurements, an ATI MINI45 (ATI Industrial Automation) force/torque (F/T) sensor is used and specifications are given in Table 4.1.

Table 4.1. ATI MINI45 Specifications
(Source: ATI, 2018)

Sensing Ranges				**Resolution**			
F_x, F_y	F_z	T_x, T_y	T_z	F_x, F_y	F_z	T_x, T_y	T_z
580 N	1160 N	20 Nm	20Nm	1/4 N	1/4 N	1/188 Nm	1/376 Nm

For the angular displacement measurements, BNO055 (BOSCH Sensortech) inertial measurement unit (IMU) sensor is used which is a 9-axis absolute orientation sensor with an integrated sensor fusion algorithm. The sensor consists of a 14-bit accelerometer, a 16-bit gyroscope with $\pm\frac{2000^\circ}{sec}$ sensing range and a triaxial geomagnetic sensor.

A KARL STORZ telescope (28731 BWA Hopkins) is used, in order to simulate the telescope of the endoscopic pituitary tumor surgery. A 3D printed holder is designed to imitate the real endoscope grasping. A computer-aided drawing of the designed mobile experimental device is given in Figure 4.1.

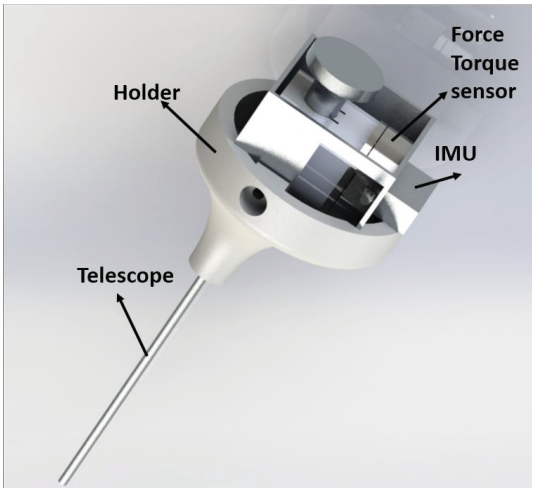

Figure 4.1. CAD model of the designed measurement device

The calibration of the F/T sensor is tested is carried out applying calibrated force and moments. The realization of the test is presented in Figure 4.2 and the results is given in Table 4.2. The test set-up is placed parallel to the ground by using IMU sensor. As the results show force measurement errors are below 4% and the moment measurement error is not more than 1.5%. These ranges of errors are evaluated to be acceptable for this study.

Table 4.2. ATI Mini45 Calibration Validation

Force and Moment Measurement Validation							
Distance (m)	**Mass (kg)**	**Measured Force (N)**	**Applied Force (N)**	**Force Error (%)**	**Measured Moment (Nm)**	**Applied Moment (Nm)**	**Moment Error (%)**
0,075	0,02	0,190	0,196	3,058	0,0145	0,0147	1,461
0,075	0,05	0,480	0,490	2,079	0,0363	0,0367	1,325
0,075	0,1	1,02	0,981	3,975	0,0729	0,073	0,917
0,075	0,2	2,01	1,962	2,446	0,1459	0,147	0,849
0,075	0,5	4,901	4,905	0,081	0,363	0,367	1,189

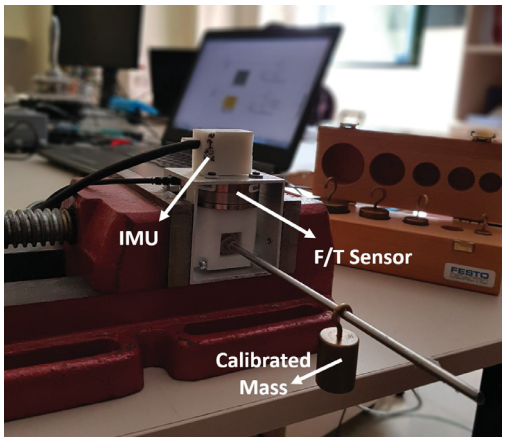

Figure 4.2. ATI Mini45 Calibration Validation Test Set-up

4.2. Proof of Concept Test for the Use of the New Measurement Device

Before realizing the human cadaver soft tissue measurements, proof of the measurement concept is tested in the laboratory by designing a robotic test set-up. The aim of the test is to prove the capability of measuring stiffness by acquiring moment and angular displacement data. In order to validate the IMU sensor measurement, an optical incremental encoder (AEDA 3300 AT) is mounted to a DC motor (Hitachi D06D401E).

The IMU angular displacement data is acquired by using an Arduino board and the data processing is realized in Matlab /Simulink environment at 100 Hz. The raw quaternion data is used to obtain transformation matrix then the angular displacement θ is determined by using following procedure.

At the begining of the validation experiment, tip direction vector $\vec{v}_1$ is defined as $\begin{bmatrix}1 & 0 & 0\end{bmatrix}^T$ and then $\vec{v}_2$ is calculated by using Equation 4.1 where $\hat{C}$ is the transformation matrix.

$$\vec{v}_2 = \hat{C}\vec{v}_1 \tag{4.1}$$

The angular rotation with respect to the $\vec{v}_1$ is calculated by using Equation 4.2.

$$\theta = cos^{-1}(\vec{v}_2 \times \vec{v}_1) \tag{4.2}$$

Figure 4.3 represents these vectors and the angular movement around the pivot point.

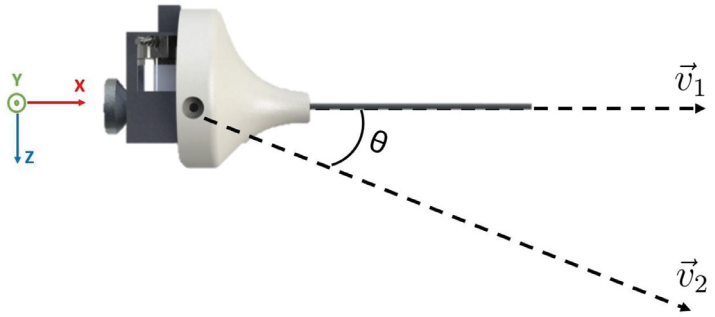

Figure 4.3. Angular displacement of the measurement device around the pivot point

The orientation of the device highly affects the moment measurements due to the weight of the force/torque sensor since the pivot point is never on the mass center. Gravity compensation algorithm is used to eliminate gravitational effects. The mass center is defined as the center of the upper surface of the F/T sensor and center of the gravity (CoG) of the device is $\begin{bmatrix} 5.44 & 0 & 19 \end{bmatrix}^T$ in mm. The weight (W) of the device that affects the gravitational force is $\begin{bmatrix} 0 & 0 & 1.57 \end{bmatrix}^T$ in N when the device is placed vertically. At the beginning of the gravity compensation procedure, the device must be held vertically then force sensor should be reset from the software of the force sensor. Then, the gravitational force and related moment can be calculated by using Equation 4.3 where F_c and M_c are the calculated force and calculated moment, respectively. In order to simplify the calculations, the axes of the IMU sensor and the axes of the F/T sensor is aligned in the assembly.

$$\begin{aligned} \vec{F}_C &= \hat{C}\vec{W} \\ \vec{M}_C &= C\tilde{o}G\vec{F}_C \end{aligned} \tag{4.3}$$

The external force and moment measurement can be obtained by subtracting the calculated f/t from the measured f/t data. This approach is valid for the static conditions since it also depends on inertial forces. In order to eliminate the inertial force effects, angular acceleration should be zero, in other words, the device should be rotated with constant angular velocity.

To actuate the system with a constant velocity in a specific angular displacement range, a PI velocity controller is designed and implemented in LabView environment. This controller is realized in 1 kHz by using myRIO (National Instruments) DAQ board. A tension spring is attached 75 mm away from the center of the motion and its stiffness is estimated by experiments. The proof of concept test set-up is given in Figure 4.4.

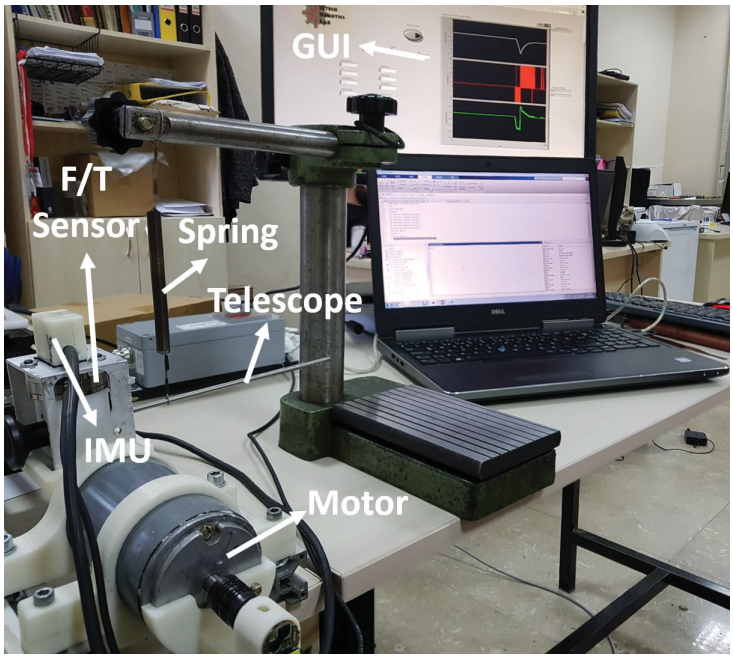

Figure 4.4. Proof of concept test set-up

The velocity reference input is generated by combining two step function. The step time of these functions determines the total angular displacement. One of the reference velocity input profiles is given in Figure 4.5 with the corresponding velocity and position measurements from the encoder.

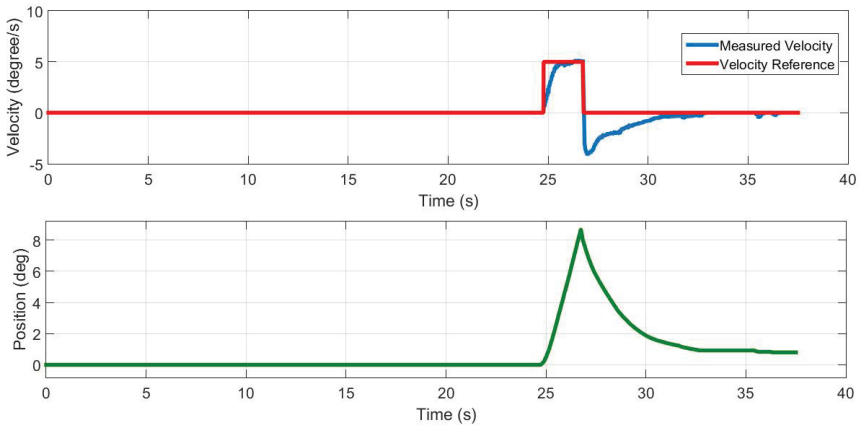

Figure 4.5. Velocity reference input with encoder measurements

In this figure, measured velocity, reference velocity, and measured position is represented. When the reference input reaches to the zero, controller is closed in order to protect to system from any undesired movements. As a result of that spring force is able

to move the device to its initial position. However, stiffness measurements are realized by considering the loading part of the experiments.

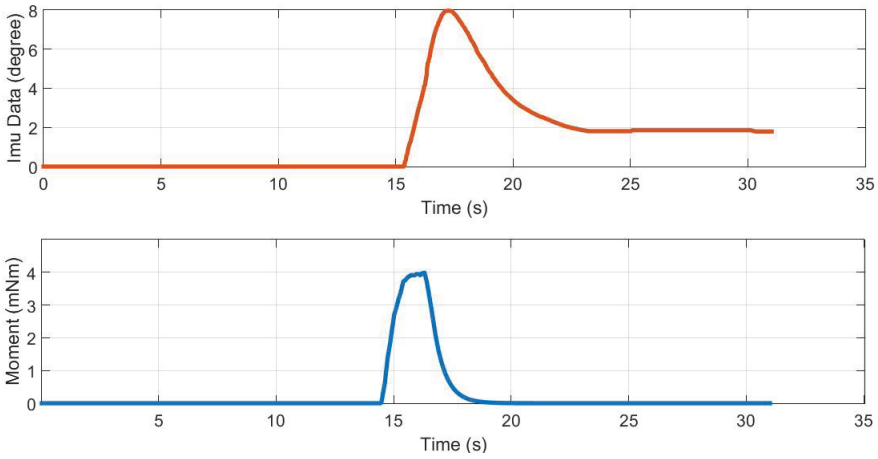

Figure 4.6. Force torque sensor and IMU measurements

Figure 4.6 shows the moment measurements from F/T sensor and angular displacement measurements from IMU. Table 4.3 presents the results of five stiffness measurements. One of the outcomes of these experiments is the IMU sensor provides quite similar data to the encoder data; hence, using IMU sensor for the soft tissue tests is acceptable. The results also show that the designed measurement device is capable to acquire repeatable stiffness measurements with the $2.14\ mNm$ standard deviation.

Table 4.3. Stiffness measurement results

Test No	Encoder ($\Delta\theta$) rad	IMU ($\Delta\theta$) rad	Moment (mNm)	Stiffness (mNm)	IMU Error %
1	0,15	0,14	10,89	77,23	5,74
2	0,14	0,14	10,46	75,25	3,06
3	0,12	0,12	8,59	72,18	4,03
4	0,13	0,12	8,73	72,68	4,98
5	0,12	0,12	8,57	72,81	2,08

4.3. Stiffness Test on Human Cadaver Tests

Soft tissue experiments are realized in an ex-vivo environment by using freshly frozen human cadaver's head. In the Neuroboscope project, the endoscope handled by the robot is expected to interact with two main parts of the nasal tissue which are the nose tip and the nasal concha hence, these tissues are investigated.

The experiments are conducted to define force/moment limits and model the soft tissue dynamic. In the following sections, these tests are presented along with their results.

For the experiments, human cadaver head is preprepared by following procedure:

- Freshly frozen cadaver head is started to be thawed 48 hours beforehand the tests are realized
- During the thawing process, thin section tomography images of the cadaver head are taken with the Siemens Somamtom Perspective device.
- When the tissue became closer to the live tissue strength, the cadaver head is then fixed with a three-point head clamp (Mayfield, Integra Life Sciences Co., NJ)

4.3.1. Force and Moment Limit Tests

Force and the moment limits are required in order to determine the maximum range of forces and moments applied by the surgeon during the surgery. Making use of the results of these experiment, proper actuators can be selected for the project.

The following test is designed to measure the force and moments about two axes that are applied to the tip of the nose and the schematic representation of the test is given in Figure 4.7. In this test, the surgeon is asked to hold the device similar to the endoscope and apply the maximum force that can be applied during the surgery to the tip of the nose in order to mimic the regular surgery procedure.

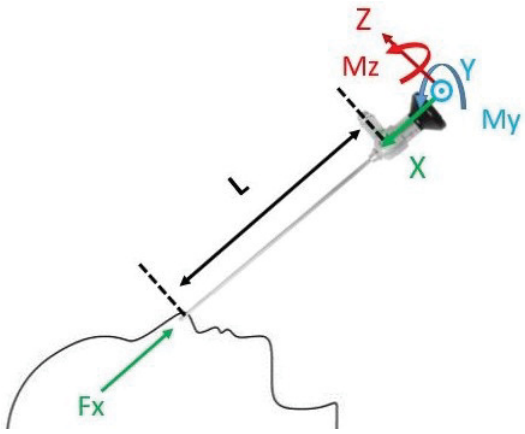

Figure 4.7. Nose tip force and moment limits test scheme

Figure 4.8 shows the five repetitions of the force measurements acquired the tip of the nose. In the first 50 seconds, the system is calibrated which is necessary for the gravity compensation algorithm. After that, the surgeon applies force to the tip of the nose according to his experiences then waits for some time then, releases the applied force. This process is repeated five times for this test.

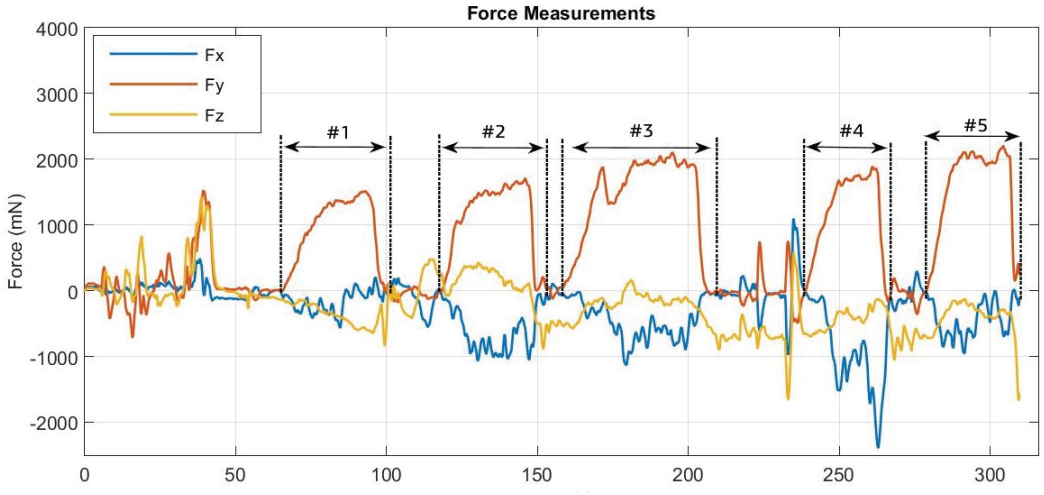

Figure 4.8. Force measurements of the tip of the nose

The result of test described above is given in Table 4.4. As it can be observed from the results, maximum force values are measured in trial # 3 and # 5. The corresponding moments are also presented in the table. As a result, the expected maximum values are determined as $\approx 2N$ and $\approx 0.3Nm$ for the force F_y and moment M_z applied at tip of the nose. These values are used in the dynamic analysis as required maximum moment and force to be applied in order to determine the required actuator torque by applying a safety factor. The dynamic analysis of the system is beyond the scope of this thesis.

Table 4.4. The measured force and moment data from the tip of the nose

Test	Fx (mN)	Fy (mN)	Fz (mN)	Mx (mNm)	My (mNm)	Mz (mNm)
# 1	-158,1	1390,5	-472,7	-22,9	40,6	227,4
# 2	-824,4	1534,4	211,0	-27,6	-136,6	280,7
# 3	-633,8	**1958,3**	-135,4	-33,0	-100,0	**345,6**
# 4	1179,6	1718,6	-363,5	-29,8	-82,9	310,6
# 5	-456,3	**2033,9**	-292,9	-33,3	-86,8	**353,8**

In order to measure friction force during to axial movement of the endoscope, another test is carried out by the surgeon. In this test, the surgeon is asked to apply force

to the tip of the nose as the normal force applied to the surface then, move the endoscope axially inside the nasal cavity and then, wait for a small amount of a time before pulling it back.

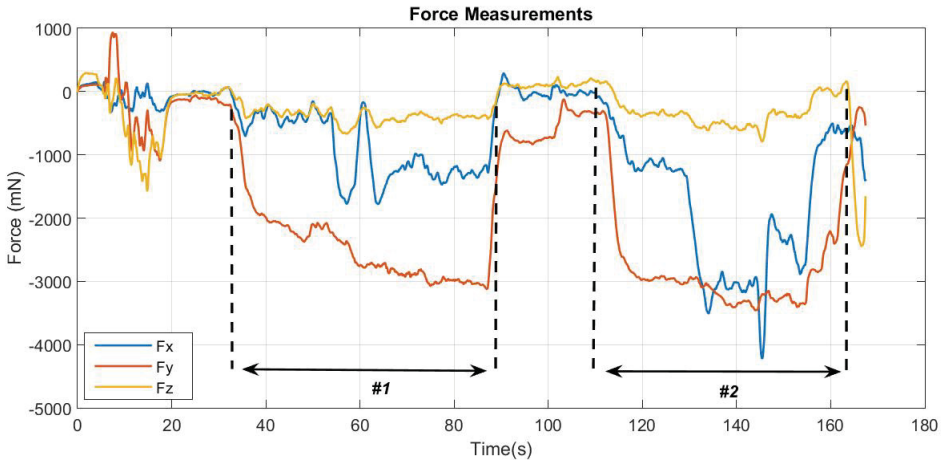

Figure 4.9. The frictional force measurements from the tip of the nose

The aforementioned procedure can be observed in the second attempt in Figure 4.9. The axial force, F_x, is increased while the contact to the tip of the nose remains then, after a while, axial force is decreased. This test is realized by two surgeons and the results in given Table 4.5. The maximum axial force due to the friction is highlighted with bold fonts. This force occurs when the endoscope enter to the nasal cavity when the endoscope in contact with the pivot point.

Table 4.5. The results of friction force measurements

Surgeon	Test	Fx (mN)	Fy (mN)	Fz (mN)	Mx (mNm)	My (mNm)	Mz (mNm)
1	#1	-901,2	435,0	1303,1	-5,3	-269,1	69,4
	#2	-2186,3	616,7	-63,5	-5,1	-137,9	63,0
	#3	**-2525,8**	859,5	-2407,7	3,2	249,3	98,2
2	#1	**-3213,6**	-3273,7	-569,3	55,5	72,3	-594,8
	#2	-1566,3	399,5	682,4	-1,1	-108,8	56,8
	#3	-2318,1	-377,3	-1577,3	28,9	276,5	-100,9

The third test is realized in the nasal cavity of the human cadaver instead of the tip of the nose. In this experiment, the surgeon is asked to apply force to the nasal concha without contacting the tip of the nose.

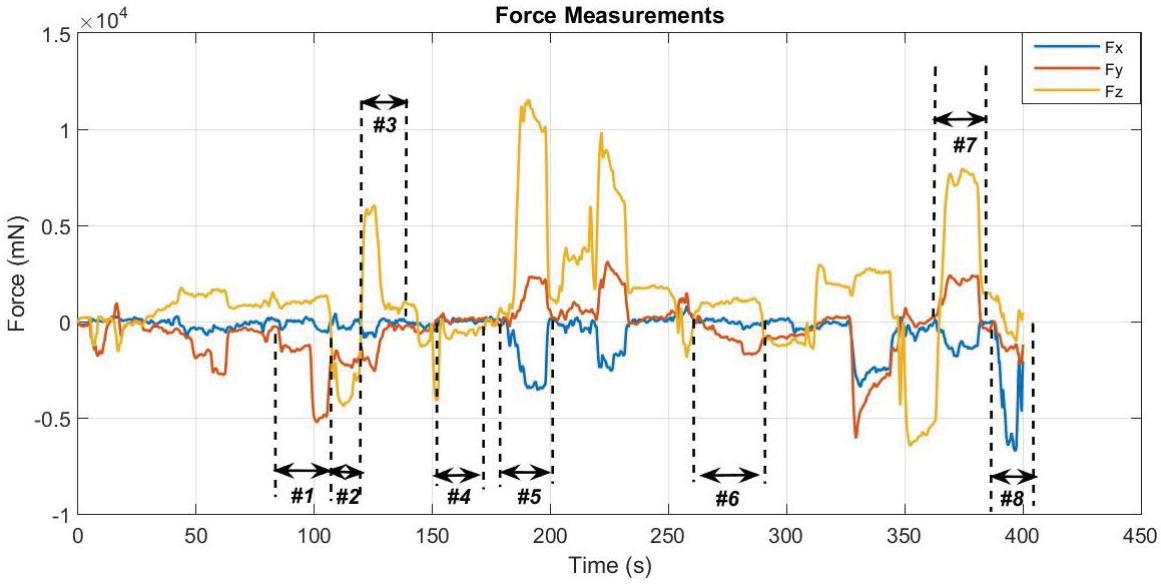

Figure 4.10. Force measurements of the nasal concha

In Figure 4.10 eight repetitions of the test is presented. In these measurements, force is applied in different axes on a nasal concha. The obtained results are given in Table 4.6.

Table 4.6. Nasal concha tissue force and moment measurements

Test	Fx (mN)	Fy (mN)	Fz (mN)	Fr (mN)	Mx (mNm)	My (mNm)	Mz (mNm)
#1	-403,9	-5063,5	1274,6	5237,1	90,3	-131,4	-769,3
#2	-338,9	-2237,5	-4184,1	4756,9	63,4	872,9	-489,4
#3	-685,0	2214,7	5841,9	6285,1	34,1	-907,9	-287,8
#4	20,3	93,3	-546,7	554,9	-6,2	170,7	17,8
#5	-3125,1	1771,6	11175,0	11738,2	-55,7	-1983,1	386,9
#6	70,3	125,6	1770,9	1776,7	3,841	-286,7	14,2
#7	-1382,4	2202,0	7494,8	7932,9	-46,0	-1229,0	369,4
#8	-6220,0	1365,4	-670,3	6403,3	32,194	-130,4	-230,7

During the data acquisition process, surgeons define the applied forces as regular, maximum acceptable and excessive regarding their experiences with real surgery conditions. This evaluation is given in following.

- # 1 and #2 are a maximum but acceptable forces.
- # 3 and 7 can be defined as a normal force however they do not occur often.
- # 4 and # 6 are in a regular force range.

- # 5 is an excessive force that should not be applied by the endoscope.
- # 8 should be considered as a maximum axial force for the nasal concha.

4.3.2. Soft Tissue Modeling Tests

Soft tissue modeling tests are realized both for nasal concha and the tip of the nose. These experiments differ from the previous ones by the motion of the endoscope.

4.3.2.1. Tip of The Nose Modeling Tests

In these experiments, the surgeons are asked to hold the device similar to the endoscope and perform the rotational movement around the predefined pivot point and compress the tip of the nose with a constant velocity. The pivot point is specified outside of the body which is presented in Figure 4.11.

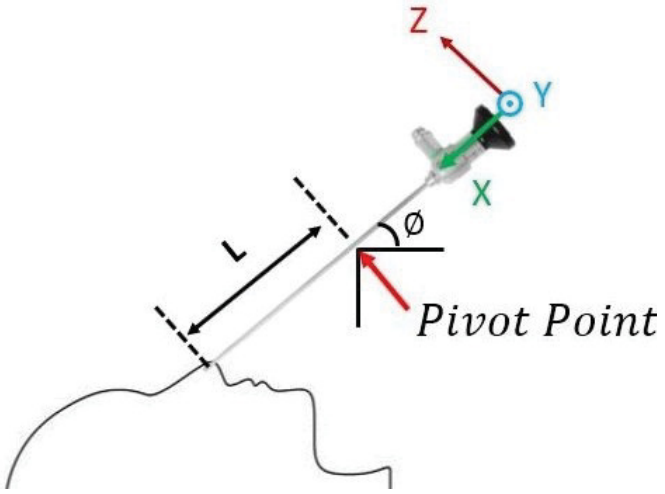

Figure 4.11. The schematic representation of the tip of the nose modeling test

In Figure 4.12, one of the moment and the angular displacement measurements are presented. The measurements are realized by four different surgeons and the measurement procedure compounds of three stages which are loading, stable and unloading. In the parameter estimation process, the first two parts are considered due to reliability of the data.

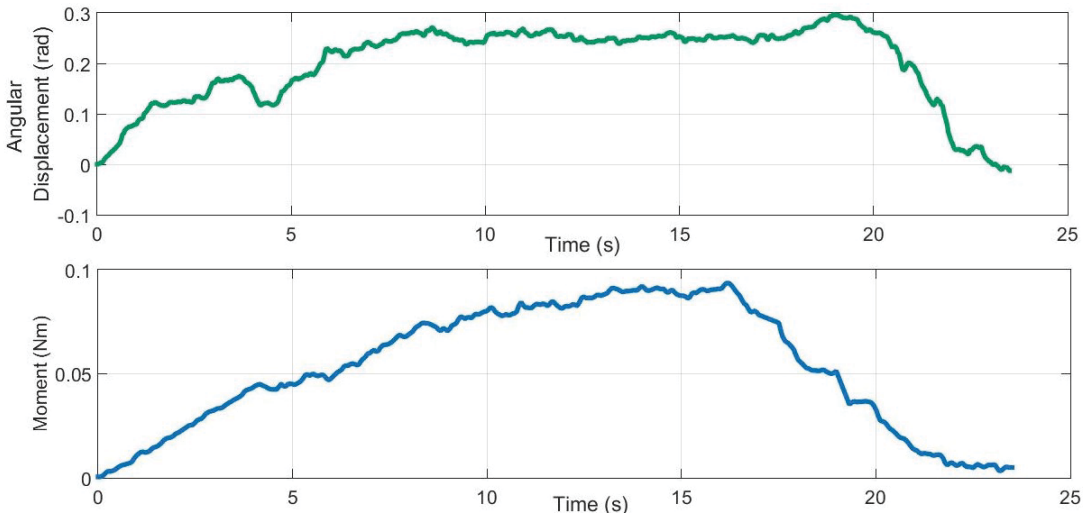

Figure 4.12. Moment and angular displacement measurements from the tip of the nose

In these experiments five different viscoelastic models are considered; Elastic, Kelvin Voight, Kelvin-Boltzmann, Maxwell and, Hunt-Crossley. The corresponding dynamic equations are given in Chapter 2 through Equation 2.3 to 2.7. For these equations, the parameter estimation process is realized as following steps :

1. Each interaction model is developed in Matlab/Simulink environment

The model is developed by using angular position data and the resultant moment is compared with the measured moment data to obtain the error in the model.

In Figure 4.13, the block diagram of an elastic model is given where the tau is selected as 0.3 by considering the delay and the noise frequency, in order to provide a proper low-pass filter and the k_{elas} represents the elastic model coefficient.

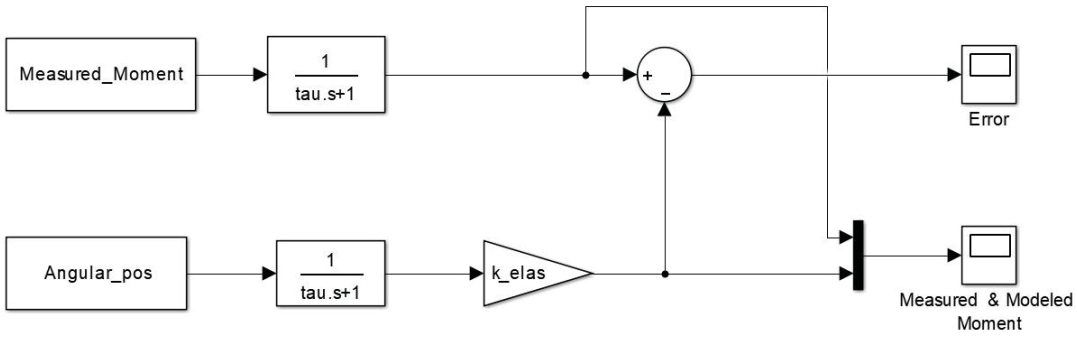

Figure 4.13. The Simulink model of an elastic tissue model

In a similar way, the rest of the investigated tissue models are developed in Simulink. In Figure 4.14, block diagram of Maxwell model is given where, b is the damping coefficient and $\alpha_{MW} = -\frac{b}{k}$. In the block diagram α_{MW} and b is represented as alpha_MW and beta_MW, respectively.

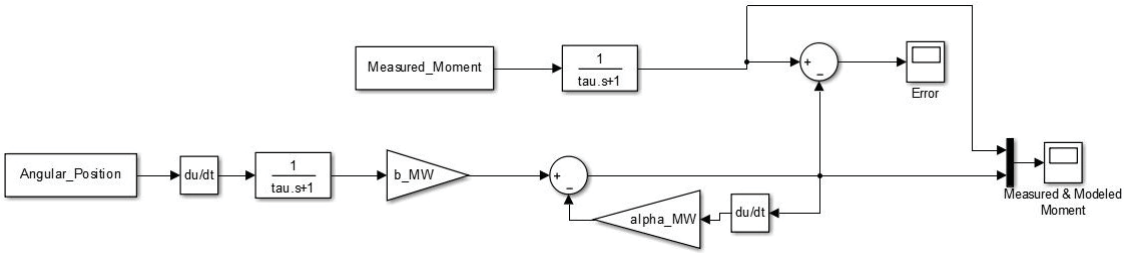

Figure 4.14. The Simulink model of Maxwell model

Figure 4.15 shows the Kelvin-Voight simulink model where k_kv and b_v are the spring and the damper terms, respectively.

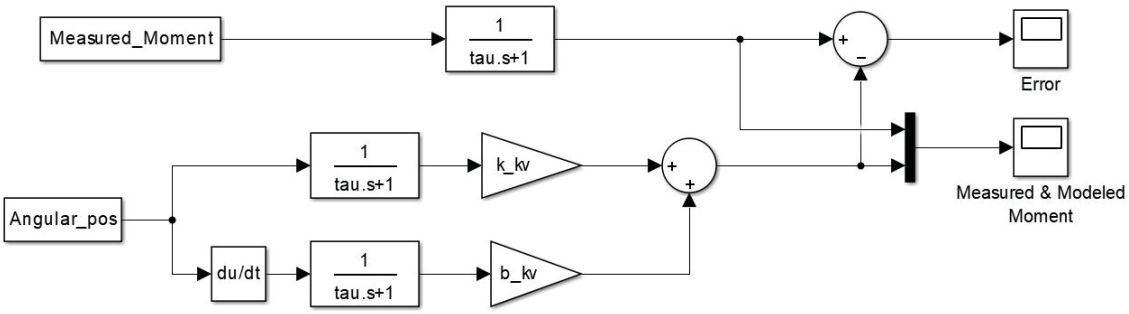

Figure 4.15. The Simulink model of Kelvin - Voight tissue model

Figure 4.16, shows the Kelvin-Boltzmann model. In this model, $\alpha_{kb} = \frac{bk_2}{k_1+k_2}$, $\beta_{kb} = \frac{k_1k_2}{k_1+k_2}$ and, $\delta_{kb} = \frac{b}{k_1+k_2}$. In the block digram, α_{kb}, β_{kb} and δ_{kb} is represented as alpha_kb, beta_kb and delta_kb, respectively.

Lastly, Figure 4.17 presents the simulation model of a non-linear Hunt-Crossley model. The β coefficient is a positive scalar and it ranges between 1.1 and 1.3 for the soft tissue as denoted in Moreira et al. (2014). In the simulation tests, β is taken as 1.2.

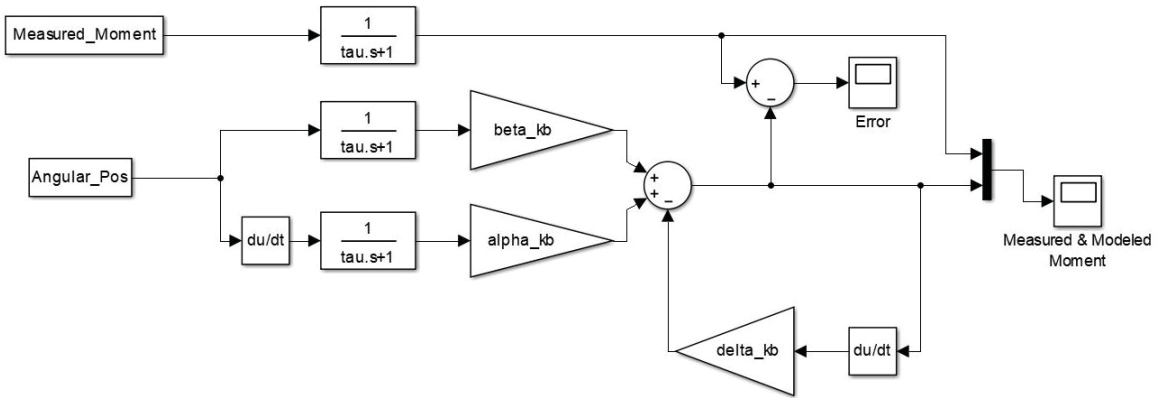

Figure 4.16. The Simulink model of Kelvin - Boltzmann tissue model

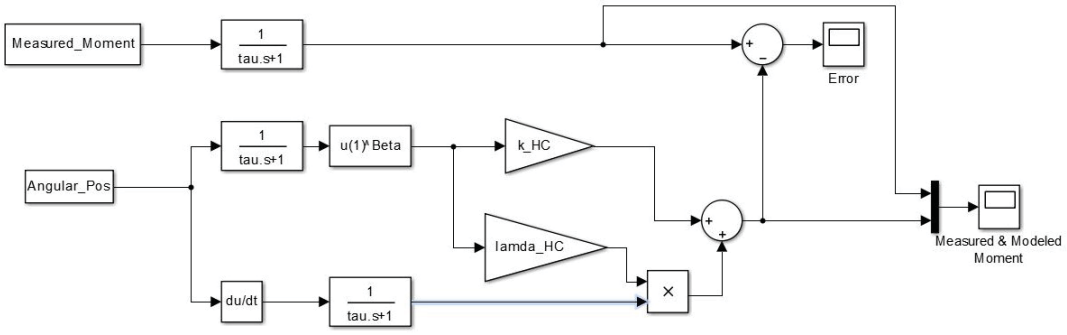

Figure 4.17. The Simulink model of Hunt - Crossley tissue model

2. The error function is minimized numerically

The error function is defined as the mean of the squares of error (MSE) and it is minimized by using `fmincon` function in Matlab. It is a nonlinear optimization function which finds a constrained minimum of a scalar function of several variables starting at an initial estimate. The initial estimations are chosen by some trial - error process and the lower boundary conditions of the optimization functions are defined as zero due to obtaining physically realistic results. The mean of the squares of error is given in Equation 4.4 where M_i is the modeled moment, M_m is the measured moment value and n is the total data number.

$$MSE = \sum_{i=1}^{n} (M_i - \bar{M}_m)^2 \tag{4.4}$$

Table 4.7 shows the identified parameters for the tip of the nose according to parameter estimation process. In this table, the unit of spring (k, k_1, k_2) and damper (b)

parameters are $\frac{Nm}{rad}$ and $\frac{Nm.s}{rad}$, respectively. It can be observed that the parameters are similar with each other for the all four experiments.

Table 4.7. Identified Parameters for the Tip of the Nose Models

		Experiments			
Models		#1	#2	#3	#4
Kelvin Boltzmann	k_2	0,455	1,208	0,860	1,363
	k_1	0,135	0,375	0,273	0,149
	b	16.270	28,457	24,695	25,105
Kelvin Voight	k	0,102	0,276	0,202	0,239
	b	0,209	0,115	0,448	0,593
Elastic	k	0,103	0,277	0,202	0,247
Maxwell	k	0,589	1,469	1,216	1,243
	b	101,309	125,209	127,071	127,302
Hunt Crossley	k	0,127	0,358	0,308	0,327
	λ	15,154	15,173	15,494	15,492

The moment is re-generated in Experiment # 1 by using identified parameters. The comparison between the measured and the modeled moment is given in Figure 4.18.

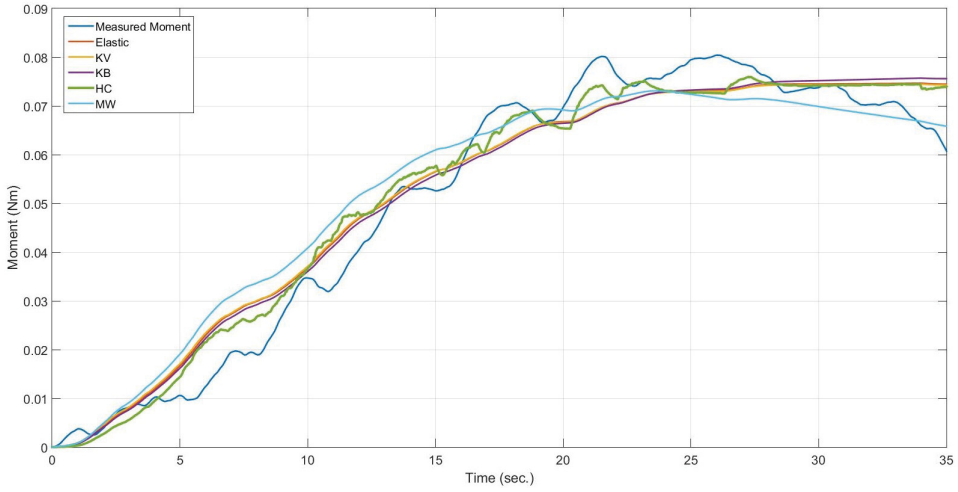

Figure 4.18. The comparison of the measured moment and five tissue models for the tip of the nose

The graphical representation of these models shows the ability of mimicking the real tissue dynamics. In order to compare these models quantitatively, root mean squares of the errors (RMSE) are calculated and compared in Table 4.8 and the minimum RMSE value received for the model of each experiment is highlighted with bold fonts. In each experiment, the maximum measured torque is approximately 0.08 Nm.

It is observed that the Kelvin-Boltzmann model resulted in the minimal errors in experiments #1,#3, #4 and Hunt-Crossley model has minimal error in experiment #2 which is quite similar with the Kelvin-Boltzmann model. Therefore, Kelvin Boltzman model, provides more realistic results with respect to the other models for the tip of the nose.

Table 4.8. RMSE between Measured and Calculated Moments for the Nose Tip Models

RMSE (Nm)				
	Experiments			
Models	#1	#2	#3	#4
Kelvin Boltzmann	**0,0036**	0,0056	**0,0058**	**0,0051**
Kelvin Voight	**0,0036**	0,0057	0,0059	0,0056
Elastic	**0,0036**	0,0056	0,0059	0,0058
Maxwell	0,0043	0,0069	0,0067	0,0056
Hunt Crossley	0,0046	**0,0053**	0,0060	0,0074

The cross-validation of the estimated parameters is realized for each measurement by using the average of the coefficients which are given in the Table 4.9 with their calculated RMSE. The results meet the expectations since the other studies in the literature show that the Kelvin-Boltzmann and Hunt-Crossley models have better performance relative to the others.

Table 4.9. RMSE between Measured and Calculated Force with Average Parameters of the Nose Tip Models

		Experiments				
			RMSE (Nm)			
Models		Avg. Coeff.	#1	#2	#3	#4
Kelvin Boltzmann	k_2 k_1 b	0,972 0,233 23,631	**0,0216**	0,0165	**0,0062**	0,0111
Kelvin Voight	k b	0,205 0,341	0,0235	0,0156	**0,0062**	0,0108
Elastic	k	0,207	0,0237	0,0155	**0,0062**	0,0114
Maxwell	k b	1,129 120,223	0,0217	0,0135	0,0068	0,0099
Hunt Crossley	k λ	0,280 15,328	0,0264	**0,0132**	0,0064	**0,0096**

The graphical representation of the cross-validation of experiment #3 is given in the Figure 4.19.

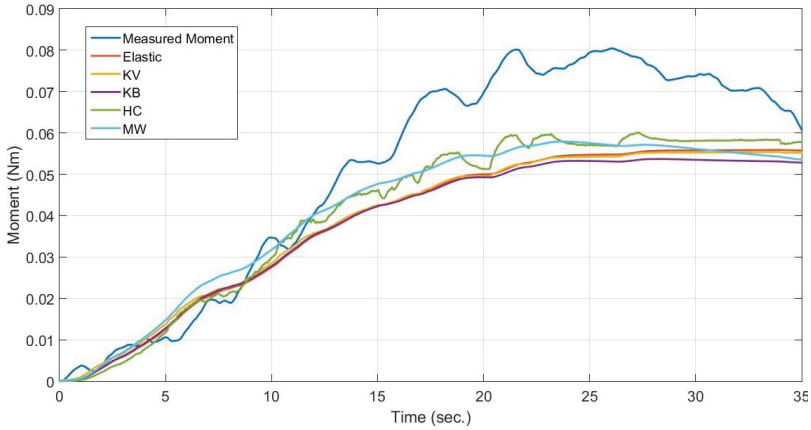

Figure 4.19. Cross validation of the experiment # 3 by using average coefficients

4.3.2.2. Nasal Concha Modeling Tests

In the endoscopic pituitary tumor surgery, the tip of the nose is the actual pivot point and the endoscope is expected to be in contact with this point during the operation. Hence, surgeons are asked to rotate the device around the tip of the nose and compress the nasal concha without interacting with pivot point for the nasal concha tissue modeling test. The schematic representation of the test is given in Figure 4.20. During the test process, no force applied to the nose tip by the surgeons.

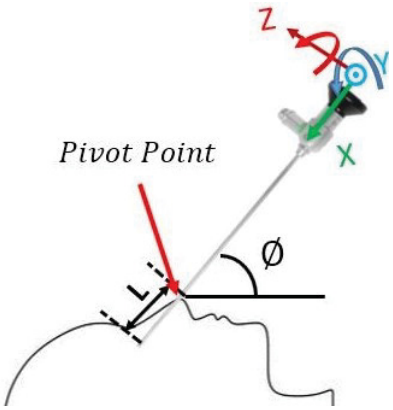

Figure 4.20. The schematic representation of the nasal concha modeling test

The parameter estimation process is realized by following the same procedure with the previous one. In this test, five data set is used for the identification. Table 4.10 presents the estimated parameters for each tissue model and results show that the parameters are similar to each other.

Table 4.10. Identified Parameters for the Nasal Concha Model

		Experiments				
Models		#1	#2	#3	#4	#5
Kelvin Boltzmann	k_2	3,829	3,700	4,198	2,993	1,795
	k_1	0,036	0,559	1,033	0,207	0,559
	b	26,357	32,038	33,878	29,029	30,979
Kelvin Voight	k	0,575	0,675	0,844	0,419	0,358
	b	0,733	0,236	1,525	1,773	0,517
Elastic	k	0,600	0,679	0,856	0,440	0,370
Maxwell	k	2,928	3,440	5,833	2,545	2,632
	b	137,166	136,950	139,842	136,699	138,644
Hunt Crossley	k	1,000	1,070	1,586	0,824	0,787
	λ	15,038	14,990	15,10	15,117	15,535

RMSE values of each model are given in Table 4.11 and the minimum-errors are highlighted by bold fonts. According to this table, Kelvin-Boltzmann has the best performance in experiment #1, #2, #3 and #4. In experiment #5, the minimum error is obtained when Hunt-Crossley model is applied.

Table 4.11. RMSE between Measured and Calculated Force for the Nasal Concha Models

RMSE (Nm)					
	Experiments				
Models	#1	#2	#3	#4	#5
Kelvin Boltzmann	**0,0039**	**0,0048**	**0,0034**	**0,0024**	0,0031
Kelvin Voight	0,0072	0,0068	0,0035	0,0033	0,0033
Elastic	0,0075	0,0068	0,0035	0,0036	0,0030
Maxwell	0,0068	0,0050	0,0050	0,0036	0,0059
Hunt Crossley	0,0128	0,0111	0,0049	0,0050	**0,0029**

The average values of the identified parameters are calculated in order to obtain approximate tissue model. The cross-validation is realized by using these values. The RMSE values are given in Table 4.12 and it is observed that Kelvin-Boltzmann model has the best performance in experiment #1 and #4. In experiment #2 and #5, the minimum error is observed when Hunt-Crossley model is applied. In contrast to other experiments, the elastic model has the best performance in experiment #3.

Table 4.12. RMSE between Measured and Obtained Force with Average Parameters of the Nasal Concha Models

		Experiments					
			RMSE (Nm)				
Models		Avg. Coeff.	#1	#2	#3	#4	#5
Kelvin Boltzmann	k_2 k_1 b	3,303 0,479 30,456	**0,0157**	0,0085	0,0128	**0,0055**	0,0080
Kelvin Voight	k b	0,574 0,957	0,0198	0,0114	0,0106	0,0064	0,0072
Elastic	k	0,589	0,0206	0,0110	**0,0104**	0,0066	0,0068
Maxwell	k b	3,476 137,860	0,0334	0,0111	0,0107	0,0083	0,0098
Hunt Crossley	k λ	1,054 15,158	0,0237	**0,0050**	0,0117	0,0068	**0,0048**

4.4. Conclusions

A remote center of motion kinematics based surgical robot mostly interacts with the tip of nose and tissue of the nasal concha in the endoscopic pituitary tumor surgery. The modeling of these interactions results in more precise controller design. A new hand-held device and the test procedure is designed and the proof-of-concept is realized as it presented in previous sections. Since the surgeon's hand motion cannot imitate a pure step input, the response of soft tissue under compression is considered by moments applied on it for the evaluation instead of evaluating interaction models by their stress relaxation and creep behavior.

Consistent results are obtained with relatively small errors and the approximate tissue models are determined. Since the Kelvin Boltzmann model is a linear model and it provides accurate results, it can be used for the controller design. In the following chapter, an impedance controller is designed by using these estimated models and the controller is experimentally verified.

CHAPTER 5

CONTROLLER DESIGN FOR ROBOT - TISSUE INTERACTION

In this chapter, the interaction between the surgical robot and the human nasal tissue is studied and a specialized motion controller is proposed for the endoscopic pituitary gland surgery case. The controller is tested in both simulation environment and with one Dof experimental set-up. In the following section, system modeling and controller design are presented. The simulation results for the predefined teleoperation case is given in the second section. In the fourth and the fifth sections, the experimental results are presented and discussed, respectively.

5.1. System Modeling and Controller Design

In order to design a proper controller, it is required to develop a mathematical model of the actuation system which consists of a DC motor, a brake, and a gearhead. The specifications of the selected DC motor is given in Table 5.1.

Table 5.1. Specification of Maxon RE25-339150 DC motor
(Source: Maxon, 2018)

Characteristics	**Value**	**Unit**	**Parameter**
Torque Constant	11.5	mNm/A	k_T
Rotor Inertia	14.5	gcm^2	J_r
Mechanical Time Constant	5.62	ms	τ
Nominal Voltage	12	V	V_N
Nominal Torque	27.5	mNm	T_N

The free body diagram of the motor is given in Figure 5.1. In this figure, ω_m represents the angular speed and $\dot{q}$ represents the output angular speed of the gearhead. The external torque which is generated due to the interaction of the telescope with the tissue is represented as τ_{ext}.

$$J_r\dot{\omega}_m + B_m\omega_m = k_t i - (J_{G\omega}\dot{\omega} + J_{G\dot{q}}\ddot{q} + B_{G\omega}\omega) - \frac{\tau_{ext}}{N} - \tau_f \tag{5.1}$$

Dynamic equation of the model is given in Equation 5.1 where the J_r is the rotor inertia, B_m is the viscous friction coefficient of the motor, and k_t is the torque constant. τ_f represents the torque loss due to the dry friction of the system.

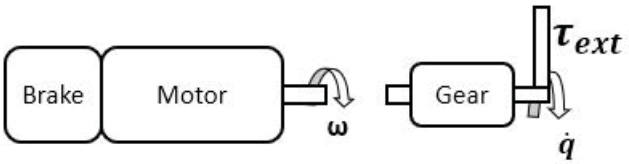

Figure 5.1. Dynamic model of the motor with gearhead and brake

The relation between the input and the output angular velocity is given in Equation 5.2. The inertia of the base gear which rotates at ω_m is given as $J_{G\omega_m}$ and $J_{G\dot{q}}$ represents the inertia of the follower gear which rotates at $\dot{q}$. Since the gear ratio, N, is 181, the output angular velocity is relatively small. Therefore, the viscous friction effect of the follower gear can be neglected. The viscous friction coefficient of the base gear is given as $B_{G\omega}$.

$$\omega = N\dot{q} \longrightarrow \dot{\omega} = N\ddot{q} \tag{5.2}$$

By substituting Equation 5.2 into the Equation 5.1 following equation is obtained where $J^\star$ and $B^\star$ represent the lumped coefficients. In order to experimentally validate the motor model, the Coulomb friction model is added to the input as a feed forward component in order to eliminate the nonlinear effects. The torque loss due to the dry friction is estimated experimentally as $\tau_f = 0.552\ \ mNm$.

$$\begin{aligned} N\ddot{q}(J_r + J_{G\omega} + \frac{J_{G\dot{q}}}{N}) + N\dot{q}(B + B_{G\omega}) &= k_t i - \frac{\tau_{ext}}{N} - \tau_f \\ J^\star\ddot{q} + B^\star\dot{q} &= \frac{k_t i}{N} - \frac{\tau_{ext}}{N^2} - \frac{\tau_f}{N} \end{aligned} \tag{5.3}$$

To derive the transfer function of the motor, external effects are taken out of the Equation 5.3 along with the Coulomb friction. By taking the Laplace transformation of the Equation 5.3, the transfer function between the torque input by the motor ,$\tau = k_t i$, and the angular velocity is defined in Equation 5.4.

$$\frac{\dot{q}(s)}{\tau(s)} = \frac{1}{N(J^\star s + B^\star)} \tag{5.4}$$

A set of experiments are conducted to obtain the frequency response of the actuation system. As a result of these experiments a Bode plot is computed. From the Bode

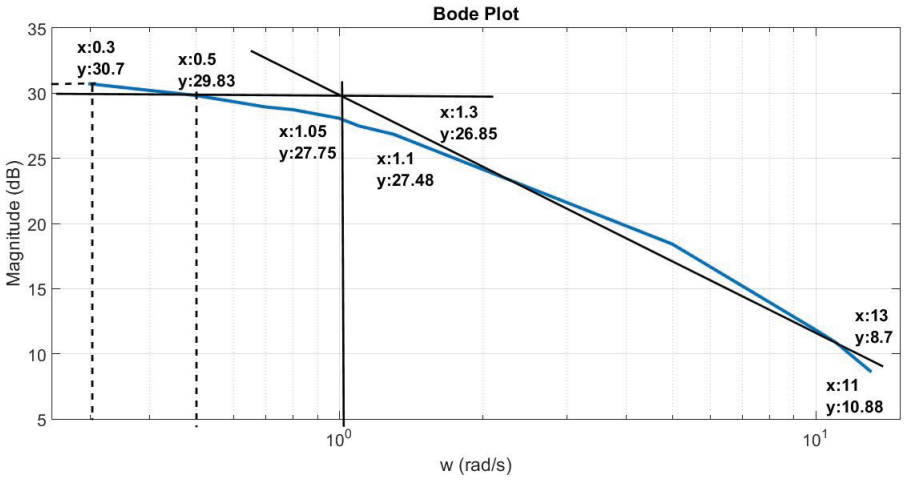

Figure 5.2. Frequency response analysis of the system

plot which is given in Figure 5.2, parameters of the transfer function can be obtained by using Equation 5.5 where the k_t is torque constant of the motor.

$$\begin{aligned} 20log(\frac{k_t}{NB^\star}) &= 30dB \\ \frac{B^\star}{J^\star} &= 1.05\frac{rad}{s} \end{aligned} \tag{5.5}$$

The model parameters are calculated as $B^\star = 2.009 \times 10^{-6}[kgm^2/s]$ and $J^\star = 1.913 \times 10^{-6}[kgm^2]$.

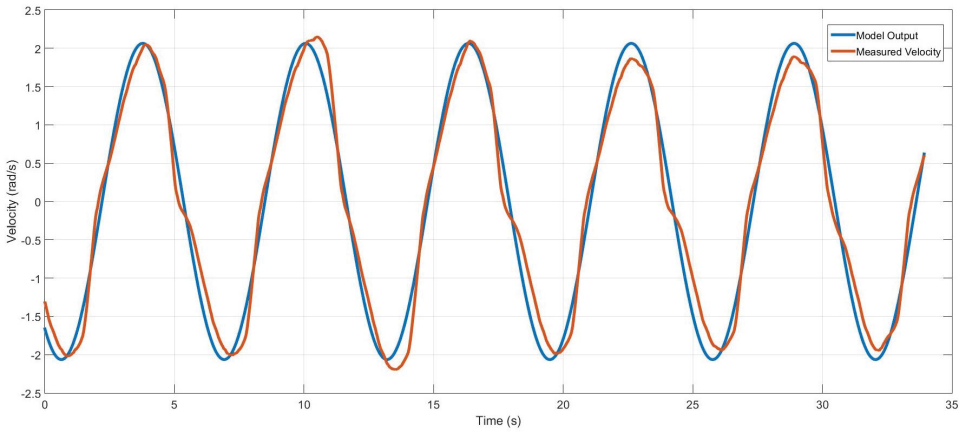

Figure 5.3. Model verification of the system

Figure 5.3, represents the model verification by using estimated model parameters. This verification is realized by applying sinusoidal current input to the system with $1rad/s$ frequency and $0.09A$ amplitude. The error mostly occurs when the direction of

the velocity changed. This can be overcome by improving system identification procedure such as increasing the measured data points.

The NeuRoboScope robot has a real-time teleoperation control capability which is composed of a wearable ring system that captures and transmits voluntary hand motions of the surgeon over a wireless connection to a slave system. Accordingly, the slave system processes the received data to generate velocity demands for the robot endoscope controller. The simplified block diagram of the motion controller is presented in Figure 5.4 where ω_r, θ_r, and θ_m are the velocity reference, generated position reference, and the measured position, respectively. G_c represents the transfer function of the controller, G_p represents the transfer function of the plant which is defined in Equation 5.4. This controller diagram represents the pure position controller, however, different scenarios requires modification on this controller. The different cases will be defined in next section.

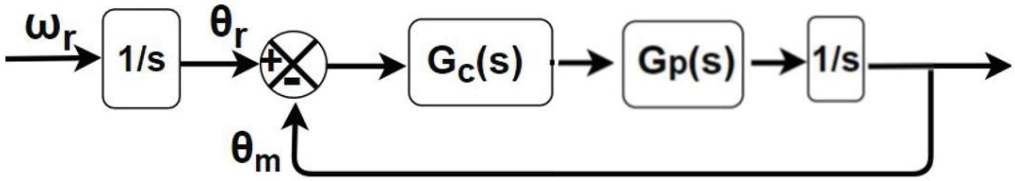

Figure 5.4. Block diagram of the position control algorithm

G_c is selected as a PD controller and the gains are obtained by using the root locus method. The open loop transfer function of the controlled system is given in Equation 5.6 where z, p, K_p, and K_d represents the zeros and poles of the open loop transfer function, proportional gain and the derivative gain, respectively.

$$\begin{aligned} G_o(s) &= \frac{K_p + K_d s}{N(J^\star s^2 + B^\star s)} \\ z = -\frac{K_p}{K_d}, \quad p_1 = 0, \quad p_2 &= -\frac{B^\star}{J^\star} = 1.05 \end{aligned} \tag{5.6}$$

The controller's performance criteria are defined by considering the capability of the DC motor. These performance criteria are given in Equation 5.7 where the mechanical time constant,τ_s, is $5.62ms$.

$$\begin{aligned} T_s = 4 * \tau_s = \frac{4}{\zeta\omega_n} &\cong 0.023 \ \ sec \\ \zeta = 0.707, \quad \zeta\omega_n &\cong 177.94 \ \ rad/s \end{aligned} \tag{5.7}$$

The s-plane with open loop poles and the zero are given in Figure 5.5 along with the desired pole location s_1 which is calculated according to the Equation 5.7. By using the angle and magnitude conditions of the root locus method, placement of the zero is calculated as 178.47 and the controller gains are calculated as $K_p = 21.77$ and $K_d = 0.122$.

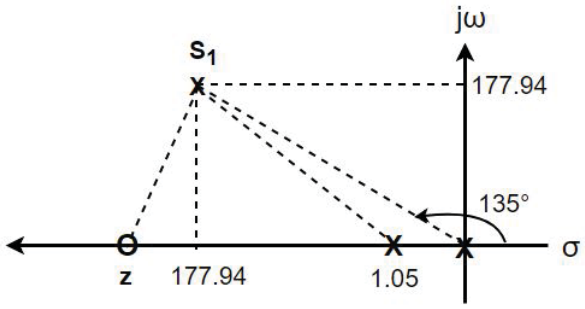

Figure 5.5. Desired pole location for PD controller

Steady state error for the designed PD controller is calculated with respect to Equation 5.8 where $E(s)$ is the error transfer function. In NeuRoboScope, velocity demand is provided by the surgeon at 100 Hz sampling rate however, the controller works at higher frequencies. The reference input can be defined as a step change, therefore, the generated position reference introduced to the controller is a ramp input.

$$E(s) = \frac{1}{1 + G_o} = \frac{N(J^\star s^2 + B^\star s)}{N(J^\star s^2 + B^\star s) + K_p + K_d s} \tag{5.8}$$

For a unit step input, steady state error goes to the zero.

$$e_{ss} = \lim_{s \to 0}(sE(s)\frac{1}{s}) = 0 \tag{5.9}$$

For a unit ramp input steady state error approaches to a constant value which depends on the proportional gain.

$$e_{ss} = \lim_{s \to 0}(sE(s)\frac{1}{s^2}) = \frac{NB^\star}{K_p} \tag{5.10}$$

For calculated controller gains the steady state error is $e_{ss} = 1.67 \times 10^{-5}\ rad$ which is an acceptable error value.

In order to develop and test the interaction control, a single DoF experimental setup designed. The components of the experimental set-up are presented in Figure 5.6.

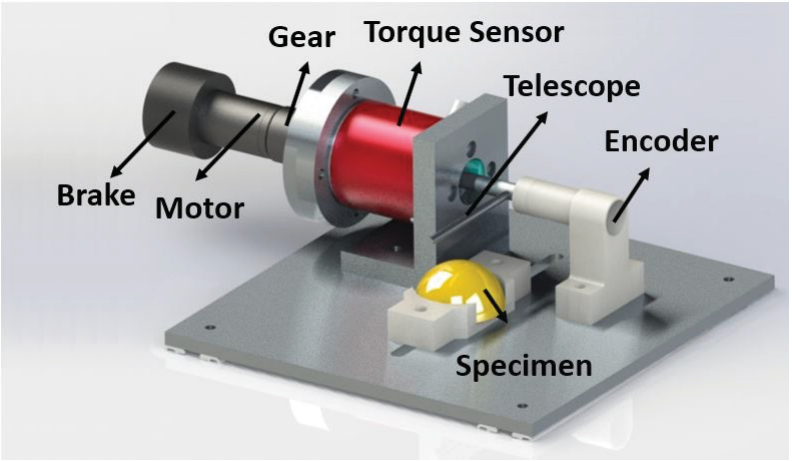

Figure 5.6. The CAD model of the experimental set-up

To mimic the motion of the endoscope, a DC motor (Maxon RE25-339155) with the planetary gearhead (Maxon GP26A) and a brake (Maxon Brake AB28) is assembled into the system. A reaction type torque sensor (Futek TFF400) is used in order to measure the applied external torque due to the interaction with the specimen. The angular position is measured by using an optical quadrature encoder (AEDA-3300AT). The part called as telescope simulates the actual telescope that is used during the surgery. For running the controller and the data acquisition purposes, MyRIO DAQ board is used combined with the Labview programming environment.

The torque sensor is calibrated by applying predefined moment values with using calibrated weights. The results are given in Table 5.2. The maximum error value is below the 2% since the maximum range of the sensor is $1.23\ \ Nm$, this error is found acceptable for this experiment.

Table 5.2. Futek TFF400 Torque Sensor Calibration Validation

Mass(g)	**Applied Moment (Nm)**	**Measured Moment (Nm)**	**Error (%)**
20	0,0108	0,0107	0,8307
50	0,0271	0,0271	0,0004
70	0,0379	0,0375	1,1601
100	0,0542	0,0546	0,7375
200	0,1084	0,1097	1,1987
500	0,2710	0,2703	0,2587

5.2. The Case Study

The control scenario of the teleoperation control of the endoscope holder robot starts by receiving the velocity demand. Surgeon starts to generate velocity demand by pressing the foot pedal, then by using wearable ring system the voluntary hand motions are captured and transmitted to the slave system via a wireless connection. The NeuRoboScope system's endoscope holder robot contains DC motors with gearhead and break. The breaks are used to increase the safety in case of an emergency such as a power cut. When the surgeon does not want to move the endoscope or already reached the external torque limit due to the robot tissue interaction, the breaks are activated to restrict the motion.

Since the NeuRoboScope robot is a non-backdrivable system with a relatively high reduction ratio due to its gear-head(1:181) and the additional capstan drive(1:5), external torque has a very small effect on the system, hence, pure position control can be implemented. However, for direct drive systems, position control should be modified to reduce the effects of external torque.

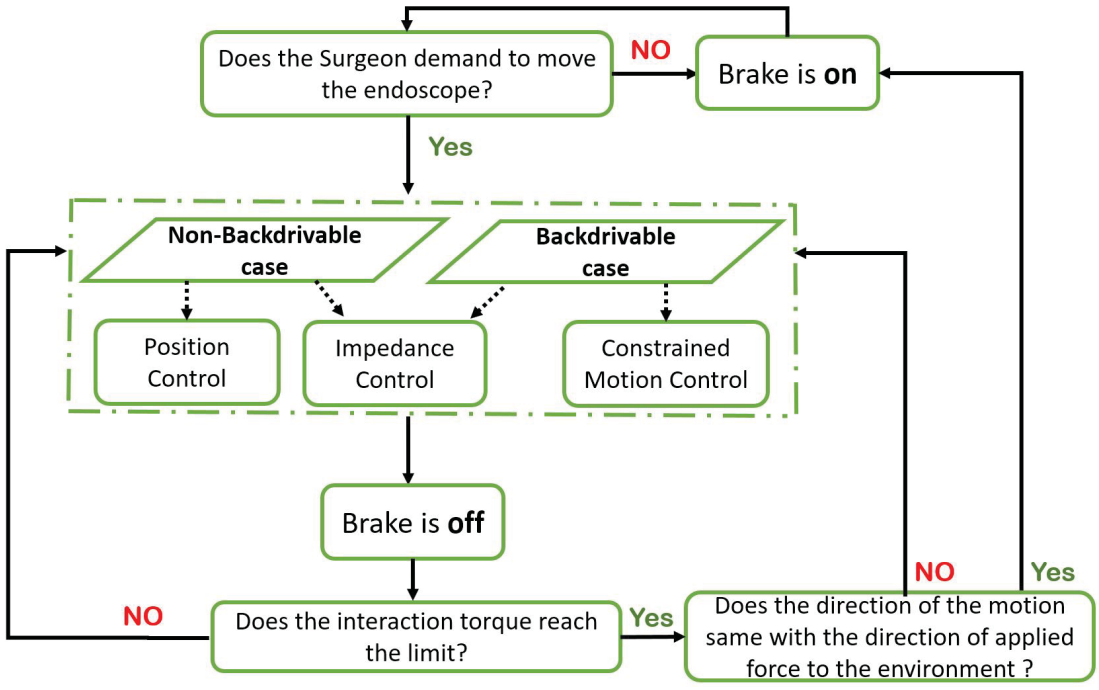

Figure 5.7. Flowchart of the controller for the surgical scenario

Figure 5.7, represents the flowchart of the control algorithm for both non backdrivable and backdrivable cases. Although the external torque has no significant effects

on the non backdrivable system, the existence of the break and a torque limit requires an application based modifications, therefore, this flowchart presents the overall procedure.

The procedure starts with the motion demand from the surgeon by pressing to the foot pedal. Then the controller is activated and the brakes are released. If the interaction torque does not reach to the limit value, then the motion control continues during the surgeon's demand. If the interaction occurs and the torque reaches to the limit and the surgeon still demands to move the endoscope through soft tissue then the brakes are activated and the motion is restricted. If the surgeon demands to move the endoscope outside to the soft tissue then the brakes are released and the control is activated again.

5.3. Simulations and Experimental Results

The performance of the proposed controller is evaluated by using the model built by using SimMechanics blocks within Matlab Simulink simulation environment. In addition to that, since the non-backdrivable system's actuation system is readily available, controllers are experimentally tested in a one DoF test set-up.

5.3.1. Non-Backdrivable Case

For the non-back drivable systems such as the NeuRoboScope robot, a pure position controller, and the impedance controller can be applied due to the aforementioned surgical scenario.

5.3.1.1. Pure Position Control

When there is more than one DoF in a robotic system and the speed reduction ratio is high enough, for a common control method is the independent joint controller. In this controller, each joint is controlled by a motion control algorithm disregarding the effects of other joints' motion. This effect of other joints' motion can be regarded as external force. This external force effect on the joint reduces with the square of the reduction ratio as shown in Equation 5.3.

The corresponding controller is represented in Figure 5.8 where θ_e and K_E are the position and the stiffness of the environment, respectively. This control algorithm is

tested in both simulation environment and experimental set-up.

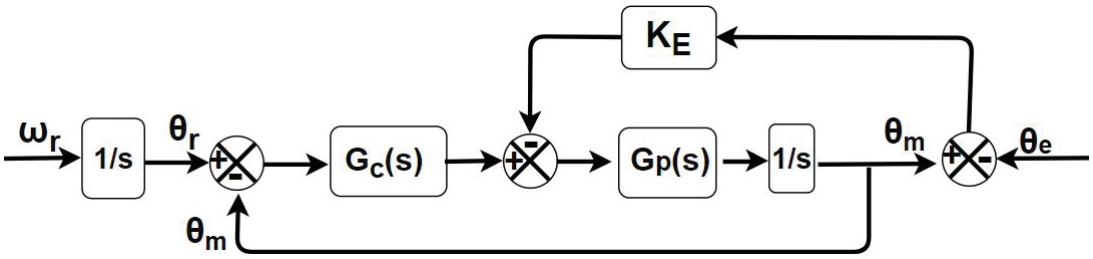

Figure 5.8. Block diagram of position controller in a constrained environment

The model of the DC motor, which is modeled in the previous section, is constructed in simulation environment and a PD controller is implemented for the position control. A step velocity reference is applied to the system via joystick and a button is used to mimic the foot pedal. By integrating the velocity input, ω_r, position reference is generated. In order to obtain external torque,τ_{ext}, value due to the interaction with the soft tissue, a soft tissue model is implemented. Kelvin-Boltzmann model of the human nasal concha is used in simulations. The information flow between the system components is given in following figure where u is the control input.

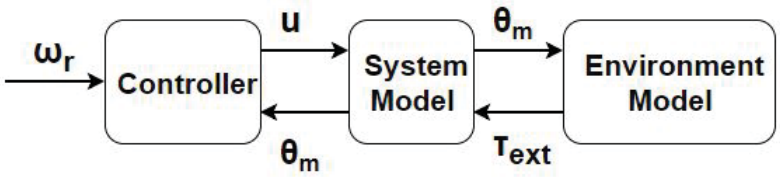

Figure 5.9. Simulation information flow

In Figure 5.10 simulation results are presented. At the beginning of the simulation break is on, which means motion is restricted, then the pedal is pressed and the break goes into the off state then the motor starts to follow the reference. When the position of the system reaches $0.5rad$, telescope starts to interact with the soft tissue and the external torque starts to increase. Then the pedal is released before the reaching torque limit which is $0.4Nm$.

In situation 1, which is presented with a vertical dashed line, the break is released but the position of the telescope did not change. This shows that controller can compensate for the effects of the external torque thanks to its non-backdrivable composition. In situation 2, external torque reaches limit and the system is locked by activating the

break even though the reference value is increased. In situation 3, the direction of the velocity demand is changed hence the break is released. Simultaneously, reference value is pullback to the measured position in order to prevent higher control inputs due to the increased error value.

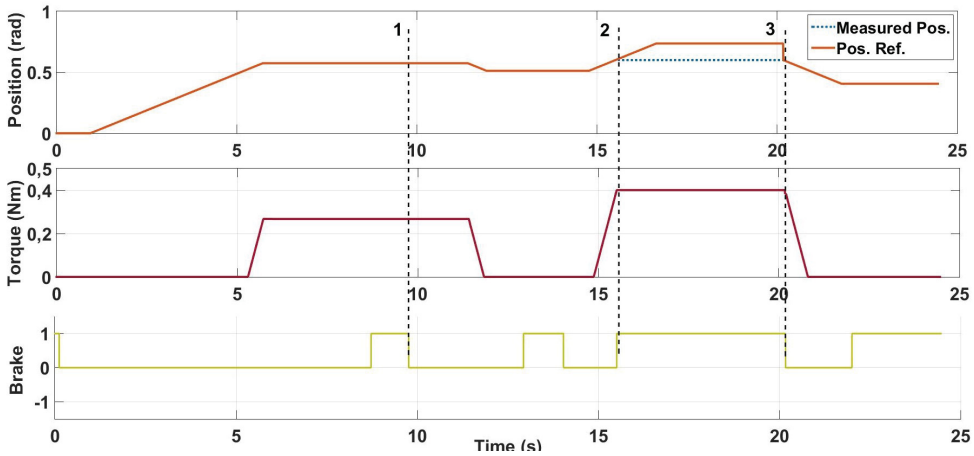

Figure 5.10. Simulation results of the pure position controller

Pure position controller and the proposed algorithm is also experimentally tested by using the experimental set-up which is shown in Figure 5.11.

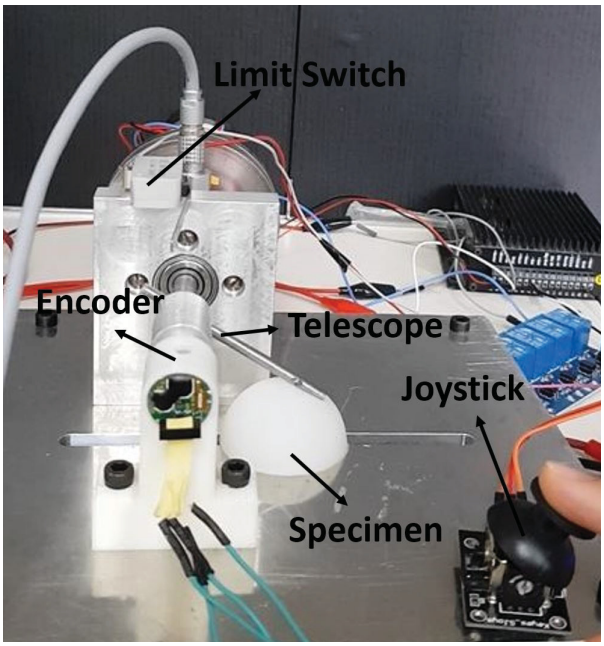

Figure 5.11. Experimental set-up with a silicone specimen

The velocity input is provided by using an analog joystick. Since the encoder is an incremental type, the initial position should be defined. To realize this homing process, a limit switch is attached to the system. In addition to that, to eliminate the nonlinear effect of the gravity due to the weight of the telescope, a gravitational term is added to the system.

The experimental results are presented in Figure 5.12. In situations, 1 and 2, telescope reached the interaction torque limit ($0.1Nm$) and the brake is activated. Similar behavior can be observed in situations 4 and 5 with the $0.3Nm$ and $0.01Nm$ torque limits, respectively. In situation 3, the brake is activated externally, therefore the motion is restricted and reference signal starts to increase. When the brake is released the reference signal is set to the measured position to prevent undesired movements.

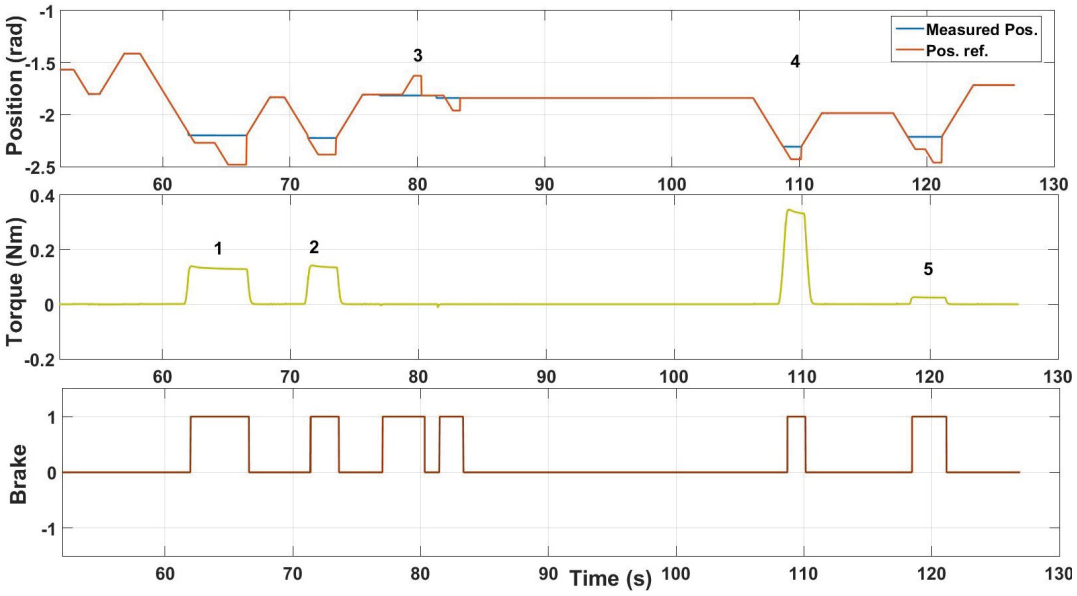

Figure 5.12. Experimental results of the pure position control

5.3.1.2. Impedance Control

By applying impedance controller, the dynamics of the interaction can be controlled by relating external torque acting on the telescope with its' velocity.

As in the previous controller case, velocity is the reference input, however, in order to design proper impedance controller, controller scheme of the pure position controller can be modified as in Figure 5.13, where the desired external torque, T_d, is defined as zero and the reference position input is considered as a disturbance. This approach allows to

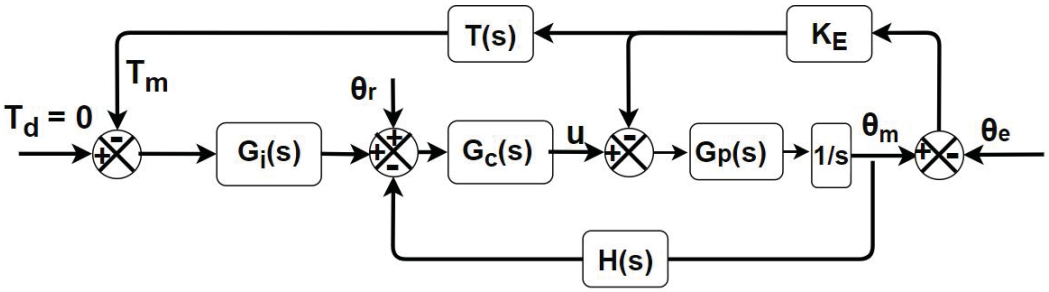

Figure 5.13. Block diagram of the impedance controller

simplify the block diagram and selecting the impedance term's parameters. In this figure, $G_i(s)$ is the transfer function of the impedance term, K_E is the environment model which is estimated as an elastic model of the nasal concha in Chapter 4. In order to simplify the controller design process, the elastic model is selected instead of Kelvin-Boltzmann model. $T(s)$ and $H(s)$ are the transfer functions of the encoder and the torque sensor, respectively. It is assumed that these sensors work much faster than the mechanical parts, therefore, the values of them are taken as 1.

Block diagram reduction is realized to obtain open loop poles and zeros. Impedance term is selected as Maxwell model and the corresponding transfer function is given in Equation 5.11 where the damping and spring terms are represented as b and k, respectively.

$$G_i(s) = \frac{bs + k}{kbs} \tag{5.11}$$

The overall open loop transfer function, $G_m(s)$, of the presented controller is given in Equation 5.12.

$$\begin{aligned} G_m(s) &= \frac{\alpha^\star s^2 + \beta^\star s + \gamma^\star}{J^\sharp s^3 + B^\sharp s^2 + C^\sharp s} \\ \alpha^\star &= K_d b K_e, & \beta^\star &= K_p K_e b + K_d k K_e \\ \gamma^\star &= K_p k K_e, & J^\sharp &= kbJ \\ B^\sharp &= kbB + kbK_d, & C^\sharp &= kbK_e + K_p kb \end{aligned} \tag{5.12}$$

Parameters of the impedance controller can be selected by root locus method in accordance with the design criteria which are damping ratio ζ and the desired natural frequency. The inner loop of the controller should be faster than the outer loop, therefore, the upper limit of the ω_n for the designed controller should be the natural frequency of the inner position controller which is $251.68\ rad/s$. For that reason, impedance parameters

define the dominant poles.

In order to plot the root-locus graph for investigating the effect of impedance parameters, the open-loop transfer function needs to be re-organized. In Equation 5.13, the re-organized TF is given for the k as an open loop gain.

$$TF = \left(\frac{1}{k}\right)\frac{bK_dK_es^2 + bK_pK_es}{Jbs^3 + (bB + bK_d)s^2 + (K_dK_e + bK_e + bK_p)s + K_pK_e} \tag{5.13}$$

When the damping parameter, b, is selected as $0.5\ \ Nm.s/rad$, the root-locus plot is obtained as following Figure 5.14. It can be observed from the figure, the position controller related poles are much more far to the left from the other pole which is the dominant pole.

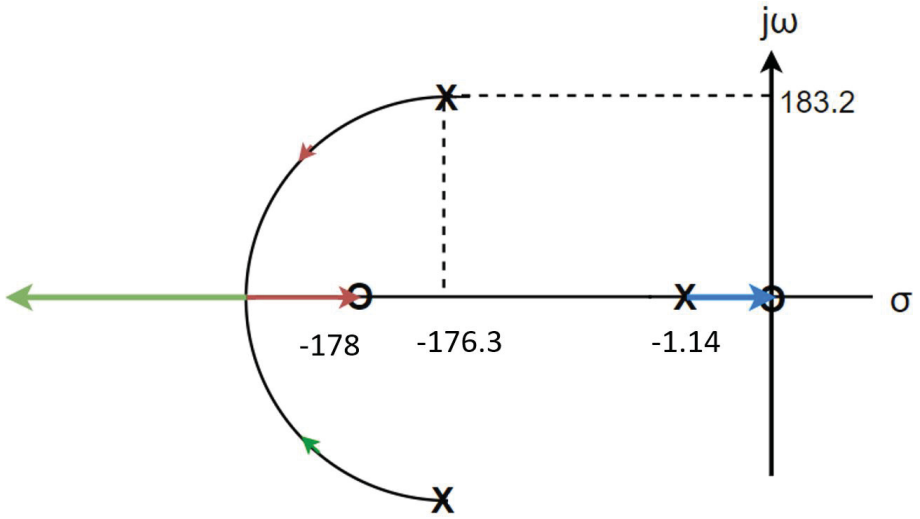

Figure 5.14. Root locus plot of the re-organized openloop transfer function

In order the simplify the calculations, the transfer function of the inner loop can be assumed as 1, then it is possible to investigate the effect of the impedance term alone. In Equation 5.14, re-organized open loop transfer function of the impedance term is given.

$$G_{o,i} = \left(\frac{1}{k}\right)\frac{bK_es}{bs + K_e} \tag{5.14}$$

The corresponding root locus plot is represented in Figure 5.15. For different frequencies, different k values can be obtained. The pole is located by defining $b = 0.5$ then, the gain can be found as 0.3 where the frequency is $1\ \ rad/s$. Therefore, k parameter is calculated as $3.33\ \ Nm/rad$.

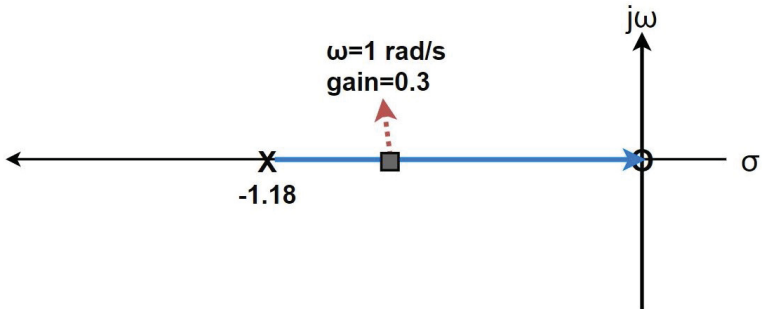

Figure 5.15. Root locus plot of the re-organized openloop transfer function of the impedance term

The simulation results for the impedance control is given in Figure 5.16. In situation 1, the interaction is started then, the external torque started to the increase. Since the impedance control regulates the position reference, the external torque settles at some point and the no more interaction is possible into the tissue. This behavior can be observed in the position graph. Even though an increased position input is generated due to the step velocity demand by the surgeon, this position reference is absorbed by the impedance term. Because of this reason, the measured position and the reference position lines are coincident in the graph.

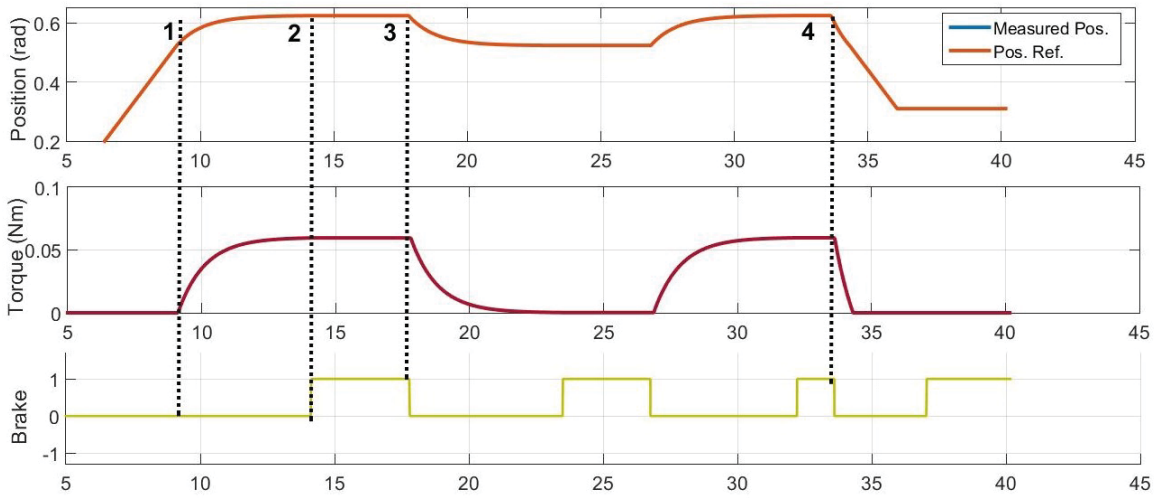

Figure 5.16. Simulation results of the impedance controller

In situation 2, the brake is triggered externally and the position is kept constant until to the situation 3. After that point brake is released and endoscope started to move slowly without giving the velocity reference. Even though this behavior generates undesired movement, it can be regulated by adjusting different impedance parameters. In

addition to that, this behavior can be occurred when the foot pedal is pressed but there is no velocity input from the surgeon, which is not a common case.

In situation 4, the same procedure is followed, but this time when the brake is released the velocity reference is given to the endoscope through the outside of the soft tissue. As is it can be observed from the torque graph, the external torque vanishes faster. This behavior does not introduce a safety problem to the procedure.

Impedance control is also tested experimentally. In these experiments, impedance term is defined as a mass-damper term and the corresponding transfer function is given in Equation 5.15.

$$G_{imp_2} = \frac{1}{ms^2 + bs} \tag{5.15}$$

The open-loop transfer function is re-organized to define damper parameter as an open loop gain which is given in Equation 5.16 where the Ks is the model of the environment.

$$G_{o,imp_2} = \left(\frac{1}{b}\right)\frac{ms^2 + Ks}{bs} \tag{5.16}$$

In the experiment, a silicone specimen is used to mimic the soft tissue. In order to model the specimen, the interaction is realized by using experimental set-up. The telescope is penetrated to the specimen as $0.1 \ \ rad$ by implementing position control. The external torque is measured by using torque sensor. The obtained results are given in Figure 5.17. The elastic model of the silicone is estimated as $K_s = 1.018 \ \ Nm/rad$ by following the estimation procedure in Chapter 4.

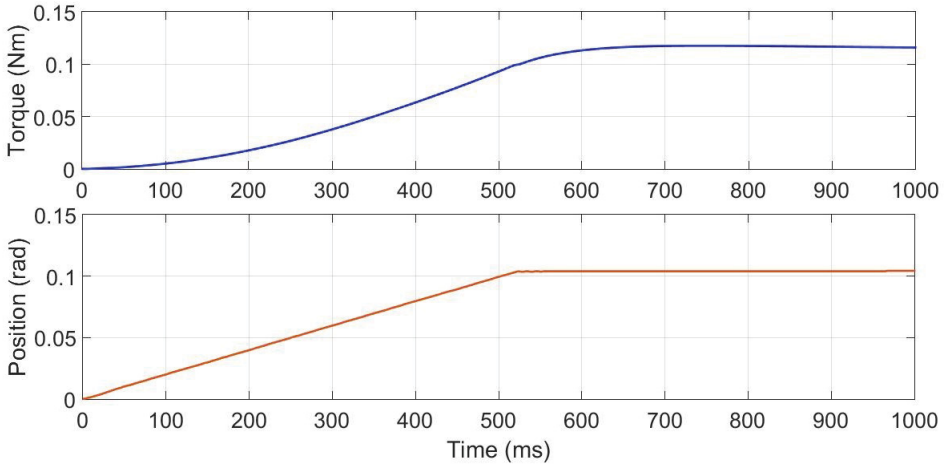

Figure 5.17. Angular position and measure torque from the specimen

The effect of the damping parameter can be observed from the root locus plot which is represented in Figure 5.18.

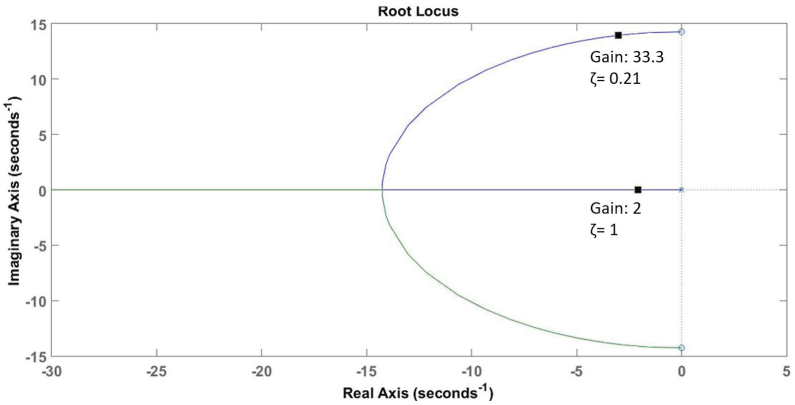

Figure 5.18. Root locus plot of the reorganized mass-damper impedance term

In this figure, mass parameter as selected as $m = 0.005\ \ kg$ and 2 different damper gain is selected as $b_1 = 0.03\ \ Nms/rad$ and $b_2 = 0.5\ \ Nms/rad$ to observe the effect of the damping ratio (ζ).

The experimental results of the impedance controller are represented in Figure 5.19. In situation 1, the interaction is started and the torque is increased. The difference between the reference position and the measured position is compensated by the impedance term. Therefore, the interaction torque has reached to a limit value. Due to the selected damping gain, a damped oscillation is observed when the interaction has occurred.

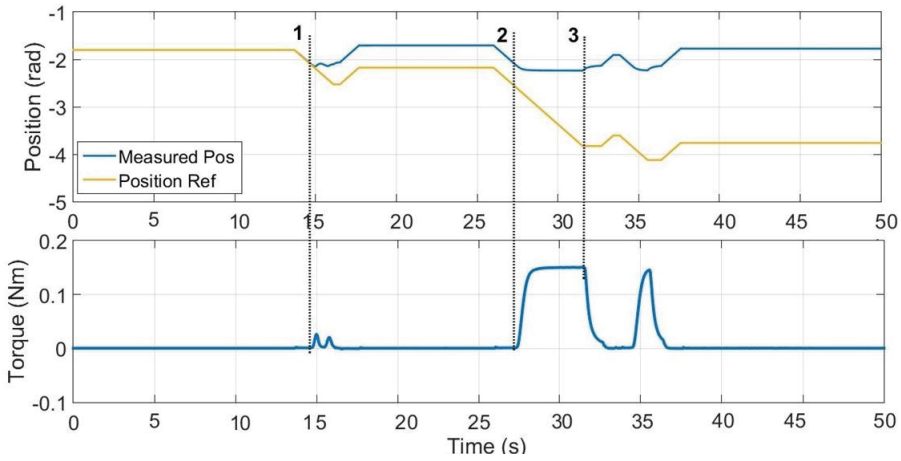

Figure 5.19. Experimental results of the impedance controller

In situation 2, the interaction occurred but this time the damper term b_2 is used. With this new parameter, the controller moves the endoscope to penetrate the tissue without any oscillation. However, the applied torque value is increased. This dynamic be-

havior can be arranged by defining mass and damper values by considering the effects of the ζ and the applied torque limit. In situation 3, the velocity reference is set to zero, consequently the endoscope started to move out slowly from the tissue.

The difference between the reference position and the measured position is increased due to the integral effect of the impedance term. This difference is not the error of the controller, it is compensated by the impedance term. The actual input from the surgeon is the velocity and the position is generated in the controller algorithm. Therefore, the controller is capable of following the reference velocity even though position difference is increased.

5.3.2. Backdrivable Case

The surgical scenario can be realized by using a back-drivable system, however, in these systems, external torque applied on the robot has a much more powerful effect on the controller. Therefore, pure position control scheme has to be modified to a constrained motion controller.

5.3.2.1. Constrained Motion Control

The main purpose of the constrained motion control is rejecting the effect of the external torque due to the interaction with the soft tissue. This can be archived in two ways. Firstly, as an ideal case, external torque can be estimated by using proper torque sensor then adding it to the control input, pure position control can be achieved. Another way to eliminate this effect is by converting the measured external torque to the position data by adding another transfer function to the controller. Figure 5.20, represents the constrained motion control with two cases.

T_{ext} term with the dashed line represents the first case of constrained motion. This controller requires a good torque sensor in terms of sensitivity, repeatability, and resolution. Since this data is added to the control input, the measurement errors due to noise will be amplified by the actuator. So, it might be necessary to use a filter. Simulations are carried out to test this controller. In these simulations, the proposed surgical scenario is followed. The DC motor is modeled without the gearhead. The torque sensor which is used in experimental set-up has some noise due to analog measurements. In the simulations, this noise is considered as white noise with the amplitude of $4\ mNm$ which is the

observed value from the sensor.

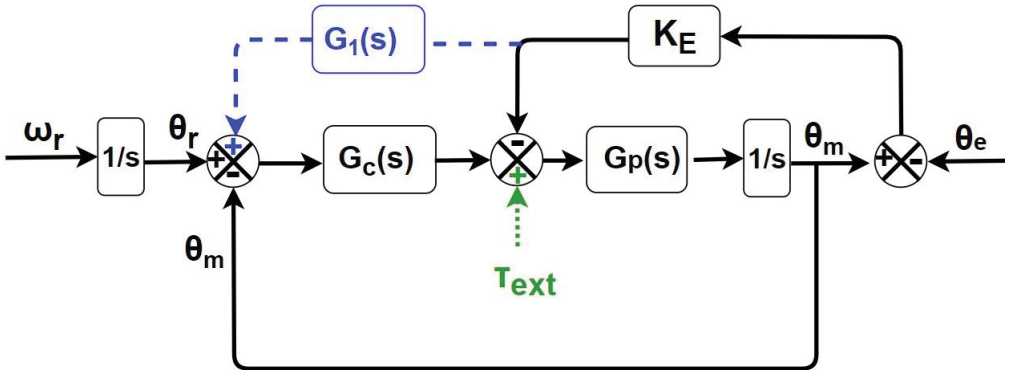

Figure 5.20. Constrained motion controller algorithm with two possible ways

Figure 5.21, represents the result of a simulation for the case of a pure position controller on the back drivable system. The experiment is started with the constant velocity reference. In situation 1 which is highlighted with the vertical dashed line, the interaction is initiated. The noisy torque value started to increase until situation 2. At this point, velocity reference is set to zero without activating the brakes. In the situation 3, the brake is triggered externally. In situation 4, the brake is released therefore, the applied torque is dropped to the zero immediately. This is a result of the external torque which has a more powerful effect with respect to the non-back drivable case. Similar behavior can be observed at the 14^{th} second in the figure. This is an undesired behavior in the surgical procedure, therefore, it should be compensated.

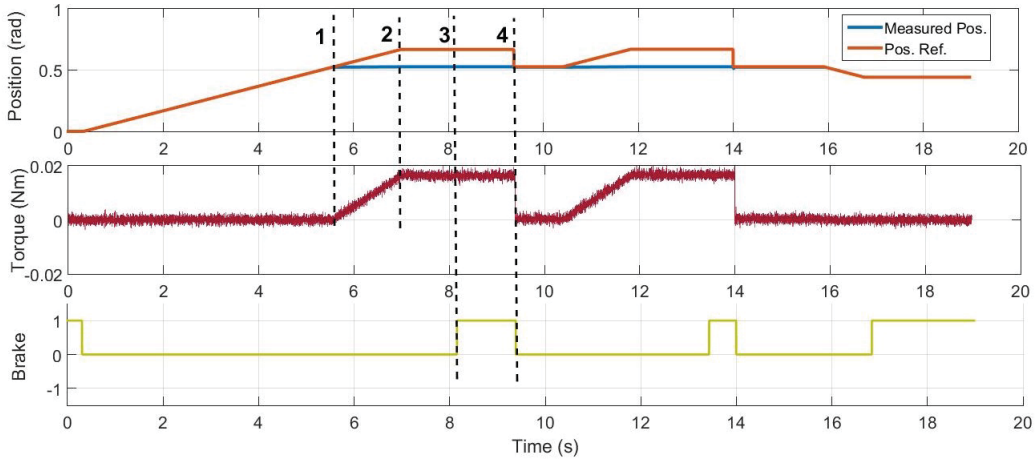

Figure 5.21. Simulation results of the pure position controller for the backdrivable case

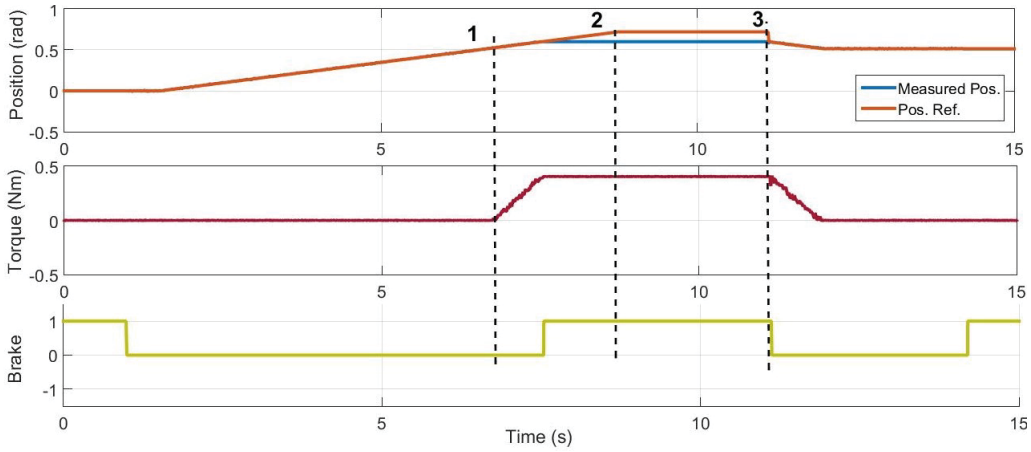

Figure 5.22. Simulation results of the constrained motion controller with adding disturbance

Figure 5.22 shows the result of the constrained motion control. In this simulation effect of the external torque is compensated by adding the noisy torque data to the control input. The procedure is kept same as the previous one in situations 1 and 2. The effect of the compensation can be observed in situation 3. Even though the break was released, the position of the telescope did not change immediately.

The second method of the constrained motion is represented in Figure 5.20 by adding the transfer function, $G_1(s)$, to the controller. This allows to regulate the external torque value. The difference of this method from the previous one is that the obtained position data enters to the PD controller. By defining the $G_1(s)$ as the reciprocal of the PD controller which is the special case of the impedance controller, a similar result can be obtained.

In Figure 5.23, simulation results of the constrained motion controller with position regulation are presented. Between the situations 1 and 2, the brake was activated externally. When the brake released, the position of the telescope did not change. The similar behavior can be observed between the situations 3 and 4. In situation 3, the torque had reached to the limit therefore the brake was activated. Since the torque data has noise on it, the state of the brake is changed rapidly between the seconds 16 and 17. Although it has no noticeable effect on the position, it can be harmful to the brake system. The possible solution might be applying a proper filter for the torque data.

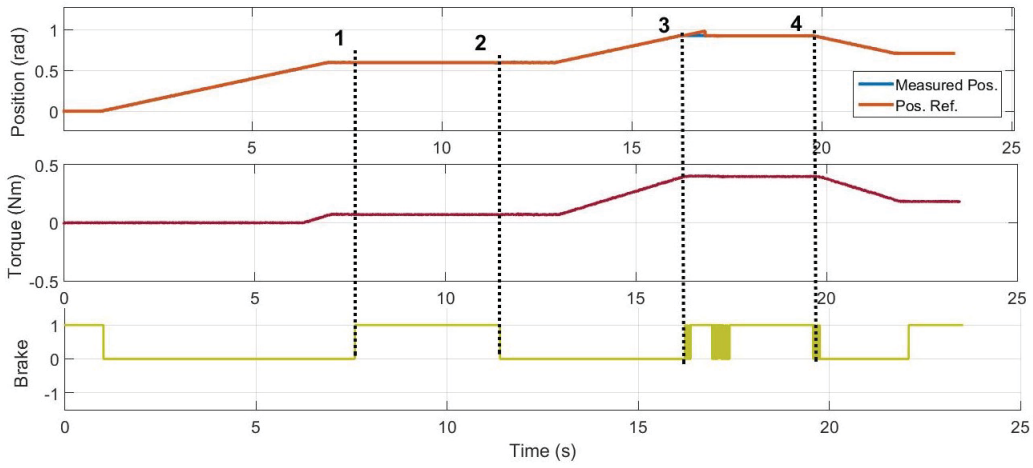

Figure 5.23. Simulation results of the constrained motion controller with position regulation

5.4. Conclusions and Discussions

In the robotic pituitary gland surgery, the surgeon provides velocity demand by using wearable ring system and a foot pedal. When the pedal is pressed system allows the surgeon to provide a reference data and the endoscope is move by the robot inside the human nasal cavity. The robot has to comply with the environment in order not to apply excessive forces to the tissue surrounding the endoscope. Therefore, the motion is constrained by these tissues. When the pedal is released the brakes are activated and the motion is restricted. This teleoperation scenario requires an application based controller design. In the scope of this Chapter, a control algorithm is proposed for the NeuRoboScope project's endoscope holder robot and in addition, this algorithm is extended for the back-drivable case.

The proposed control scenario is tested in both simulation environment and via an experimental set-up. The actuation system is modeled in order to design a proper position controller. This position controller is modified for non-backdrivable and backdrivable cases. For the non-backdrivable case, a pure position controller and an impedance controller are implemented and tested. For the backdrivable case, a constrained motion algorithm is implemented and tested.

The test results show that a proper controller should be chosen by considering the application and the system type in terms of backdrivability. In NeuRoboScope case, the pure position controller can be used due to the high reduction ratio of the gears used in the actuation system (1:905). However, external torque limit has to be considered.

For the human nasal cavity, these torque limits are identified in Chapter 4. Therefore, the external torque has to be measured in order to activate the brakes to constrain the extensive application of forces to the soft tissue. This controller allows the control of the position without being affected by the external torques due to the interaction with the soft tissue. The safety of the procedure can be achieved by activating the brakes when the torque reaches the limit.

If the application requires to control the dynamics between the robot and the soft tissue, impedance control can be applied. By defining different impedance terms, the desired impedance can be realized. By using the environment model, proper impedance terms can be selected in terms of oscillation and external torque limits. Using different environment models may add more poles and zeros to the system's transfer function. In order to simplify the calculations, only the elastic model is considered for the tissue and specimen model. This controller also requires a torque sensor, however by controlling the dynamics of the interaction, torque limit validation can be avoided without activating the brakes.

For the backdrivable systems, the pure position controller cannot be implemented due to the increased effects of the external torque. Therefore, constrained motion control can be implemented in order to eliminate the effect of external torque. This can be realized in two ways. Firstly, the external torque can be measured and added to the control output as a disturbance. This first method calls for a precise and noise-free torque measurement. The second way of the eliminating effects of external torque is adding the measured external torque to the position data by multiplying with a transfer function. By defining this transfer function as the reciprocal of the position controller, the external torque can be eliminated which is a special case of an impedance controller. This controller also requires torque measurements. However, measurements noise can be compensated by modifying the transfer function.

CHAPTER 6

CONCLUSIONS

In the scope of the thesis, compliant control of the NeuRoboScope project's endoscope holder robot is studied to be employed in a robotic endoscopic pituitary gland surgery. Controlling the interaction of the robot is investigated in two separate parts. First, the interaction between the robot and surgeon is considered by designing an admittance controller. The contribution of this part of the study to the literature is that the effects of the admittance terms are presented quantitatively.

In the second part, the interaction between the robot and a patient is considered. One of the important contribution of this part to the literature is identifying the viscoelastic model of the human cadaver nasal concha. In addition to that, force and torque values applied to the soft tissue during the surgery are obtained for this specific surgical procedure. Making use of these outcomes, several compliant controllers are implemented and tested for the defined control scenario. Results show that it is possible to regulate the robot-soft tissue interaction for safety purposes while controlling the motion of the endoscope by using an adequate force/torque sensor.

As a future work, compliant control algorithms can be tested by different environmental models for a multi DoF system by considering the different robot kinematics. In addition to that, the commercial F/T sensors are not compatible with the surgical case, therefore, it is possible to implement F/T observers to measure the external force and torques or application based specialized sensor can be developed.

REFERENCES

Allaf, M., S. Jackman, P. Schulam, J. Cadeddu, B. Lee, R. Moore, and L. Kavoussi (1998). Laparoscopic visual field. *Surgical Endoscopy 12*(12), 1415–1418.

Anderson, R. J. and M. W. Spong (1988). Hybrid impedance control of robotic manipulators. *IEEE Journal on Robotics and Automation 4*(5), 549–556.

ATI (2018 (accessed November 18, 2018)). *ATI INDUSTRIAL AUTOMATION*. https://www.ati-ia.com/products/ft/sensors.aspx.

Balaniuk, R. and K. Salisbury (2002). Dynamic simulation of deformable objects using the Long Elements Method. In *Proceedings 10th Symposium on Haptic Interfaces for Virtual Environment and Teleoperator Systems*, pp. 58–65.

Basdogan, C., C. H. Ho, and M. A. Srinivasan (2001, September). Virtual environments for medical training: graphical and haptic simulation of laparoscopic common bile duct exploration. *IEEE/ASME Transactions on Mechatronics 6*(3), 269–285.

Bauzano, E., I. Garcia-Morales, P. del Saz-Orozco, J. C. Fraile, and V. F. Munoz (2013, November). A minimally invasive surgery robotic assistant for HALS SILS techniques. *Computer Methods and Programs in Biomedicine 112*(2), 272–283.

Berkelman, P., L. Whitcomb, R. Taylor, and P. Jensen (2003, October). A miniature microsurgical instrument tip force sensor for enhanced force feedback during robot-assisted manipulation. *IEEE Transactions on Robotics and Automation 19*(5), 917–922.

Bicchi, A., G. Canepa, D. De Rossi, P. Iacconi, and E. P. Scillingo (1996). A sensor-based minimally invasive surgery tool for detecting tissutal elastic properties. In *, Proceedings, of IEEE International Conference on Robotics and Automation*, pp. 884–888.

Camarillo, D. B., T. M. Krummel, and J. Salisbury (2004, October). Robotic technology in surgery: Past, present, and future. *The American Journal of Surgery 188*(4), 2–15.

Castaneda, M. A. P. and F. A. Cosio (2003, September). Computer simulation of prostate resection for surgery training. In *Proceedings of the 25th Annual International Conference of the IEEE Engineering in Medicine and Biology Society*, pp. 1152–1155.

Cotin, S., H. Delingette, and N. Ayache (1999, January). Real-time elastic deformations of soft tissues for surgery simulation. *IEEE Transactions on Visualization and Computer Graphics 5*(1), 62–73.

Craiem, D., F. J. Rojo, J. M. Atienza, R. L. Armentano, and G. V. Guinea (2008, September). Fractional-order viscoelasticity applied to describe uniaxial stress re-

laxation of human arteries. *Physics in Medicine and Biology 53*(17), 4543–4554.

Craig, J. J. (1989). *Introduction to Robotics: Mechanics and Control*. Pearson/Prentice Hall, Upper Saddle River, NJ, USA.

Dai, X., B. Zhao, S. Zhao, Y. He, Y. Sun, P. Gao, Y. Hu, and J. Zhang (2016). An endoscope holder with automatic tracking feature for nasal surgery. In *International Conference on Information and Automation*, pp. 1–6.

Dargahi, J., M. Parameswaran, and S. Payandeh (2000, September). A micromachined piezoelectric tactile sensor for an endoscopic grasper-theory, fabrication and experiments. *Journal of Microelectromechanical Systems 9*(3), 329–335.

Dario, P., M. C. Carrozza, M. Marcacci, S. D'Attanasio, B. Magnami, O. Tonet, and G. Megali (2000). A novel mechatronic tool for computer-assisted arthroscopy. *IEEE Transactions on Information Technology in Biomedicine 4*(1), 15–29.

De, S., J. Kim, Y.-J. Lim, and M. A. Srinivasan (2005, June). The point collocation-based method of finite spheres (PCMFS) for real time surgery simulation. *Computers & Structures 83*(17), 1515–1525.

De, S., Y. J. Lim, M. Manivannan, and M. A. Srinivasan (2006, June). Physically Realistic Virtual Surgery Using the Point-Associated Finite Field (PAFF) Approach. *Presence 15*(3), 294–308.

Dede, M. İ. C. (2003). Position/force control of robot manipulators. M.Sc. thesis, METU.

Delingette, H. (1998). Toward realistic soft-tissue modeling in medical simulation. *Proceedings of the IEEE 86*(3), 512–523.

Ebrahimi, A., S. Sadeghnejad, G. Vossoughi, H. Moradi, and F. Farahmand (2016). Nonlinear adaptive impedance control of virtual tool-tissue interaction for use in endoscopic sinus surgery simulation system. In *International Conference on Robotics and Mechatronics*, pp. 66–71.

Ferraguti, F., N. Preda, A. Manurung, M. Bonfe, O. Lambercy, R. Gassert, R. Muradore, P. Fiorini, and C. Secchi (2015, October). An Energy Tank-Based Interactive Control Architecture for Autonomous and Teleoperated Robotic Surgery. *IEEE Transactions on Robotics 31*(5), 1073–1088.

Ferraguti, F., C. Secchi, and C. Fantuzzi (2013). A tank-based approach to impedance control with variable stiffness. In *Robotics and Automation (ICRA), 2013 IEEE International Conference on*, pp. 4948–4953.

Fodor, G. and T. Gabor (1999). Hybrid position and force control algorithm expansion of a robot control system. *Periodica Polytechnica Electrical Engineering 43*(4), 251–261.

From, P. a. J., J. H. Cho, A. Robertsson, T. Nakano, M. Ghazaei, and R. Johansson (2014). Hybrid stiff/compliant workspace control for robotized minimally invasive surgery. In *International Conference on Biomedical Robotics and Biomechatronics*, pp. 345–351.

Fuchs, K. H. (2002, February). Minimally invasive surgery. *Endoscopy 34*(2), 154–159.

Fung, Y. C. (2013, March). *Biomechanics: Mechanical Properties of Living Tissues*. Springer Science & Business Media.

Gallagher, A. G., N. McClure, J. McGuigan, K. Ritchie, and N. P. Sheehy (1998, September). An ergonomic analysis of the fulcrum effect in the acquisition of endoscopic skills. *Endoscopy 30*(7), 617–620.

Gladilin, E., S. Zachow, P. Deuflhard, and H. C. Hege (2001). A biomechanical model for soft tissue simulation in craniofacial surgery. In *Proceedings of International Workshop on Medical Imaging and Augmented Reality*, pp. 137–141.

Gray, B. L. and R. S. Fearing (1996). A surface micromachined microtactile sensor array. In *Robotics and Automation, 1996. Proceedings., 1996 IEEE International Conference on*, Volume 1, pp. 1–6.

Hagn, U., M. Nickl, S. Jörg, G. Passig, T. Bahls, A. Nothhelfer, F. Hacker, L. Le-Tien, A. Albu-Schäffer, R. Konietschke, et al. (2008). The dlr miro: a versatile lightweight robot for surgical applications. *Industrial Robot: An International Journal 35*(4), 324–336.

Hirose, S. and K. Yoneda (1990, May). Development of optical six-axial force sensor and its signal calibration considering nonlinear interference. In *Proceedings IEEE International Conference on Robotics and Automation*, pp. 46–53 vol.1.

Hogan, N. (1985, March). Impedance Control: An Approach to Manipulation: Part I—Theory. *Journal of Dynamic Systems, Measurement, and Control 107*(1), 1–7.

Howe, R. D., W. J. Peine, D. A. Kantarinis, and J. S. Son (1995, May). Remote palpation technology. *IEEE Engineering in Medicine and Biology Magazine 14*(3), 318–323.

Hunt, K. and F. Crossley (1975). Coefficient of restitution interpreted as damping in vibroimpact. *Journal of applied mechanics 42*(2), 440–445.

I. Baumann, P.K. Plinkert, W. K. G. B. (2001, January). Vibrotactile characteristics of different tissues in endoscopic otolaryngologic surgery - in vivo and ex vivo measurements. *Minimally Invasive Therapy & Allied Technologies 10*(6), 323–327.

IntuitiveSurgical (2000 (accessed April 16, 2018)). *da Vinci Surgical System*. https://www.intuitivesurgical.com/products/.

Işıtman, O., O. Ayit, and M. İ. C. Dede (2017). The effects of admittance term on backdrivability. In *International Workshop on Computational Kinematics*, pp. 181–190.

Işıtman, O., O. Ayit, and M. İ. C. Dede (2018). Viscoelastic modeling of human nasal tissues with a mobile measurement device. In *International Workshop on Medical and Service Robots*, pp. 102–110.

Katsura, S., Y. Matsumoto, and K. Ohnishi (2007, February). Modeling of Force Sensing and Validation of Disturbance Observer for Force Control. *IEEE Transactions on Industrial Electronics 54*(1), 530–538.

Keeve, E., S. Girod, and B. Girod (1996). Craniofacial surgery simulation. In *Visualization in Biomedical Computing*, Lecture Notes in Computer Science, pp. 541–546. Springer, Berlin, Heidelberg.

Kerdok, A. E., S. M. Cotin, M. P. Ottensmeyer, A. M. Galea, R. D. Howe, and S. L. Dawson (2003, September). Truth cube: establishing physical standards for soft tissue simulation. *Medical Image Analysis 7*(3), 283–291.

Khan, S. G., G. Herrmann, M. Al Grafi, T. Pipe, and C. Melhuish (2014, September). Compliance Control and Human–Robot Interaction: Part 1 — Survey. *International Journal of Humanoid Robotics 11*(03), 128–155.

Kim, V. B., W. H. H. I. Chapman, R. J. Albrecht, B. M. Bailey, J. A. Young, L. W. Nifong, and W. R. J. Chitwood (2002, February). Early Experience with Telemanipulative Robot-Assisted Laparoscopic Cholecystectomy Using da Vinci. *Surgical Laparoscopy Endoscopy & Percutaneous Techniques 12*(1), 33–40.

Kim, W. Y., S. Y. Ko, J.-O. Park, and S. Park (2016, May). 6-DOF force feedback control of robot-assisted bone fracture reduction system using double F/T sensors and adjustable admittances to protect bones against damage. *Mechatronics 35*, 136–147.

Kim, B., J. Park, S. Park, and S. Kang (2010, April). Impedance Learning for Robotic Contact Tasks Using Natural Actor-Critic Algorithm. *IEEE Transactions on Systems, Man, and Cybernetics, Part B (Cybernetics) 40*(2), 433–443.

Kühnapfel, U., H. K. Cakmak, and H. Maaß (2000). Endoscopic surgery training using virtual reality and deformable tissue simulation. *Computers & Graphics 24*(5), 671–682.

Lanfranco, A. R., A. E. Castellanos, J. P. Desai, and W. C. Meyers (2004, January). Robotic Surgery: A Current Perspective. *Annals of Surgery 239*(1), 14–21.

Lewandowski, R. and B. Chorazyczewski (2010, January). Identification of the parameters of the Kelvin–Voigt and the Maxwell fractional models, used to modeling of viscoelastic dampers. *Computers & Structures 88*(1), 1–17.

Mahvash, M. and P. E. Dupont (2011, April). Stiffness Control of Surgical Continuum

Manipulators. *IEEE Transactions on Robotics 27*(2), 334–345.

Maxon (2018 (accessed March 8, 2018)). *Maxon Motor AG*. Available at: https://www.maxonmotor.com/maxon/view/catalog/.

Meral, F. C., T. J. Royston, and R. Magin (2010, April). Fractional calculus in viscoelasticity: An experimental study. *Communications in Nonlinear Science and Numerical Simulation 15*(4), 939–945.

Misra, S., K. T. Ramesh, and A. M. Okamura (2008). Modeling of tool-tissue interactions for computer-based surgical simulation: A literature review. *Presence: Teleoperators and Virtual Environments 17*(5), 463–491.

Moreira, P., N. Zemiti, C. Liu, and P. Poignet (2014). Viscoelastic model based force control for soft tissue interaction and its application in physiological motion compensation. *Computer Methods and Programs in Biomedicine 116*(2), 52–67.

Nisky, I., F. Huang, A. Milstein, C. M. Pugh, F. A. Mussa-ivaldi, and A. Karniel (2012). Perception of Stiffness in Laparoscopy–the Fulcrum Effect. *Studies in Health Technology and Informatics 173*, 313–319.

Omata, S., Y. Murayama, and C. E. Constantinou (2004, May). Real time robotic tactile sensor system for the determination of the physical properties of biomaterials. *Sensors and Actuators A: Physical 112*(2-3), 278–285.

Osa, T., S. Uchida, N. Sugita, and M. Mitsuishi (2014). Hybrid control of master-slave velocity control and admittance control for safe remote surgery. In *International Conference on Intelligent Robots and Systems*, pp. 1328–1334.

Ott, C., R. Mukherjee, and Y. Nakamura (2010). Unified impedance and admittance control. In *International Conference on Robotics and Automation*, pp. 554–561.

Pappalardo, A., A. Albakri, C. Liu, L. Bascetta, E. De Momi, and P. Poignet (2016). Hunt–crossley model based force control for minimally invasive robotic surgery. *Biomedical Signal Processing and Control 29*, 31–43.

Payne, C. J. and G.-Z. Yang (2014, August). Hand Held Medical Robots. *Annals of Biomedical Engineering 42*(8), 1594–1605.

Peirs, J., J. Clijnen, D. Reynaerts, H. V. Brussel, P. Herijgers, B. Corteville, and S. Boone (2004, September). A micro optical force sensor for force feedback during minimally invasive robotic surgery. *Sensors and Actuators A: Physical 115*(2-3), 447–455.

Petter, E., M. Biehl, and J. U. Meyer (1996, October). Vibrotactile palpation instrument for use in minimal invasive surgery. In *Proceedings of 18th Annual International Conference of the IEEE Engineering in Medicine and Biology Society*, pp. 179–180.

PNI (2018 (accessed February 21, 2018)). *Pacific Neuroscience Institute*. https://www.pacificneuroscienceinstitute.org/blog/pituitary-disorders/acromegaly-101/.

Prasad, S. K., M. Kitagawa, G. S. Fischer, J. Zand, M. A. Talamini, R. H. Taylor, and A. M. Okamura (2003). A modular 2-DOF force-sensing instrument for laparoscopic surgery. In *International Conference on Medical Image Computing and Computer-Assisted Intervention*, pp. 279–286.

Puangmali, P., K. Althoefer, L. D. Seneviratne, D. Murphy, and P. Dasgupta (2008, April). State-of-the-Art in Force and Tactile Sensing for Minimally Invasive Surgery. *IEEE Sensors Journal 8*(4), 371–381.

Raibert, M. H. and J. J. Craig (1981). Hybrid position/force control of manipulators. *Journal of Dynamic Systems, Measurement, and Control 103*(2), 126–133.

Richards, C., J. Rosen, B. Hannaford, M. MacFarlane, and M. Sinanan (1999). Surgeon-tool force/torque signatures - evaluation of surgical skills in minimally invasive surgery. *The Conference of Physical & Informational Technologies: Options for a New Era in Healthcare*, 791–798.

Roy, J. and L. L. Whitcomb (2002). Adaptive force control of position/velocity controlled robots: theory and experiment. *IEEE Transactions on Robotics and Automation 18*(2), 121–137.

Slotine, J.-J. E. and Weiping (1991). *Applied Nonlinear Control*, Volume 199 of *1*. Prentice Hall Englewood Cliffs, NJ, USA.

Stoianovici, D. (2000, September). Robotic surgery. *World Journal of Urology 18*(4), 289–295.

Sundaraj, K., C. Mendoza, and C. Laugier (2002, December). A fast method to simulate virtual deformable objects with force feedback. In *7th International Conference on Control, Automation, Robotics and Vision*, pp. 413–418.

Tadano, K. and K. Kawashima (2006). Development of 4-DOFs forceps with force sensing using pneumatic servo system. In *Proceedings of IEEE International Conference on Robotics and Automation*, pp. 2250–2255.

Tavakoli, M. (2008). *Haptics for teleoperated surgical robotic systems*. World Scientific, Hackensack, NJ, USA.

Taylor, R., P. Jensen, L. Whitcomb, A. Barnes, R. Kumar, D. Stoianovici, P. Gupta, Z. Wang, E. Dejuan, and L. Kavoussi (1999). A steady-hand robotic system for microsurgical augmentation. *The International Journal of Robotics Research 18*(12), 1201–1210.

Taylor, R. and D. Stoianovici (2003, October). Medical robotics in computer-integrated surgery. *IEEE Transactions on Robotics and Automation 19*(5), 765–781.

Tholey, G., A. Pillarisetti, W. Green, and J. P. Desai (2004). Design, Development, and Testing of an Automated Laparoscopic Grasper with 3-D Force Measurement Capability. In *Medical Simulation*, Lecture Notes in Computer Science, pp. 38–48. Springer, Berlin, Heidelberg, Germany.

Volpe, R. and P. Khosla (1993). The equivalence of second order impedance control and proportional gain explicit force control: Theory and experiments. In *Experimental Robotics II*, Lecture Notes in Control and Information Sciences, pp. 1–24. Springer, Berlin, Heidelberg, Germany.

Wang, W., R. N. K. Loh, and E. Y. Gu (1998, February). Passive compliance versus active compliance in robot-based automated assembly systems. *Industrial Robot: An International Journal 25*(1), 48–57.

Watanabe, T., T. Iwai, Y. Fujihira, L. Wakako, H. Kagawa, and T. Yoneyama (2014, March). Force Sensor Attachable to Thin Fiberscopes/Endoscopes Utilizing High Elasticity Fabric. *Sensors 14*(3), 5207–5220.

Whitney, D. (1985, March). Historical perspective and state of the art in robot force control. In *Proceedings of IEEE International Conference on Robotics and Automation*, Volume 2, pp. 262–268.

Yip, M. C., S. G. Yuen, and R. D. Howe (2010, May). A Robust Uniaxial Force Sensor for Minimally Invasive Surgery. *IEEE Transactions on Biomedical Engineering 57*(5), 1008–1011.

Yuen, S. G., D. T. Kettler, P. M. Novotny, R. D. Plowes, and R. D. Howe (2009, October). Robotic Motion Compensation for Beating Heart Intracardiac Surgery. *The International Journal of Robotics Research 28*(10), 1355–1372.

Yuen, S. G., D. P. Perrin, N. V. Vasilyev, J. Pedro, and R. D. Howe (2010). Force tracking with feed-forward motion estimation for beating heart surgery. *IEEE Transactions on Robotics 26*(5), 888–896.

Zeng, G. and A. Hemami (1997). An overview of robot force control. *Robotica 15*(05), 473–482.